FOSSIL ENERGY

DOE/BC/15201-1
(OSTI ID: 782900)

FLUID-ROCK CHARACTERIZATION AND INTERACTIONS IN NMR WELL LOGGING

Annual Report
August 1, 1999-July 31, 2000

By:
George J. Hirasaki
Kishore K. Mohanty

Date Published: July 2001

Work Performed Under Contract No. DE-AC26-99BC15201

Rice University
Houston, Texas

National Energy Technology Laboratory
National Petroleum Technology Office
U.S. DEPARTMENT OF ENERGY
Tulsa, Oklahoma

DOE/BC/15201-1
Distribution Category UC-122

Fluid-Rock Characterization and Interactions in NMR Well Logging

By
George J. Hirasaki
Kishore K. Mohanty

July 2001

Work Performed Under Contract DE-AC26-99BC15201

Prepared for
U.S. Department of Energy
Assistant Secretary for Fossil Energy

Ginny Weyland, Project Manager
National Petroleum Technology Office
P.O. Box 3628
Tulsa, OK 74101

Prepared by
Rice University
6100 Main Street
Houston, TX 77005-1892

Subcontractor
University of Houston
4800 Calhoun Road
Houston, TX 77204-4792

TABLE OF CONTENTS

Relaxation and Self-Diffusion Measurements of Pure Ethane at Ambient and Elevated Temperature

NMR Analysis of Crude Oil and Pure Hydrocarbons

Interpretation of Wettability in Sandstones With NMR Analysis

Internal Field Gradients in Porous Media

Task 3.0 Pore Morphology/Rock Characterization

Stochastic Reconstruction of 3D Porous Media by Simulated Annealing Method

NMR Response Simulation Technique

ABSTRACT

Objective: To characterize the fluid properties and fluid-rock interactions that are needed for formation evaluation by NMR well logging.

This is the first annual progress report submitted to the DOE. It reports on the work completed during the reporting period even if it may have started before this period.

This project is a partnership between Professor George J. Hirasaki at Rice University and Professor Kishore Mohanty at University of Houston. In addition to the DOE, this project is supported by a consortium of oil companies and service companies.

The fluid properties characterization has emphasized the departure of live oils from correlations based on dead oils. Also, asphaltic components can result in a difference between the T_1 and T_2 relaxation time distributions as well as reduce the hydrogen index.

The fluid rock characterizations that are reported here are the effects of wettability and internal magnetic field gradients.

A pore reconstruction method has been developed to recreate three-dimensional porous media from two-dimensional images that reproduce some of their key statistical properties. A Monte Carlo simulation technique has been developed to calculate the magnetization decay in fluid saturated porous media given their pore structure.

INTRODUCTION

Objective: To characterize the fluid properties and fluid-rock interactions that are needed for formation evaluation by NMR well logging.

NMR well logging is finding wide use in formation evaluation. The formation parameters commonly estimated are porosity, permeability, and capillary bound water. Special cases include estimation of oil viscosity, residual oil saturation, location of oil/water contact, and interpretation on whether the hydrocarbon is oil or gas. In most cases, it is adequate to determine if the formation is sandstone or carbonate and then use default parameters and interpretation methods. However, it is important to recognize the exceptional cases and have parameters and interpretation methods for these cases.

Default rock and fluid properties are very useful in the interpretation of NMR logs because the exact lithology and fluid composition of the logged interval may not be known. In most cases it is necessary to only know if the formation is sandstone or carbonate. For example, a water-wet sandstone formation with insignificant internal gradient effects, having microporosity that is diffusionally isolated from the macropores and containing a hydrocarbon with a unit hydrogen index and long bulk relaxation time can use a 33 ms T_2 cutoff to estimate the volume of capillary-bound water, mobile fluids, total porosity, and permeability (Kenyon, 1997; Kleinberg and Vinegar, 1996; Straley, et al., 1997). However, there are limits to the validity of the default properties and core analysis or fluid analysis will be needed in these cases to refine the correlations.

Some exceptions we propose to address are as follows: (1) departure of the relaxation time – viscosity correlation for methane-containing live oil from existing correlations based on stock tank oils and viscosity standards, (2) departure of the live oil hydrogen index from unity or the correlations based on alkanes or on API gravity, (3) crude oils that have bulk fluid relaxation time distributions that overlap with that for the capillary bound water, (4) wettability alterations that result in oil relaxation time distributions that overlap with that for the capillary bound water, (5) wettability alteration with crude oils and oil based drilling fluids that alter value of the capillary bound water from that of water-wet conditions, (6) diffusion effects resulting from internal gradients which cause an echo spacing dependent shortening of the relaxation time distribution for both brine and hydrocarbons, (7) diffusional coupling between the brine in the micropores and the brine in the macropores, and (8) estimation of permeability of vuggy carbonates.

EXECUTIVE SUMMARY

The work is divided into; Task 1.0 Fluid Properties, Task 2.0 Fluid-Rock Interactions, Task 3.0 Pore Morphology/Rock Characterization.

The main emphasis of fluid properties was the characterization of live oils. The relaxation time versus oil viscosity correlations in the literature are based on dead oils. Live oils are expected to differ from dead oils because methane relaxes with the spin-rotation mechanism while higher molecular weight hydrocarbons relax by the dipole-dipole mechanism. These two mechanisms have the opposite dependence of viscosity. Relaxation time and self-diffusion measurements were made on binary mixtures of methane with hexane, decane, and hexadecane. The measurements showed that the relaxation time deviated from the correlation based on dead oils as the methane content increased. A correlation was developed to describe the deviation of the live oil relaxation time from that of the dead oil as a function of the gas/oil ratio. This correlation is valid for all three oils with the methane content increasing to that of the vapor phase. Measurements are being made with ethane to determine which hydrocarbon gas components must be correlated by the spin-rotation mechanism.

Asphaltic oil may be problematic because of the broad relaxation time distribution and possibly reduced hydrogen index. A database has been accumulated for a set of crude oils and pure hydrocarbons. A difference between T_1 and T_2 relaxation time that correlates with the asphaltene content was found. Also, the hydrogen index can be significantly less than 1.0.

The usual assumption for interpreting NMR well logs is that the formation is water-wet such that the brine relaxes by surface relaxation and the hydrocarbon relaxes as bulk fluid. This assumption may not be valid if the formation is mixed-wet. The NMR relaxation time was measured for three different sandstones with a refined oil and with a crude oil that is known to alter wettability. Bentheim and Berea were water-wet with refined oil, but became mixed-wet with crude oil after aging. Due to the chlorite lining of North Burbank, it was mixed-wet even with refined oil. Wettability alteration does not always result in lengthening of the water relaxation time. However, in every case of wettability alteration, a shortening of the relaxation time of the residual oil was observed.

Fluid typing with diffusion measurements in NMR well logging is usually interpreted assuming that the magnetic field gradient is that applied by the tool design. However, formations that contain paramagnetic minerals can have induced or internal gradients that are larger than that imposed by the tool design. Analytical solutions have been developed for arrays of cylinders and spheres and for pores lined with chlorite clay flakes. These models will subsequently be used to interpret NMR measurements where internal gradients are significant.

A pore reconstruction method has been developed to recreate three-dimensional porous media from two-dimensional images that reproduce some of their key statistical properties. A Monte Carlo simulation technique has been developed to calculate the magnetization decay in fluid saturated porous media given their pore structure. This technique has been validated against analytical solutions for simply-shaped pores.

Task 1.0 Fluid Properties: The fluid properties to be studied are subdivided into; Sub-Task 1.1 Hydrogen Index; Sub-Task 1.2 Relaxation Time of Live Oils; Sub-Task 1.3 Diffusivity of Methane-Hydrocarbon Mixtures; and Sub-task 1.4 Relaxation Time Distribution of Asphaltic Oils.

Sub-Task 1.1 Hydrogen Index: An approach has been developed to calculate the hydrogen index (HI) of live oils by expressing the HI as a function of density and hydrogen/carbon ratio H/C. The H/C can be determined from the HI and density of the stock tank oil, composition of the gas, and the formation volume factor and solution gas/oil ratio. The greatest deviation from the default HI value of 1.0 was found for a 35° API oil with a solution GOR of 1720 scf/STB. While the STO had a HI of 0.98, the live oil at the bubble point had a calculated HI of 0.76. These results are documented in "Some Exceptions to Default NMR Rock and Fluid Properties" SPWLA Annual Meeting, Keystone, CO, May 25-28, 1998.

Sub-Task 1.2 Relaxation Time of Live Oils: and
Sub-Task 1.3 Diffusivity of Methane-Hydrocarbon Mixtures:.

Correlation of NMR Relaxation Time with Viscosity/Temperature, Diffusion Coefficient and Gas/Oil Ratio of Methane-Hydrocarbon Mixtures

Sho-Wei Lo

INTRODUCTION

Viscosity, diffusivity and gas/oil ratio are important transport properties in the characterization of reservoirs by NMR well logging and in prediction of production performance. For the past few years, NMR well logging has been used to estimate the formation properties and hydrocarbon liquid/vapor characterization. Previous work has shown that pure alkanes, alkane mixtures, viscosity standards and stock tank crude oils have NMR relaxation times which vary linearly with viscosity/temperature and diffusivity on a log-log scale. However, pure methane at some temperatures and pressures does not follow the same trend. The linear correlation is not valid for live crude oils that contain significant amount of methane. Therefore, the study of methane-hydrocarbon mixtures is of interest.

SUMMARY

An NMR spectrometer was used to study relationship between NMR relaxation time and temperature, viscosity, diffusivity and gas/oil ratio of methane-hydrocarbon mixtures. NMR relaxation measurements of three mixtures, methane-n-hexane, methane-n-decane and methane-n-hexadecane, were made. The log mean relaxation times were plotted against viscosity/temperature and it was found that unlike stock tank oils, they do not depend linearly on viscosity/temperature on a log-log scale. Each of the mixtures forms a different curve on the plot of relaxation time vs. viscosity/temperature.

Diffusivity measurements were also made for these three mixtures, as well as pure hexane, decane and hexadecane. The log mean diffusion coefficients were calculated. The relationship

between diffusion coefficients and relaxation times were studied, and it was found that diffusion coefficients depend linearly on T_1 for pure hydrocarbons, but the dependence does not hold for methane-hydrocarbon mixtures.

Correlations between transport properties and NMR relaxation times were developed. First, a relaxation time mixing rule was developed by studying the theory of NMR relaxation mechanism. From the mixing rule, it was found that departure of relaxation times of methane-n-alkane mixtures from linear correlation on a log-log scale can be correlated with proton fractions of methane, which can be expressed as gas/oil ratio. Thus, correlation between relaxation time, viscosity/temperature and gas/oil ratio was developed. Correlation between relaxation time, diffusivity and gas/oil ratio was also developed. From these correlations, viscosity and gas/oil ratio can be estimated from NMR relaxation time and diffusion coefficient.

Equipment and Experimental Conditions

A 90 MHz NMR spectrometer with a superconducting magnet was used to make measurements. It is equipped with a high pressure probe and air bath that can take pressure up to 6000 psia and temperature up to 60°C. It also has pulse field gradient capability for diffusivity measurements.

Three mixtures, methane-hexane, methane-decane and methane hexadecane, were measured at elevated pressures and temperatures. The binary mixtures were brought to the desired temperature and pressure. Equilibrium was established by circulating methane through the liquid phase by a magnetic pump. After the mixture reached equilibrium, the liquid or vapor was circulated into the NMR sample probe for measurements. Eqilibrium two-phase, two component mixtures at a specified temperature and pressure have zero degree of freedom. Thus, the phase compositions can be determined from the specific temperature and pressure. The phase composition and viscosity were estimated using experimental data and SUPERTRAPP, the NIST Thermophysical Properties of Hydrocarbon Mixtures Database.

Results

Three mixtures were measured, methane-n-hexane, methane-n-decane and methane-n-hexadecane. For each mixture, both liquid phase and vapor phase were measured. The critical pressure at our temperature range is about 3000 psia for methane-hexane system, therefore the highest pressure for this system measured is about 3000 psia. For methane-decane system, the critical pressure is about 5300 psia, and the highest pressure measured is about 5200 psia. The critical pressure of methane-hexadecane is above our equipment limit, 6000 psia, thus, methane-hexadecane mixtures were measured at up to 6000 psia.

The results of all three mixtures were plotted as T_1 vs. viscosity/ temperature, along with pure alkanes and pure methane, to see the T_1 dependence of viscosity/temperature. Figure 1 is the plot. T_1 of methane-hydrocarbon mixtures do not follow the same correlation as pure alkanes. Methane-hydrocarbon mixtures deviate from the straight line due to the methane relaxation.

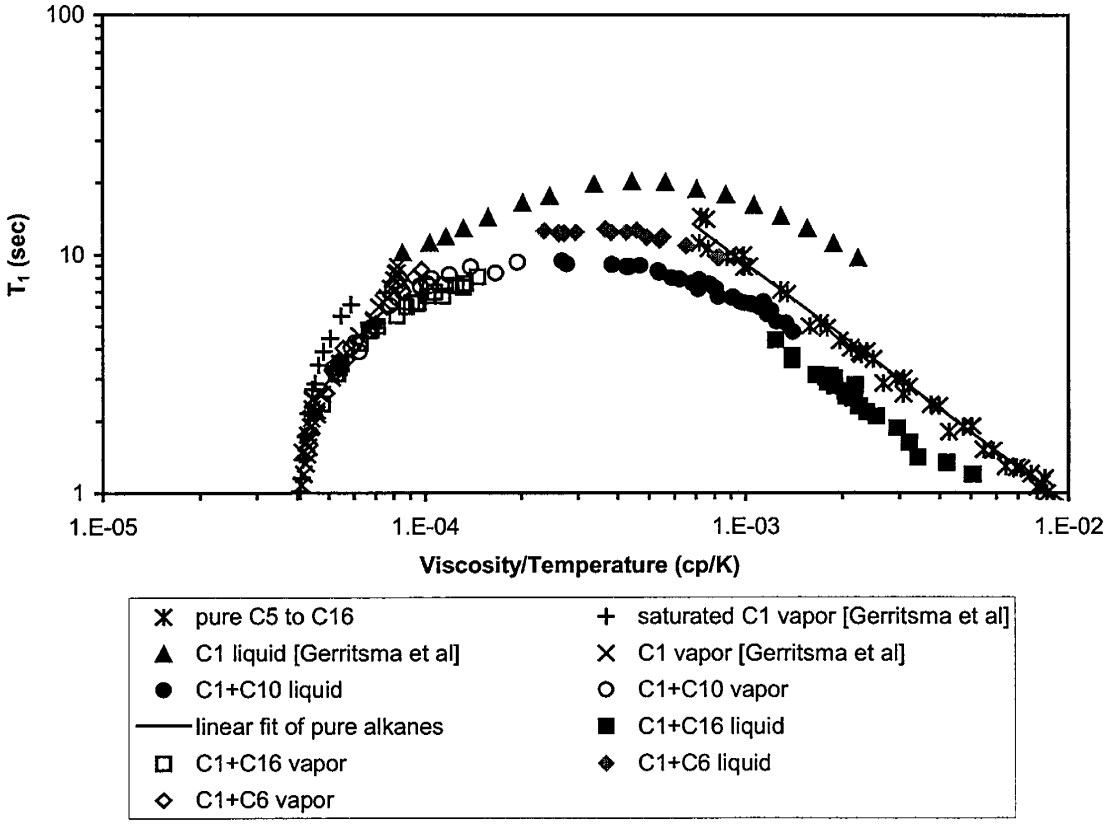

Fig. 1. T_1 dependence of viscosity/temperature

Diffusion coefficients were measured for all three methane-hydrocarbon mixtures. Pure hexane and decane were also measured. Figure 2 is the plot of log mean T_1 against log mean diffusion coefficient of both liquid and vapor phases of the three binary mixtures, along with pure components. The mixtures depart from the straight line of the pure components.

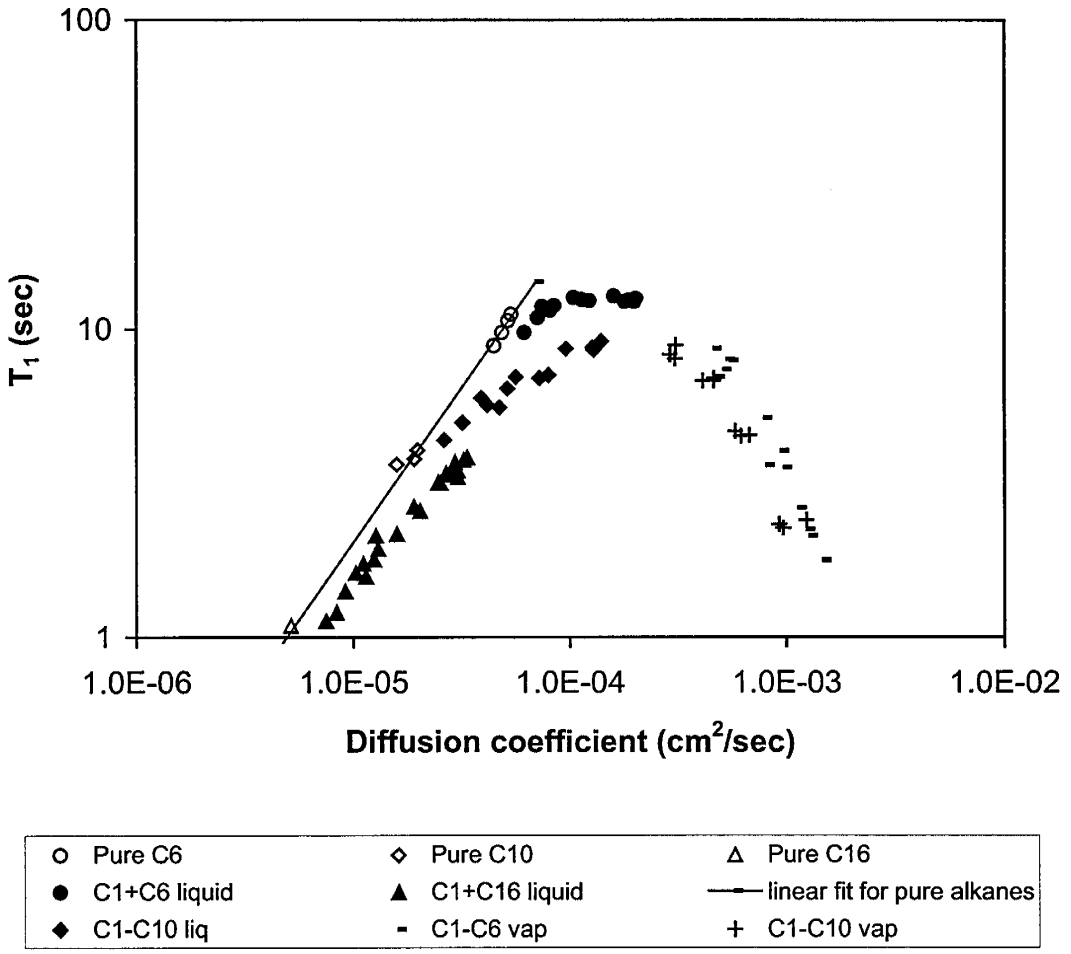

Fig. 2. T_1 dependence on diffusion coefficient: pure alkanes and methane-alkane mixtures

Diffusion coefficient dependence of viscosity/temperature was plotted and observed. Diffusion coefficients have the same linear relationship with viscosity/temperature for all of the mixtures and pure alkanes. Diffusion coefficients are proportional to T/η, $D = 5.05\times10^{-8}\ T/\eta$, where the diffusion coefficient, D, is expresses in cm^2/sec, viscosity, η, is expressed in cp and T is absolute temperature in degree K.

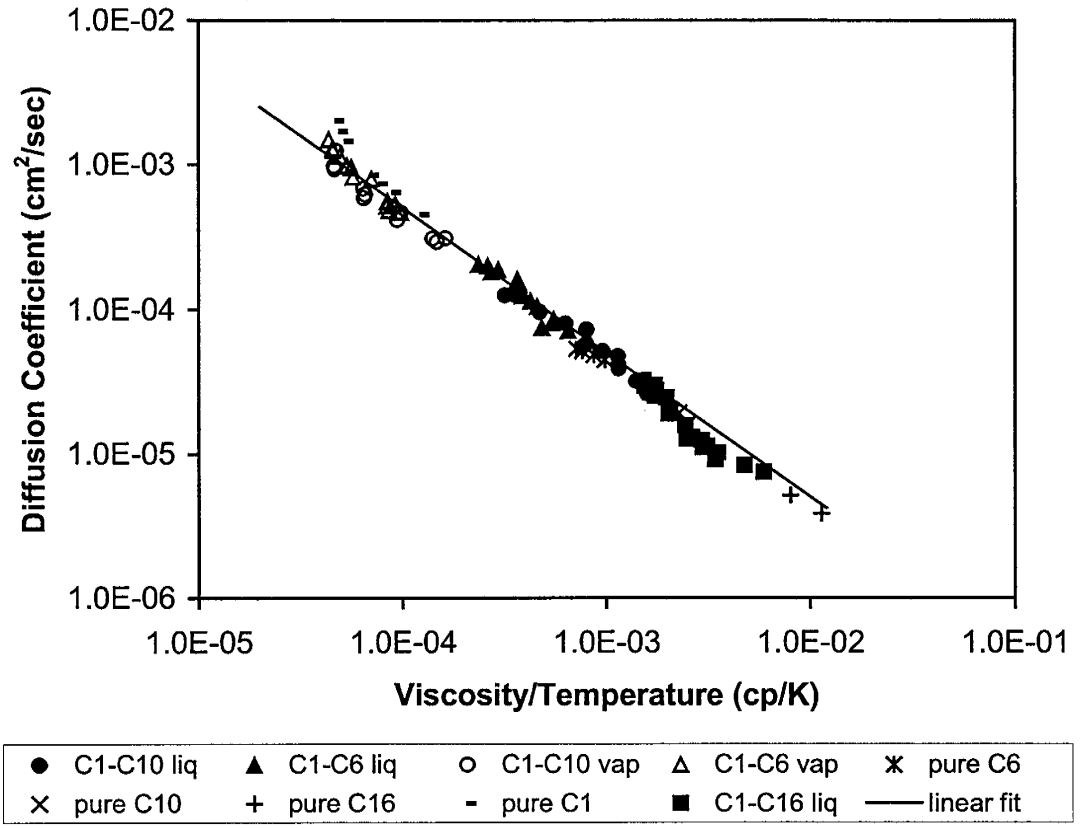

Fig. 3. Diffusivity dependence on η/T for pure alkanes and methane-alkane mixtures

Correlations of Relaxation Time with Transport Properties

As a first step of development of correlations between T_1 and transport properties of fluids, a mixing rule of T_1 is developed. For each methane-alkane mixture, there are two contributions to T_1, one from protons of methane and the other from protons of higher alkane. The log mean T_1 can be described as

$$Log_{10}(T_{1,\log mean}) = H(C1)Log_{10}(T_{1,C1}) + H(A)Log_{10}(T_{1,A}) \qquad (1)$$

where H(C1) is the proton fraction of methane, and H(A) is the proton fraction of the higher alkane; $T_{1,C1}$ and $T_{1,A}$ are the relaxation times of methane and the higher alkane. Some earlier works show

that the dominant relaxation mechanism for pure n-alkanes is an intramolecular interaction,(Zega, 1987) and the dominant relaxation mechanisms for liquid methane are intermolecular and spin rotation interactions (Oosting and Trappeniers, 1971). Thus, we made the assumptions that protons of higher alkanes relax by intramolecular dipole-dipole interaction, and protons of methane relax by spin rotation interaction and intermolecular dipole-dipole interaction.

For intramolecular dipole-dipole interactions, (McConnell, 1987)

$$T_1 = T_2 = \frac{3r^6 D_R}{\gamma^4 \hbar^2 I(I+1)} \tag{2}$$

where

γ = gyromagnetic ratio

$\hbar$ = Plank's constant/2π

r = distance between two protons in the same molecule

D_R = rotational diffusion coefficient

From equation 2, we can conclude that

$$T_2 = T_1 \propto D_R \tag{3}$$

For a spherical molecule with radius a, (McConnell, 1987)

$$D_R = \frac{kT}{8\pi a^3 \eta} \tag{4}$$

Thus,

$$T_2 = T_1 \propto D_R \propto \frac{T}{a^3 \eta} \tag{5}$$

For a mixture with components A and B,

$$T_{1_A} \propto \frac{T}{a_A^3 \eta} \tag{6}$$

$$T_{1_B} \propto \frac{T}{a_B^3 \eta} \tag{7}$$

$$T_{1_m} \propto \frac{T}{a_m^3 \eta} \tag{8}$$

where

T_{1m} = log mean T_1

a_m = log mean radius.

Thus,

$$\frac{T_{1_A}}{T_{1_m}} = \frac{a_m^3}{a_A^3} \tag{9}$$

the log mean radius can be calculated,

$$a_m^3 = e^{\left[H_A \log\left(a_A^3\right) + H_B \log\left(a_B^3\right)\right]} \tag{10}$$

$$a_m = a_A^{H_A} a_B^{H_B} \tag{11}$$

For methane-hydrocarbon mixtures, the relaxation time of the higher hydrocarbon is

$$T_{1,dd} = T_{1_m} \frac{a_m^3}{a_{Cn}^3} \tag{12}$$

T_{1m} can be obtained from the linear fit for pure alkanes from the viscosity/temperature of the mixture. The diameters of the molecules used are the Lennard-Jones diameters estimated from viscosity data. Lennard-Jones diameters are available for normal alkanes from methane to octane (Rowley, 1994).

Methane in the mixtures is assumed to relax by both spin rotation interaction and intermolecular dipole-dipole interaction. The spin rotation relaxation rate is estimated by fitting dilute methane gas data. Dilute pure methane gas relaxes by spin-rotation interaction(Oosting and Trappeniers, 1971). It was discovered that pure methane relaxation times can be correlated with density and temperature in the form of (Lalita *et al*, 1974, Jonas, 1994)

$$\frac{T_1}{\rho} = \frac{C_1}{T^{C_2}} \tag{13}$$

where ρ is the density and T is temperature. C_1 and C_2 can be calculated by fitting literature pure methane T_1 data (this work, Gerritsma *et al*, 1971) with the previous equation in log-log scale.

$$\log\frac{T_1}{\rho} = \log C_1 - C_2 \log T \tag{14}$$

C_1 was found to be 1.57×10^5 and C_2 1.50. Therefore, $T_{1,sr}$ of methane of the mixtures is estimated by

$$\frac{T_{1,sr}}{\rho} = \frac{1.57\times10^5}{T^{1.50}} \tag{15}$$

The spin-rotation relaxation time is

$$T_{1,SR} = \frac{1.57\times10^5 \rho}{T^{1.50}} \tag{16}$$

The intermolecular dipole-dipole relaxation rate can be described as

$$T_{1,inter} = \frac{15kT}{32\pi^2 N\gamma^4\hbar^2 I(I+1)\rho_n \eta} \tag{17}$$

It can be calculated that for hydrogen proton,

$$T_{1,inter} = \frac{TM}{450.84N\rho\eta} \tag{18}$$

where ρ is the density in g/cm^3, and M is the molecular weight. In a methane-hydrocarbon mixture, N can be calculated as

$$N = 4x_{C1} + N_{Cn}x_{Cn} \tag{19}$$

where x_{C1} is the mole fraction of methane in the mixture, N_{Cn} is the number of hydrogen atoms in hydrocarbon, and x_{Cn} is the mole fraction of the hydrocarbon. The molecular weight M can be calculated as

$$M = M_{C1}x_{C1} + M_{Cn}x_{Cn} \tag{20}$$

M_{C1} and M_{Cn} are the molecular weight of methane and higher hydrocarbon, respectively.

The overall mixing rule is,

$$T_{1,Cn} = T_{1_m}\frac{a_m^3}{a_{Cn}^3} \tag{21}$$

$$T_{1,C1} = \frac{1}{\frac{1}{T_{1,SR}} + \frac{1}{T_{1,inter}}} \tag{22}$$

where the calculation of $\frac{1}{T_{1,SR}}$ and $\frac{1}{T_{1,inter}}$ are from equations 16 and 17.

Correlations between transport properties and NMR relaxation time were developed. First, the relationship of deviation of relaxation time from the linear dependence for methane-free alkanes and proton fraction of methane was observed. Deviation of relaxation time on a log-log plot is defined as the difference of T_1 and $T_{1,linear}$ for given viscosity/temperature or diffusion coefficient,

$$Deviation = Log_{10}(T_{1,linear}) - Log_{10}(T_1) = Log_{10}\left(\frac{T_{1,linear}}{T_1}\right) \tag{23}$$

From the overall mixing rule, deviation is

$$Deviation = Log_{10}(T_{1,linear}) - Log_{10}(T_1)$$
$$= H_1\left[Log_{10}(T_{1,SR}T_{1,inter}) - Log_{10}(T_{1,SR} + T_{1,inter}) - Log_{10}(T_{1,linear}) - Log_{10}\frac{a_m^3}{a_n^3}\right] + Log_{10}\frac{a_m^3}{a_n^3} \quad (24)$$

Deviation is a function of the proton fraction of methane. Proton fractions of methane and higher hydrocarbons can be expressed as a gas/oil ratio, where the gas/oil ratio is defined as standard cubic meters of solution gas (methane only) per cubic meter of stock tank oil. The standard condition is 60°F and 1 atm.

$$GOR = \frac{\text{cubic meters of methane at standard condition}}{\text{cubic meters of stock tank oil}} = \frac{x_{C1}M_{C1}}{x_{Cn}M_{Cn}} \times \frac{\rho_{Cn,60^\circ F,1atm}}{\rho_{C1,60^\circ F,1atm}} \quad (25)$$

where x_{C1} and x_{Cn} are the mole fraction of methane and n-alkane, M_{C1} and M_{Cn} are the molecular weight of methane and n-alkane, and ρ_{C1} and ρ_{Cn} are the mass density of methane and n-alkane, respectively. There is a one to one correspondence between the GOR and proton ratio, where the proton ratio is

$$\text{Proton Ratio} = \frac{\text{number of protons from methane in the mixture}}{\text{number of protons from n - alkane in the mixture}} = \frac{4x_{C1}}{(2n+2)x_{Cn}} \quad (26)$$

From equations 25 and 26, the conversion between the GOR and proton ratio is

$$GOR = \frac{(2n+2)M_{C1}}{4M_{Cn}} \times \frac{\rho_{Cn,60^\circ F,1atm}}{\rho_{C1,60^\circ F,1atm}} \times (\text{Proton Ratio}) \quad (27)$$

Deviation of mixture T_1 is plotted against gas/oil ratio in Figure 4.

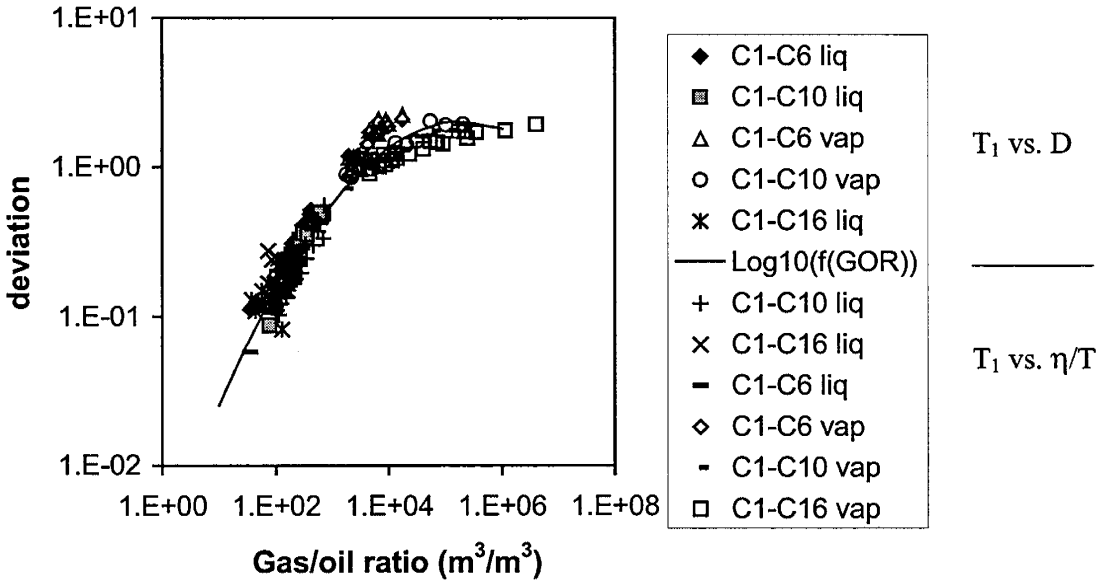

Fig. 4. Log-log plot of deviation vs. gas/oil ratio

Deviation of relaxation time from linear dependence on viscosity/temperature and diffusion coefficient on a log-log plot can be correlated with gas/oil ratio by the function fitting curve, f(GOR). Thus,

$$deviation = Log_{10}(T_{1,linea}) - Log_{10}(T_1) = Log_{10}(f(GOR)) \quad (28)$$

From the fitting curve,

$$Log_{10}(deviation) = -0.127(Log_{10}GOR)^2 + 1.25Log_{10}GOR - 2.80 \quad (29)$$

To test this hypothesis, the methane-hydrocarbon mixtures were mapped onto the linear correlation on log-log plot of T_1 vs. viscosity/temperature by adding the deviation to T_1. Define T_1* as the projection of T_1 onto $T_{1,linear}$ on T_1 vs. viscosity/temperature plot.

$$Log_{10}(T_1^*) = Log_{10}(T_1) + deviation \quad (30)$$

$$Log_{10}(T_1^*) = Log_{10}(T_1) + Log_{10}(f(GOR)) \quad (31)$$

$$T_1^* = T_1 \times f(GOR) \quad (32)$$

T_1* falls near $T_{1,linear}$ (methane-free system) on log-log plot of T_1 vs η/T. Figure 5 is the plot of T_1* vs. η/T. The average difference between T_1* and $T_{1,linear}$ is 16.3%.

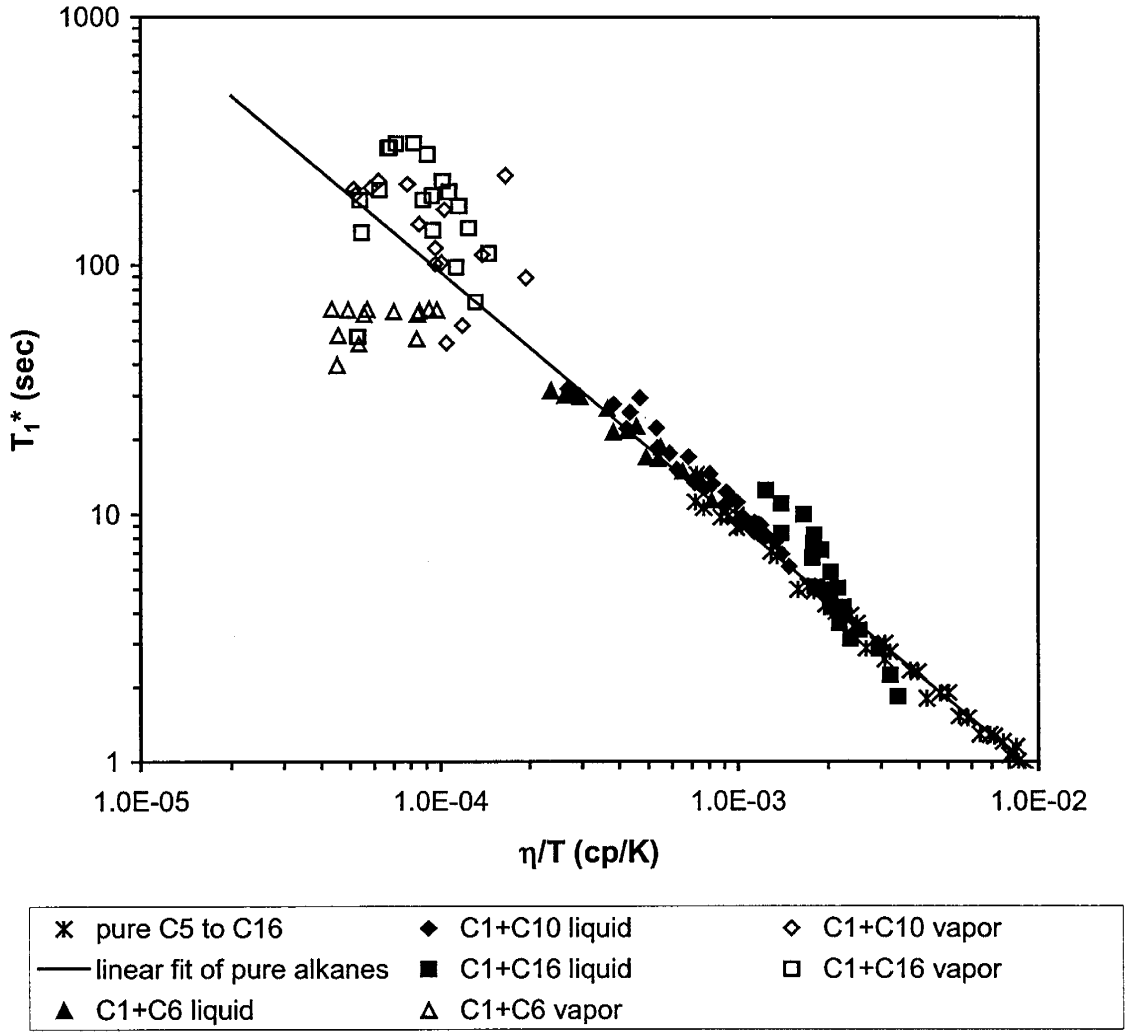

Fig. 5. T_1* dependence on viscosity/temperature

Since T_1 can be expressed as a function of $T_{1,linear}$ and gas/oil ratio, and $T_{1,linear}$ can be expressed as a function of viscosity/temperature, T_1 can be expressed as a function of gas/oil ratio and viscosity/temperature.

$$T_1 = \frac{T_{1,linear}}{f(GOR)} \tag{33}$$

$$T_{1,linear} = 0.009558\frac{T}{\eta} \tag{34}$$

$$T_1 = \frac{0.009558\frac{T}{\eta}}{f(GOR)} = F_1(GOR, \tfrac{\eta}{T}) \tag{35}$$

From this correlation, GOR contour lines can be drawn on the plot of T_1 vs. η/T. The contour lines are parallel to the linear line of zero GOR. Figure 6 is the plot with constant GOR contour lines.

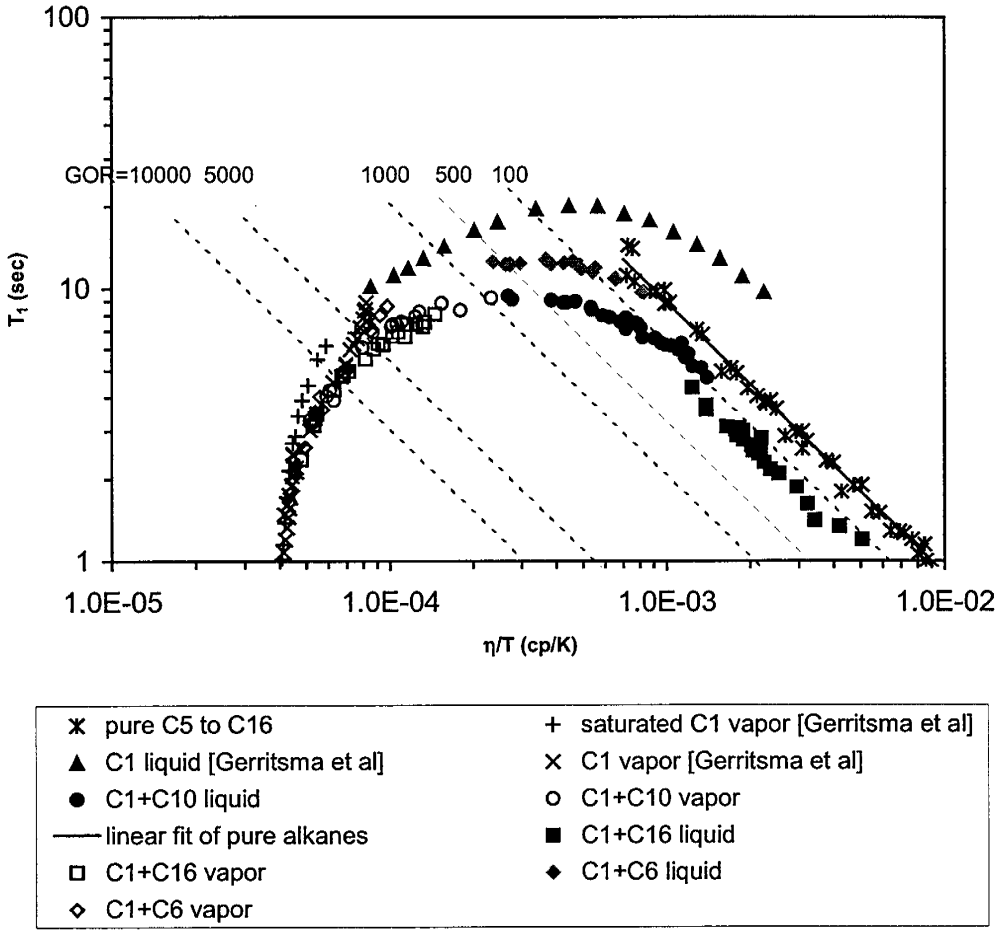

Fig. 6. T_1 vs. η/T with constant GOR contour lines

T_1 dependence on diffusion coefficient can be treated the same way. Define T_1** as a projection of T_1 onto $T_{1,linear}$ on T_1 vs. diffusivity plot.

$$Log_{10}(T_1^{**}) = Log_{10}(T_1) + deviation \tag{36}$$

$$Log_{10}(T_1^{**}) = Log_{10}(T_1) + Log_{10}(f(GOR)) \tag{37}$$

$$T_1^{**} = T_1 \times f(GOR) \tag{38}$$

Figure 7 is the plot of T_1** dependence on diffusion coefficient. The average percent difference between T_1** and $T_{1,linear}$ is 12.0%.

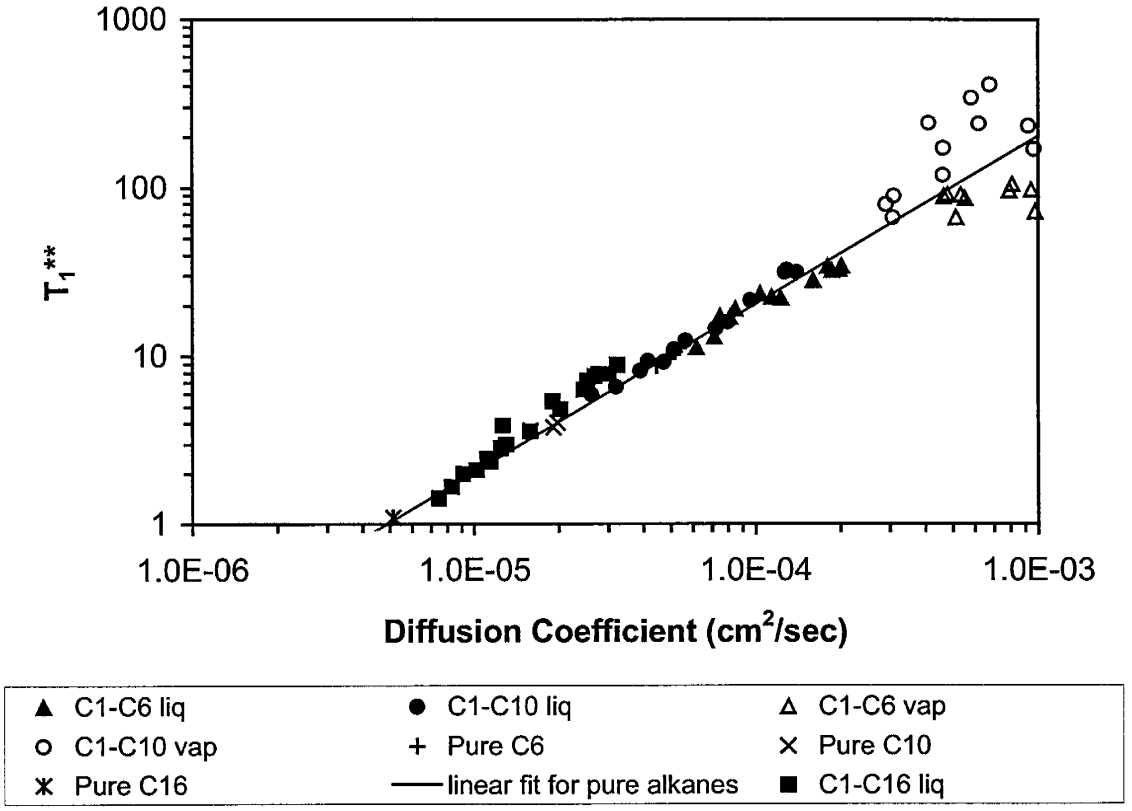

Fig. 7. T_1** vs. diffusion coefficient for pure alkanes and methane-alkane mixtures

T_1 is a function of $T_{1,linear}$ and gas/oil ratio, and $T_{1,linear}$ is a function of diffusion coefficient. Thus, T_1 can be expressed as a function of gas/oil ratio and diffusion coefficient.

$$T_1 = \frac{T_{1,linear}}{f(GOR)} \tag{39}$$

$$T_{1,linear} = 2.04\times10^5 D \tag{40}$$

$$T_1 = \frac{2.04\times10^5 D}{f(GOR)} = F_2(GOR, D) \tag{41}$$

The contour lines of constant GOR can also be plotted on the figure of T_1 vs. D. Figure 8 is the plot of T_1 vs. D with constant GOR contour lines.

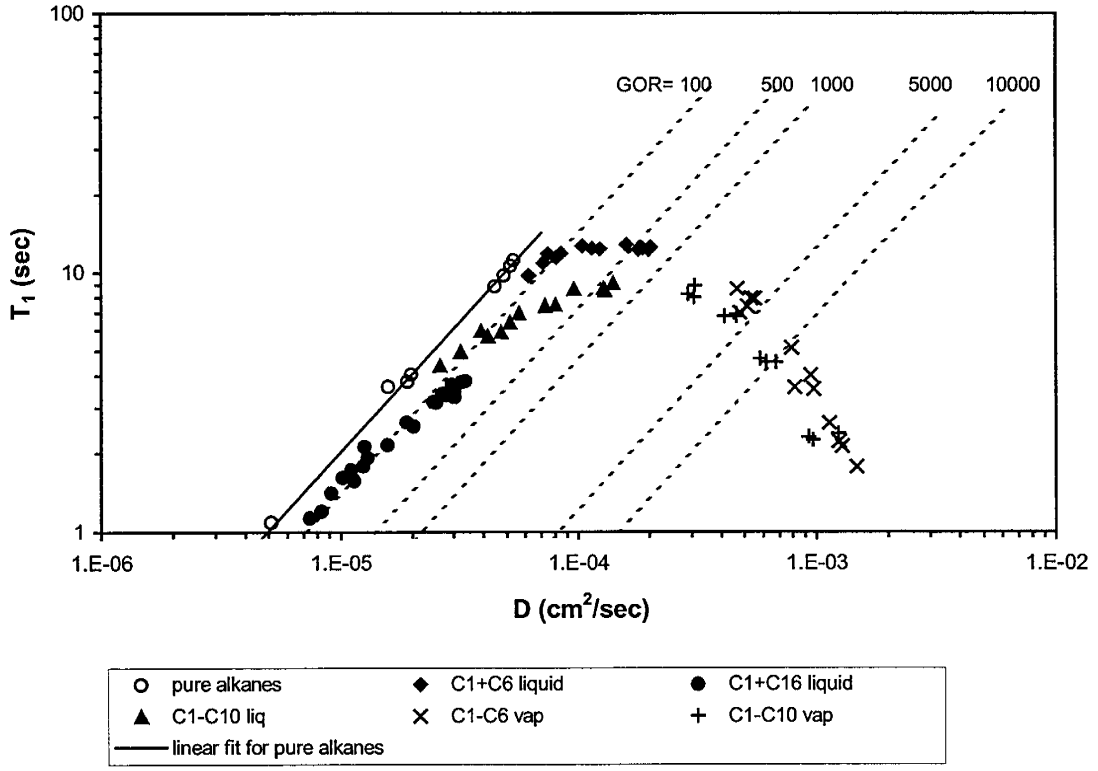

Fig. 8. T_1 vs. D with constant GOR contour lines

From equations 34 and 40, the correlation between diffusion coefficient and viscosity/temperature can be calculated,

$$D = 4.69\times10^{-8}\frac{T}{\eta} \tag{42}$$

The relationship between diffusion coefficient and viscosity/temperature was studied directly in the results section. From the experimental data it was found that

$$D = 5.05\times10^{-8}\frac{T}{\eta} \tag{43}$$

These two methods have about 7% difference.

T_1 vs. D and T_1 vs. T/η can be plotted together with common contour lines of constant GOR. Figure 9 shows the plot.

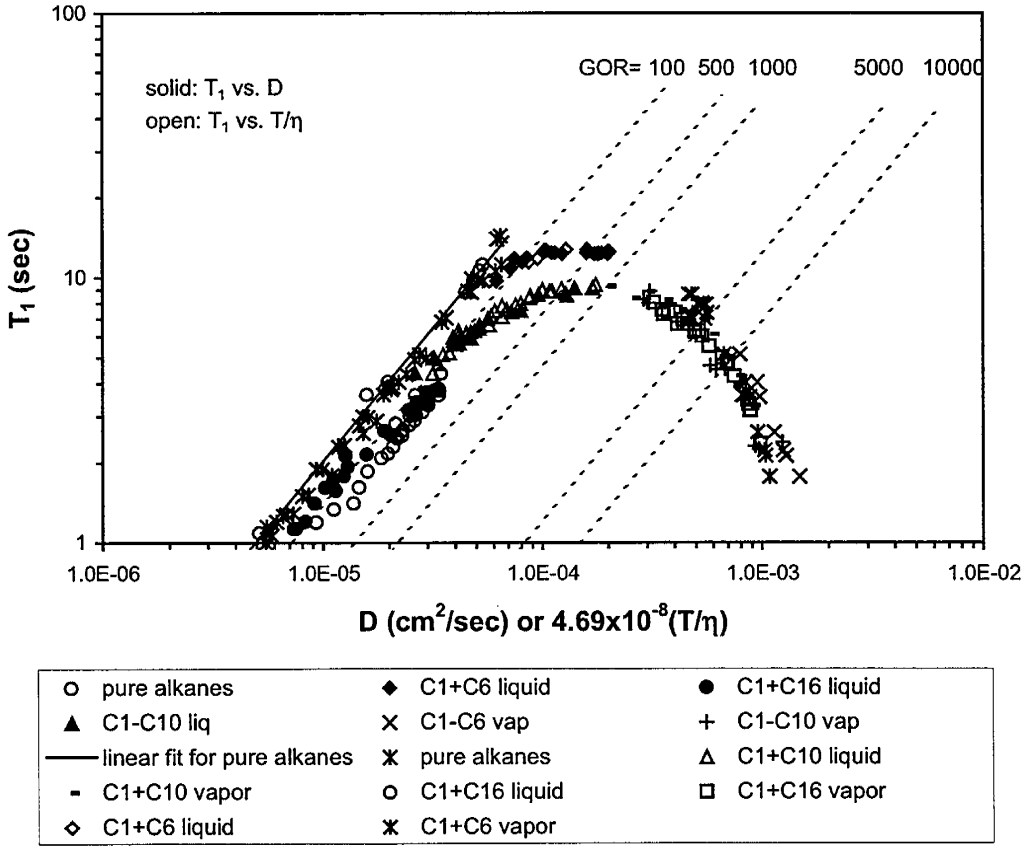

Fig. 9. T_1 vs. D and T_1 vs. T/η on the same plot

Conclusions

The 90 MHz NMR apparatus was restored and modified. After restoration, it could perform experiments at pressure up to 6000 psia and temperature from room temperature to 60°C.

The relaxation times and diffusion coefficients of pure alkanes and pure methane were measured. For pure higher alkanes, T_1 depends linearly on temperature/viscosity and diffusion coefficient on log-log plot.

For the first time, relaxation times of methane-n-alkane mixtures at elevated pressures and temperatures were measured. Three methane-n-alkane mixtures were measured, methane-n-hexane, methane-n-decane and methane-n-hexadecane. The linear correlations for pure alkanes do not hold for methane-n-alkane mixtures. The mixture data depart from linear correlation of pure alkanes due to the dissolved methane.

A mixing rule was developed for methane-n-alkane mixtures. It was assumed that the higher alkanes relax by intramolecular dipole-dipole interactions in the mixture, and methane relaxes by both intermolecular dipole-dipole interaction and spin-rotation interaction. The T_1 estimations from mixing rules and experimental results agree with one another.

Correlations of T_1 and transport properties (viscosity/T, GOR and diffusion coefficient) of methane-n-alkane mixtures were developed. The logarithm of the ratio of T_1 and $T_{1,linear}$ for given viscosity/temperature or diffusion coefficient correlates with the gas/oil ratio, independent of whether the oil is hexane, decane or hexadecane. Thus, T_1 can be expressed as a function of viscosity/temperature and gas/oil ratio. It can also be expressed as a function of diffusivity and gas/oil ratio. Diffusivity was found to be inversely proportional to viscosity/temperature regardless of composition, gas/oil ratio and temperature. Therefore, if any two of these properties, relaxation time (T_1), diffusion coefficient, gas/oil ratio and viscosity, are given, the other two can be estimated from the correlations.

References

Abragam, A., *Principle of Nuclear Magnetism*, Oxford University Pressure, New York, N. Y., **1961**

Beznik, F., *Corresponding States Correlations Relating Proton Spin-Relaxation Rates of Hydrocarbons to Viscosities at Advanced Pressures*, M. S. Dissertation, Rice University, **1994**.

Bloembergen, N., Purcell, E. M., and Pound, R. V., "Relaxation Effects in Nuclear Magnetic Resonance Adsorption," *Phys. Rev.*, 73(7), 679, **1947**

Carr, H. Y. and Purcell, E. M., "Effect of Diffusion on Free Precession in Nuclear Magnetic Resonance Experiments," *Phys. Rev.*, 94(3), 630, **1954**

Chuah, T., *Estimation of Relaxation Time Distribution for NMR CPMG Measurements*, M.S. Dissertation, Rice University, **1996**

C.R.E.P.S., *Viscosity and Density of Light Paraffins, Nitrogen and Carbon Dioxide*, Editions Technip-Paris, **1970**

Ely, J. F., and Hanley, H. J. M., "Predictions of Transport Properties," *Ind. Eng. Chem. Fundam.*, 20, 323, **1981**

Ertl, H., and Dullien, F. A. L., "Self-Diffusion and Viscosity of Some Liquids as a Function of Temperature," *AIChE Journal*, 19(6), 1215, **1973**

Etesse, P., *High Pressure NMR Study of CO_2 and Supercritical CO_2-n-hexadecane Mixtures*, Ph.D. Dissertation, Rice University, **1992**

Ferdrin, S., *Viscosity and Spin-Lattice Relaxation Time of Supercritical CO_2-n-Hexadecane Mixtures, and Molar Density and Isobaric Heat Capacity Ratios for Dense Fluids*, M. S. Dissertation, Rice University, **1995**

Gerritsma, C. J., Oosting, P. H., and Trappeniers, N. J., "Proton-Spin-Lattice Relaxation and Self-Diffusion in Methanes II. Experimental Results for Proton-Spin-Lattice Relaxation Times," *Physica*, 51, 381. **1971**

Gerritsma, C. J., and Trappeniers, N. J., "Proton-Spin-Lattice Relaxation and Self-Diffusion in Methanes I. Spin-Echo Spectrometer and Preparation of the Methane Samples," *Physica*, 51, 365, **1971**

Helbæk, M., Hafskjold, B., Dysthe, D.K., and Sϕrland, G.H., "Self-Diffusion Coefficients of Methane or Ethane Mixtures with Hydrocarbons at High Pressure by NMR," *J. Chem. Eng. Data* , 41, p.598, **1996**

Hirschfelder, J. O., Curtiss, C. F. and Bird, R. B., *Molecular Theory of Gases and Liquids,* John Wiley & Sons, New York, NY, **1954**

Huang, C., *Estimation of Rock Properties by NMR Relaxation Methods*, M.S. Dissertation, Rice University, **1997**

Kashaev, S. K., Le, B., and Zinyatov, M. Z., "Proton Spin-Lattice Relaxation, Viscosity, and Vibration of Molecules in the Series of *n*-Paraffins," *Doklady Akadmii Nauk SSSR*, 157, (6), 1438, **1964**

Kleinberg, R. L. and Vinegar, H. J., "NMR Properties of Reservoir Fluids," *The Log Analyst*, November-December, 20, **1996**

Knapstad, B.,Skjolsvik, P. A. and Oye, H. A., "Viscosity of the *n*-Decane. Methane System in the Liquid Phase," *Ber. Bunsenges Phys. Chem.*, 94, 1156, **1990**

Lee, A. L., Gonzalez, M. H., and Eakin, B. E., "Viscosity of Methane-*n*-Decane Mixtures," *J. Chem. Eng. Data*, 11, (3), 281, **1966**

Lo, S., Hirasaki, G. J., Kobayashi, R. and House, W. V., "Relaxation Time and Diffusion Measurements of Methane and *n*-Decane Mixtures," *The Log Analyst*, Nov-Dec, 43, **1998**

McConnell, J., *The Theory of Nuclear Magnetic Relaxation in Liquids*, Cambridge University Press, New York, **1987**

Morriss, C. E., Freedman, R., Straley, C., Johnston, M., Vinegar, H. J. and Tutunjian, P. N., "Hydrocarbon Saturation and Viscosity Estimation from NMR Logging in the Belridge Diatomite," *The Log Analyst*, 38, March-April, 44, **1997**

NIST Thermodynamic Properties of Hydrocarbon Mixture Database: *NIST Standard Reference Data Products Catalog* 1995-1996.

Oosting, P. H., and Trappeniers, N. J., "Proton-Spin-Lattice Relaxation and Self-Diffusion in Methanes III. Intrepretation of Proton-Spin-Lattice Relaxation Experiments," *Physica*, 51, 395, **1971**

Oosting, , P. H., and Trappeniers, N. J., Proton-Spin-Lattice Relaxation and Self-Diffusion in Methanes IV. Self-Diffusion in Methane," *Physica*, 51, 418, **1971**

Rajan, S., Lalita, K., and Babu, S. V., "Nuclear Spin-Lattice Relaxation in CH_4-Inert Gas Mixtures," *J. Magn. Reson.*, 16, 115, **1974**

Reamer, H. H., Olds, R. H., Sage, B. H., and Lacey, W. N., "Phase Equilibria in Hydrocarbon Systems," *J. Ind. Eng. Chem.*, 34(12), 1526, **1942**

Reamer, H. H., Opfell, J. B. and Sage, B. H., "Diffusion Coefficients in Hydrocarbon Systems, Methane-Decane-Methane in Liquid Phase," *Ind. Eng. Chem.*, 48(2), 275, **1956**

Shim, J. and Kohn, J. P., "Multiphase and Volumetric Equilibra of Methane – *n*-Hexane Binary System at Temperatures between -110° and 150° C," *J. Chem. Eng. Data*, 7(1), 3, **1962**

Stejskal, E. O. and Tanner, J. E., "Spin Diffusion Measurements: Spin Echoes in the Presence of a Time-Dependent Field Gradient," *J. Chem. Phys.*, 42(1), 288, **1965**

Tanner, J. E. and Stejskal, E. O., "Restricted Self-Diffusion of Protons in Colloidal Systems by the Pulse-Gradient, Spin-Echo Method," *J. Chem. Phys.*, 49(4) 1768, **1968**

Tutunjian, P. N. and Vinegar, H. J., "Petrophysical Applications of Automated High-Resolution Proton NMR Spectroscopy," *The Log Analyst*, March-April, 33, 136, **1992**

Zega, J. A., *Spin-Lattice Relaxation in Pure and Mixed Alkanes and Their Correlation with Thermodynamic and Macroscopic Transport Properties*, M. S. Dissertation, Rice University, **1987**

Zaga, J. A., *Spin-Lattice Relaxation in Normal Alkanes at Elevated Pressures*, Ph.D. Dissertation, Rice University, **1990**

Zega, J. A., House, W. V. and Kobayashi, R., "A Corresponding-States Correlations of Spin Relaxation in Normal Alkanes," *Physica A*, 156, 277, **1989**

Zega, J. A., House, W. V. and Kobayashi, R., "Spin-Lattice Relaxation and Viscosity in Mixtures of *n*-Hexane and *n*-Hexadecane," *Ind. Eng. Chem. Res.*, 29, 909, **1990**

Zhang, Q., Lo, S., Huang, C., Hirasaki, G. J., Kobayashi, R. and House, W. V., "Some Exceptions to Default NMR Rock and Fluid Properties,"39th Annual Logging Symposium, SPWLA, **1998**

Relaxation and Self-Diffusion Measurements of Pure Ethane at Ambient Temperature

Ying Zhang

Introduction

Nuclear magnetic resonance has been widely used for studies of molecular motion for a few decades. It can provide the information of spin-lattice relaxation time (T_1) and diffusion coefficient. Proton spin-lattice relaxation times and self-diffusion coefficients in ethane were measured at ambient and elevated temperatures and elevated pressures using an 89MHz NMR apparatus. The relationships between transport properties, temperature and relaxation times are discussed.

Spectrometers and Experimental Methods

The spectrometer used for NMR measurements is a high field, 89 MHz spectrometer with super-conducting magnet. The high-pressure probe operates up to 6000 psia. This spectrometer also has pulse field gradient capability for diffusion measurements. Pure ethane was measured at ambient temperature and elevated pressure. During the experiment, the ethane was brought to the desired pressure and then introduced into the sample probe for measurement.

For a component with the same type of protons, T_1 can be described as single exponential decay,

$$M(t) = M_0\left(1 - 2e^{-\frac{t}{T_1}}\right) \tag{1}$$

where M_0 is the magnetization of protons at equilibrium state, and M is the magnetization at time t.

For a single component, self-diffusion coefficient can be described as

$$M(\delta) = M_0 e^{-\gamma^2 D\delta^2\left(\Delta-\frac{\delta}{3}\right)g^2} \tag{2}$$

δ is length of gradient pulse, Δ is the time between two gradients, and g is gradient strength.

T_1 was measured by the inversion recovery method. The magnetization was first inverted by a 180° pulse from the positive z axis to the negative z axis. Then, after a delay t, a 90° pulse was applied to flip magnetization to the x-y plane, and the intensity was measured. The process was repeated for different values of t. Diffusion coefficients were measured by pulse-gradient spin-echo method. A 90° pulse was introduced and followed by a magnetic-field gradient pulse with strength g and of duration δ. Then, a 180° pulse was applied and followed by the second identical gradient pulse. The process was repeated with various δ and a set of δ and M can be collected.

Relaxation Time

Relaxation times of ethane at ambient temperature and elevated pressures were measured. The results were shown in Table 1.

Table 1 : Spin-lattice relaxation time at ambient temperature and various pressure								
T (°C)	19.4	19.3	20.3	19.9	20.4	20.0	19.6	19.8
P (psia)	433	495	538	572	658	990	1612	2344
T_1(sec)	7.202	7.276	19.037	20.387	20.057	22.099	21.243	22.008

Figure 1 is the plot of T_1 vs. pressure at ambient temperature. T_1 increases with the pressure at ambient temperature. One interesting observation is that T_1-P curve becomes flat when pressure is higher than 700 psia. It is not certain if this is due to the combination of spin-rotation and dipole-dipole relaxation processes or due to the effect of oxygen that may have passed through the oxygen scavenger.

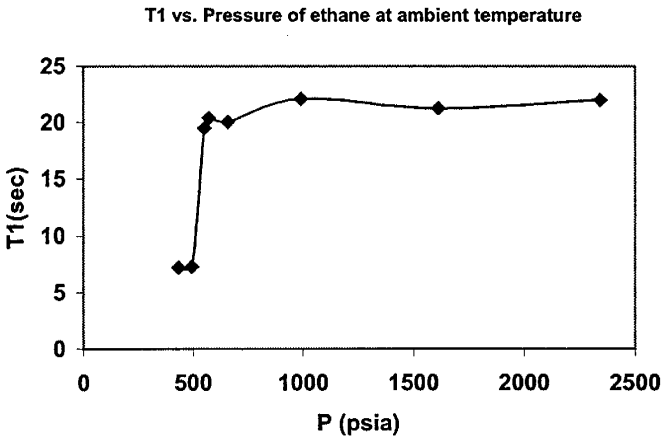

Figure 1: T_1 dependence on pressure at ambient temperature.

Figure 2 is the plot of relaxation time vs. viscosity/temperature for pure ethane, pure methane and other pure hydrocarbons. The viscosity of ethane was estimated by interpolating the viscosity data by Eakin et al.(1962). Previous work has shown that pure alkanes, alkane mixtures, viscosity standards and stock tank crude oils have NMR relaxation times that vary linearly with viscosity/temperature on a log-log scale. Sho-Wei Lo's work shows that pure methane at some temperatures and pressures does not follow the trend. Ethane's behavior is similar to that of methane. Pure ethane at some temperatures and pressures does not follow the linear relationship, either. Ethane and methane may relax by spin-rotation mechanism in addition to dipole-dipole interactions while other hydrocarbons relax only by dipole-dipole interaction. The spin-rotation mechanism has a different dependence on viscosity. As liquid ethane and liquid methane approach their critical points, they may relax by spin-rotation mechanism and they have the slope opposite that of liquid ethane and liquid methane at lower temperatures.

Figure 3 is the same data as Figure 2 except the relaxation time is plotted as a function of viscosity rather that viscosity/temperature. Surprisingly, it appears to correlate the data better. The cryogenic liquid methane and ethane data now are similar to the higher alkanes, even though theory has that it should be a function of viscosity/temperature.

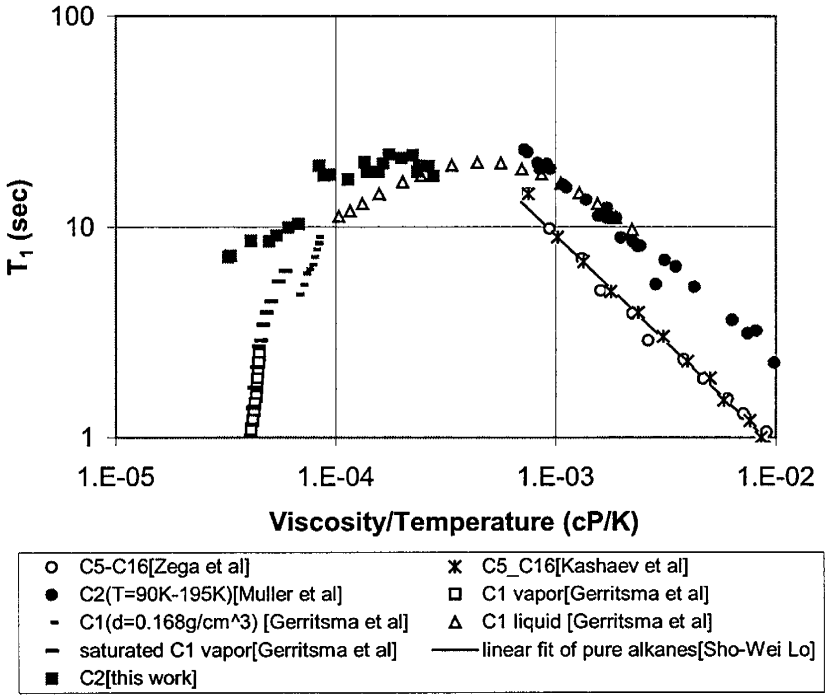

Figure 2. T_1 vs. viscosity/temperature plot of pure ethane and pure alkanes.

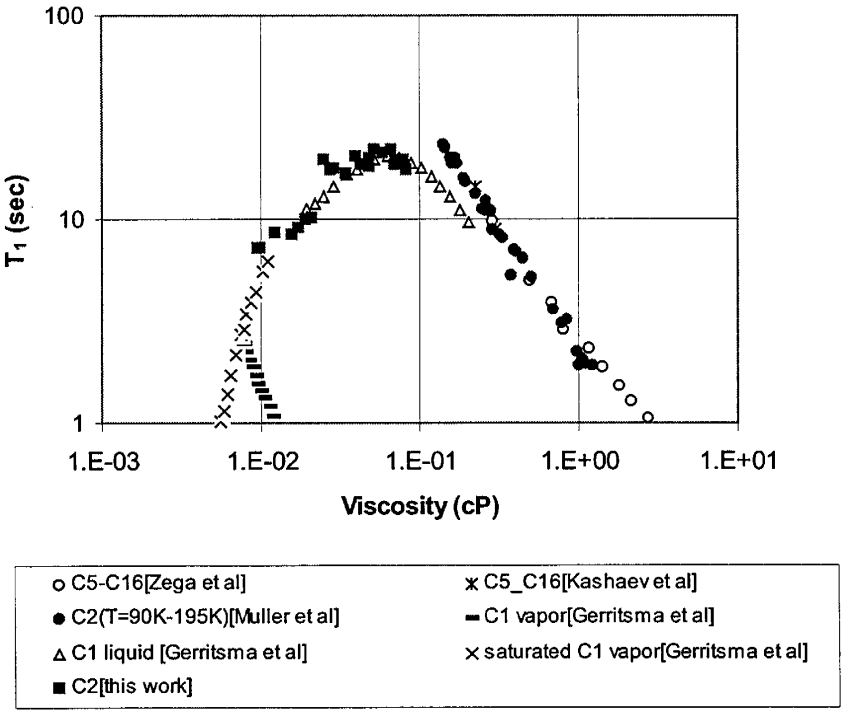

Figure 3. T_1 vs. viscosity plot of pure ethane and pure alkanes.

Diffusion Coefficients

Self-diffusion coefficients were also measured at ambient temperature and elevated pressure. The results were shown in Table 2. Figure 4 is the plot of Log D vs. pressure at ambient temperature.

Diffusion coefficient dependence of viscosity/temperature was plotted in Figure 5. According to Stokes-Einstein equation, diffusion coefficients have the following relationship with viscosity/temperature:

$$D = \frac{kT}{4\pi\sigma\eta} \tag{3}$$

where σ is characteristic length of the intermolecular potential. This relationship is applicable to all of the mixtures and pure alkanes. Diffusion coefficients are proportional to T/η, $D=5.05\times10^{-8}\times T/\eta$, where D is expressed in cm^2/sec, viscosity is expressed in cP and T is absolute temperature in K. These results are consistent with Stokes-Einstein equation.

Table 2 : Diffusion coefficients at ambient temperature and various pressure								
T (°C)	19.7	19.2	19.9	20.1	20.1	20.2	20.0	20.1
P (psia)	434	482	571	722	835	925	1560	2233
D(cm^2/s)	1.277E-3	6.052E-4	3.056E-4	2.562E-4	2.443E-4	2.352E-4	2.384E-4	2.319E-4

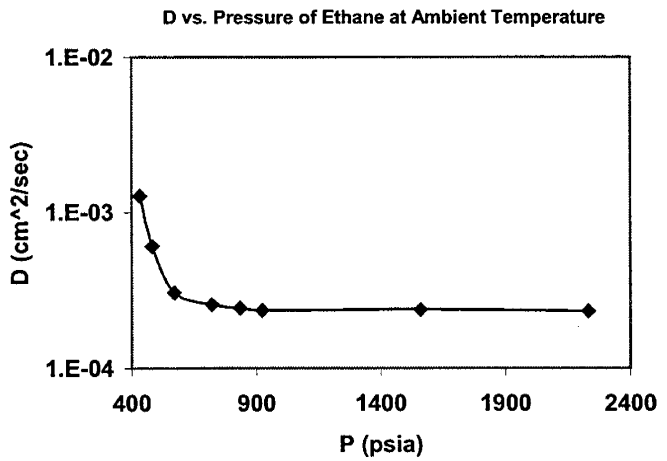

Figure 4. Diffusion coefficient dependence of pressure at ambient temperature.

Figure 6 is a plot of relaxation time versus diffusion coefficient. The higher alkanes are on a straight line with a slope of unity. Ethane, similar to methane-alkane mixtures, deviates from the correlation that applies to higher alkanes.

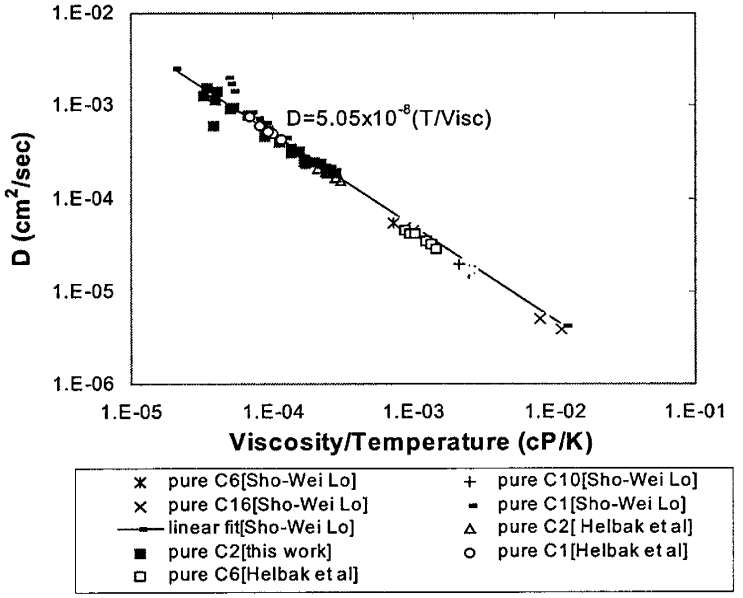

Figure 5. Diffusivity dependence on η/T for pure ethane and alkanes.

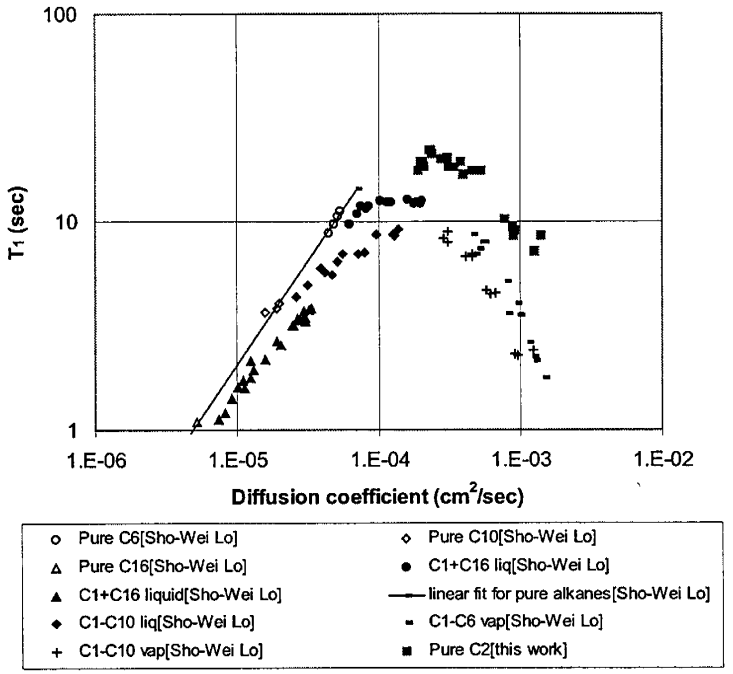

Figure 6. Relaxation time versus diffusion coefficient for pure ethane, pure higher alkanes, and methane-alkane mixtures.

Conclusion

T_1 and diffusion coefficients for ethane were measured at ambient and elevated temperature and elevated pressures. The relationships between transport properties, temperature and relaxation times were observed. The linear relationship between T_1 and η/T for pure alkanes does not hold for ethane. The result for the diffusion coefficients is consistent with Stokes-Einstein equation.

References

1. Gerritsma, C.J.; Oostin, P.H; Trappenier, N.J. "Proton-Spin-Lattice Relaxation and Self-Diffusion in Methanes II. Experimental Results for Proton-Spin-Lattice Relaxation Times," *Phsyca* **51** (1971) 381.
2. Helbak,M.; Hafskjold, B.; Dysthe, D. K.; Sorland, G. H.; "Self-Diffusion Coefficients of Methane or Ethane Mixtures with Hydrocarbons at High Pressure by NMR,". *J. Chem. Eng. Data* (1996), **41**, 598-603.
3. Muller, B. H.; J. D. Noble; "Proton Spin-Lattice Relaxation in Pure Liquid Ethane and Some of Its Deuterated Modifications," *Letters to the Editor* (1962), 777-779.
4. Wade, C. G.; Waugh, J. S.; "Temperature and Pressure Dependence of Self-Diffusion in Liquid Ethane," *J. Chem. Phys.* (1965), **43**, 3555-3557.
5. Harmon, J. F.; Muller, B. H.; "Nuclear Spin Relaxation by Translational Diffusion in Liquid Ethane," *Physical Review* (1969), **182**, 400-410.
6. Lo, Sho-Wei, *Correlations of NMR Relaxation Time with Viscosity/Temperature, Diffusion Coefficient and Gas/Oil Ratio of Methane-Hydrocarbon Mixtures*, Ph. D. Dissertation, Rice University, 1999.
7. Eakin, B. E.; Starling, K.E.; Dolan, J. P.; Ellington, R. T.; "Liquid, Gas and Dense Fluid Viscosity of Ethane," *J. Chem. Eng. Data* (1962), **7**, 33-36.

Sub-Task 1.4 Relaxation Time Distribution of Asphaltic Oils:

NMR Analysis of Crude Oil and Pure Hydrocarbon Fluids

Kelly Elizabeth McCann

Advisor
Dr. George Hirasaki

Participant
Abby Vinegar

Amoco Summer Internship

Rice University
Houston Texas
August 28, 1999

Purpose

The purpose of this ongoing study, my predecessors being Ariel Flores and Brandon H. E. Fleet, is to compile a database of the properties of various hydrocarbon samples. Such properties include NMR relaxation time, viscosity, density, asphaltene content, and hydrogen index. For a complete listing, please refer to Appendix A, Table 1. The relaxation time distributions are shown in Appendix B. The crude oil samples analyzed thus far include SMY, SMP, SMT, SM, M13, M11, SMID, M4, M14, SNS, Diluted Bitumen, SMP69, North Burbank, M2, M1, SWCQ, and M10. The pure hydrocarbons analyzed include toluene, 1-methylnaphthalene, hexadecane, squalene, 1-phenyldodecane, and decahydronaphthalene. In an attempt to construct a model similar to crude oils with variable asphaltene content, four solutions of polystyrene dissolved in toluene were made and tested. The solutions were 5%, 10%, 20%, and 43% polystyrene by mass dissolved in toluene. It was expected that each sample would act as a single compound with one distinct peak, which would change with the amount of polystyrene dissolved in the toluene. For the relaxation time distributions, please refer to the figures of Appendix B.

Equipment

Crude oil samples, pure hydrocarbons, and the solutions of polystyrene dissolved in toluene were tested in 5 or 10 mL volumetric flasks using a Resonance Instruments Maran NMR spectrometer housing a permanent magnet of 2 MHz resonance frequency. The temperature within the spectrometer is maintained at 30 ° C.

NMR Procedure

Samples that appeared to contain water droplets when looked at under a microscope, such as Diluted Bitumen and M10, were centrifuged at 20000 rpm for 1 hour to remove excess water.

5 and 10 mL volumetric flasks were thoroughly cleaned with toluene and followed with acetone for rapid drying under ambient conditions. Using disposable pipettes, samples were measured into the flasks. To remove oil that stuck to the column of the flask, a CHEMWIPE was wrapped around a pipette, which was then inserted and revolved within the flask. The flask was then capped, labeled, and saran-wrapped to prevent evaporation.

After placing the sample in a 30° C oven or the spectrometer for at least 30 minutes to allow it to come to 30° C, the Setup utility was used to calibrate the gain, frequency, pulse, and delay of the system automatically. The utility P90P180 was used to tune the pulses manually.

After tuning, *CPMGROCK* was chosen from the utility menu for T_2 measurements. A wait time (TW) 4 to 6 times the maximum relaxation time was chosen. If the sample had not been measured previously, a *TW* of 6000 milliseconds or longer was set. T_2 short τ was set at 120 microseconds, and T_2 long τ was set at 1000 microseconds. Filter width was set to 0.1 MHz, *Dead1* was 60 microseconds, and *Dead2* was 20 microseconds. The number of echoes was determined using the equation $2^* \tau$ *(number of echoes)=(4 to

6)*(longest T_2 relaxation time). two hundred and fifty six scans were made at 100% gain. With larger samples, gain may have been automatically tuned to a number less than 100%. In such a case, a calibration sample was run at the same gain for hydrogen index calculations or a sample of a smaller volume was run at 100% gain.

For T_1 measurements, the T1A utility was employed. Filter width was changed to 0.01 MHz, *Dead2* was changed to 150 microseconds, and the number of scans was set to 128. Under *Define Tau,* the *First Value* was set to 0.01 ms, the *Last Value* was 10000 ms, and the number of steps was set to 50.

NMR raw data was saved on a diskette and imported into the MATLAB program *tmain* and a Fortran program written by previous graduate students for processing. Initially, α was automatically chosen by the *T1/T2* FORTRAN program. Later, the value of α was manually set to be 10 in order to be consistent. Printouts were made of figures 1 and 2 from t-pre and figures 2 and 3 from t-post for future reference. The data was then transferred into Excel to produce T_2 short, T_2 long, and T_1 relaxation time distributions on the same plot. A simple MATLAB program called *Peak* was written to analyze 3 to 6 data points around the peak of a distribution from Excel. The points were fitted to a quadratic equation to find the maximum time and amplitude of the peak.

When more than one NMR measurement of a sample was done, the log mean, sum of *fs*, and other numerical data was averaged.

Crude Oil Results

T_2 short and long distributions have the same leading edge, but the T_2 short tend to have broader distributions. This is a result of the inability to acquire data before the first echo (at 2 milliseconds) when τ is set to one millisecond for T_2 long. Thus, early relaxation information that is recorded in a T_2 short measurement cannot be recorded in the T_2 long. The relaxation time plots in Appendix B show only the T_2 short measurements (in addition to the T_1 measurements) since they provide the same information as T_2 long measurements, in addition to early information.

More viscous oils tend to have shorter relaxation times.

T_1 distributions for the oils tend to be shifted toward the right of the T_2 distributions, thus having a longer relaxation time at the leading edge and peak relaxation time, see Fig. 1. It has been observed that those samples with higher asphaltene contents tend to exhibit a greater shift between T_1 and T_2. When T_1/T_2 peak vs. percent asphaltene content for crude

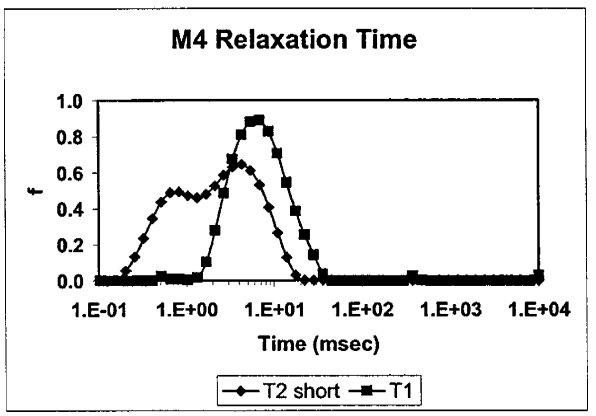

Fig. 1. T_1 and T_2 short relaxation distributions of M4 crude oil.

oils and pure hydrocarbons is plotted, a linear correlation is apparent. The greater the asphaltene content, the greater the shift between the peaks of the T_1 and T_2 distributions, see Fig. 2.

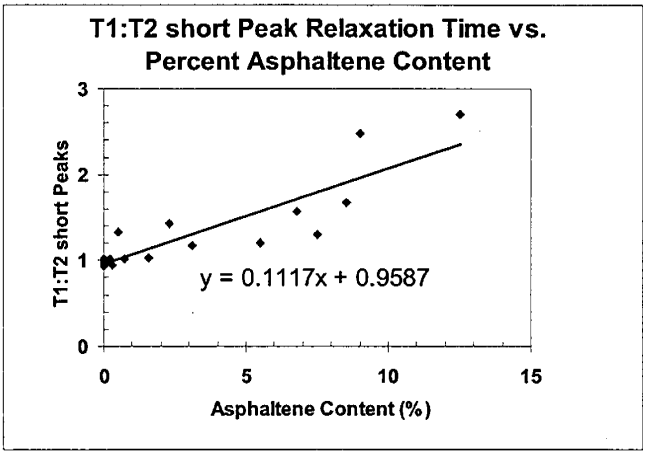

Fig. 2. Shift of T_1 and T_2 distributions as a function of asphaltene content.

Pure Hydrocarbon Results

Pure hydrocarbon distributions differ from those of the crude oils in that their relaxation time distributions are only a single peak (disregarding artifact from noise), Fig 3.

The T_1 and T_2 leading edge relaxation time and peak are located at approximately the same time, with only 2.6% difference on average. This is in keeping with the observation of a possible relationship between T_1/ T_2 peak shift and asphaltene content. These hydrocarbons do not contain asphaltenes, and no shift in the leading edge is observed.

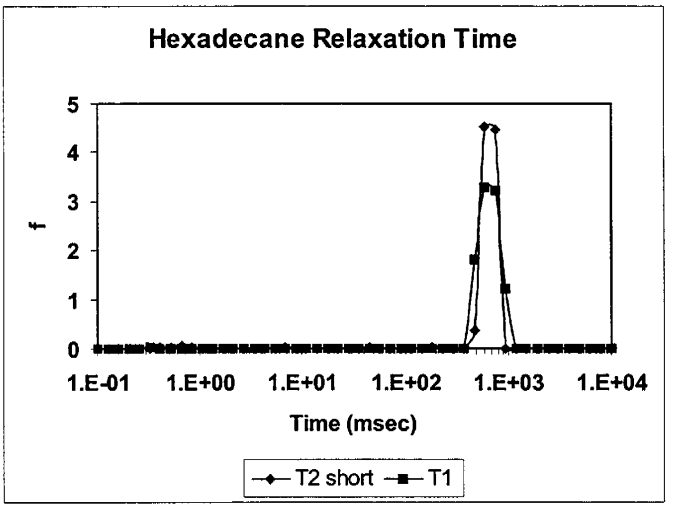

Fig. 3. Relaxation time distributions for a pure hydrocarbon, n-hexadecane.

Polystyrene in Toluene Results

There are two distinct regions of distribution peaks: two small peaks are between 10 and 100 milliseconds (attributed to the polystyrene) and one sharp, tall peak is at about 2000 milliseconds (attributed to the toluene), see Fig. 4. The amplitude, broadness, and location of the

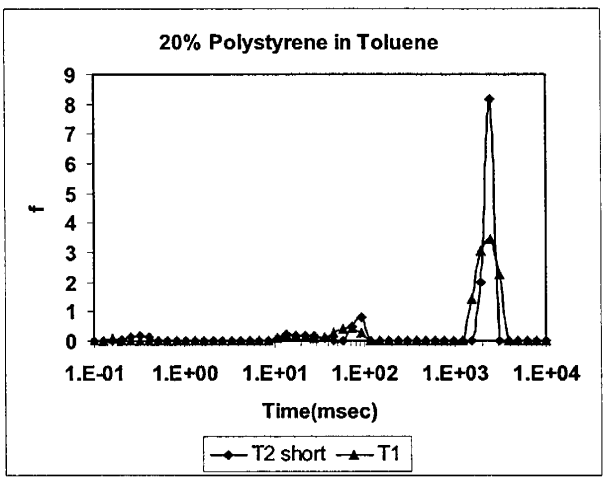

Fig. 4. 20% polystyrene in toluene.

toluene peak are as if the sample is the pure toluene and does not change in the presence of the polystyrene. The amplitudes of the two peaks attributed to the polystyrene increase in direct proportion to the amount of polystyrene in the sample. Manually doing a cumulative fs of the two smaller polystyrene peaks of the 20% solution, it was found that these peaks were about 21.3 % of the total distribution. For the 43% solution, the polystyrene peaks were about 42.3% of the total. Thus, the assumption that the peaks earlier in the distribution are directly proportional to and can be accounted for by the amount of polystyrene was confirmed.

Density

A 10 mL or 25 mL specific gravity flask is placed on the electronic balance. After the balance is tared, the vial is filled with the hydrocarbon to be measured and the capillary stopper is put in place. Excess fluid is wiped from the top and the outside of the flask. The flask is weighed at room temperature and the weight is recorded. The sample is then placed in a 30° C oven for at least an hour and a half. Since the fluid expands, excess fluid seeps out of the capillary stopper. After wiping the excess fluid from the glass, a second weight is recorded for use in the database. Density is calculated recorded in grams per mL.

Hydrogen Index, *HI*

The HI was determined by dividing the sum of the amplitudes of the T_2 short distribution with that of the same volume of the calibration sample. It was discovered that the reproducibility of the HI measurements was poor because of the lack of reproducibility of the sum of the amplitudes of the calibration samples. The latter problem is due to the oscillations of the early echos. If the first echo is above the trend, it is interpreted as a short relaxation time component. If the first echo is below the trend, it does not contribute to the relaxation time distribution. Thus the reported *HI*s were normalized with respect to the average amplitude of a number of calibration samples.

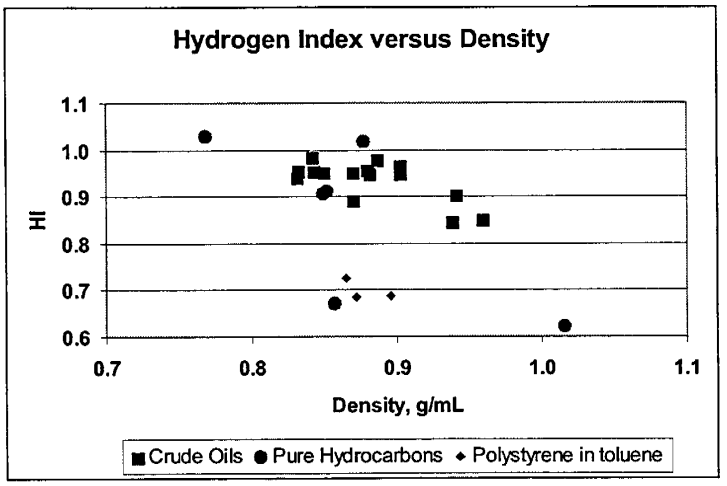

Fig. 5. *HI* of crude oils, pure hydrocarbons, and polystyrene in toluene.

H:C Ratio

Calculation

H:C ratio was calculated using the following equation taken from "Some Exceptions to Default NMR Rock and Fluid Properties":

$$\frac{1.333\,HI}{\rho - 0.112\,HI}$$

HI is the hydrogen index using the average sum fs of all the calibration samples and ρ is density in g/mL.

Results

When *H:C* ratio vs. density at 30°C is plotted, a linear correlation is apparent. Please refer to Figure 6. The greater the density of a sample, the lower the *H:C* ratio. For example, 1-methyl naphthalene's density of 1.016 g/mL corresponded to a *H:C* of 0.87, while hexadecane's density of 0.768 g/mL corresponded to a *H:C* of 2.10.

For the pure hydrocarbons, the deviation of the experimentally calculated *H:C* ratios from their real values ranged from 0.011 to 0.034, see Fig. 7. Thus, it can be assumed that there is a similar deviation in calculated *H:C* ratio from the actual value for the crude oils.

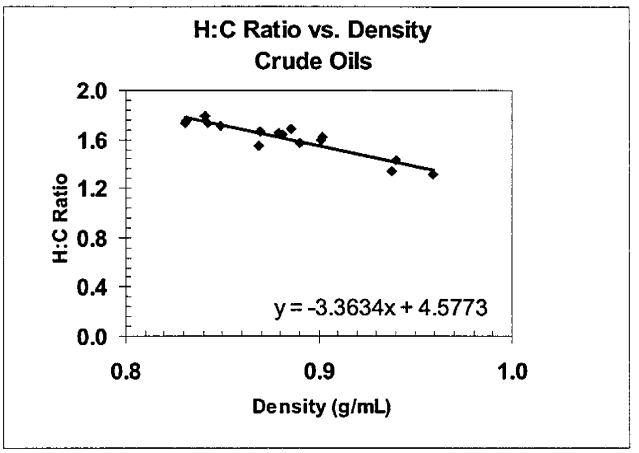

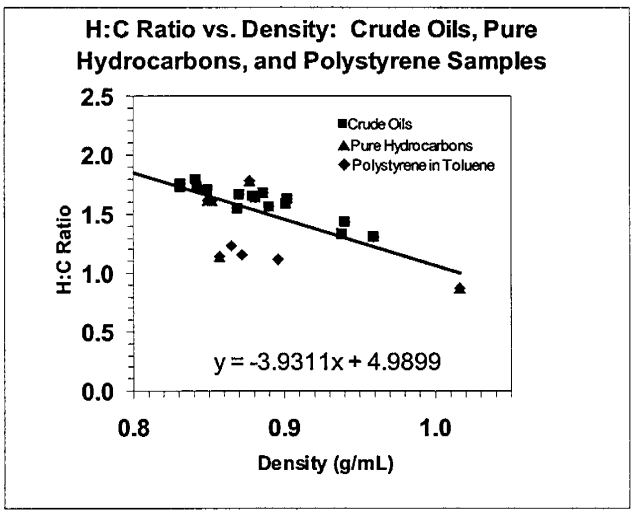

Fig. 6. *H:C* ratio correlated with density.

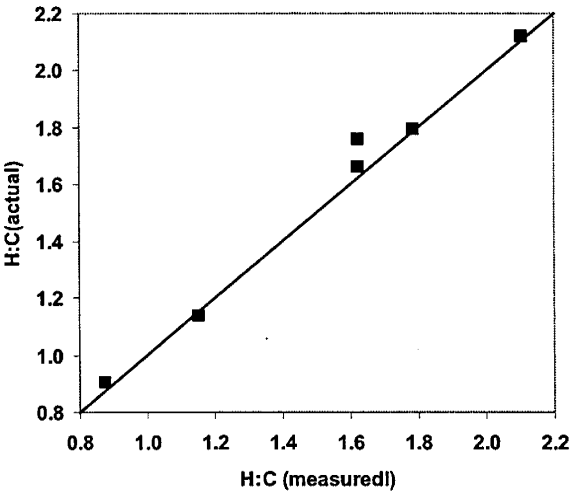

Fig. 7. Comparison of measured *H:C* to actual value for pure hydrocarbons.

Viscosity

Procedure

Abby Vinegar and I used a digital Brookfield viscometer to determine the viscosity of the crude oils and other samples. Sixteen mL of the sample to be tested is placed in the cylindrical metal container, the spindle is attached and carefully lowered into the container without touching its sides, and the motor responsible for rotating the spindle is turned to the highest speed setting that will give a meaningful digital reading. After recording the viscosity in cp at room temperature, the container is submerged in a water bath to maintain a constant temperature of 30°C and a second reading is taken.

Results: Viscosity and T_2 short Log Mean Correlation

When the T_2 short log mean relaxation time of the crude oils is plotted against their viscosities at 30°C in cp (refer to Figure 8), the equation for the best-fit line through the data points gives:

$$T_{2,LM} = \frac{1225}{\eta^{0.95}}, \qquad R^2 = 0.85$$

The literature equation (Morriss, et al., 1997), for which samples were tested at 25 ° C, was found to be:

$$T_{2,LM} = \frac{1200}{\eta^{0.9}}$$

All the crude oils and hydrocarbons taken together, the equation becomes:

$$T_{2,LM} = \frac{1795}{\eta^{1.04}}, \qquad R^2 = 0.88$$

The polystyrene solutions in toluene do not follow the viscosity correlation. The relaxation time of toluene remain approximately the bulk value even for the extremely viscous solutions.

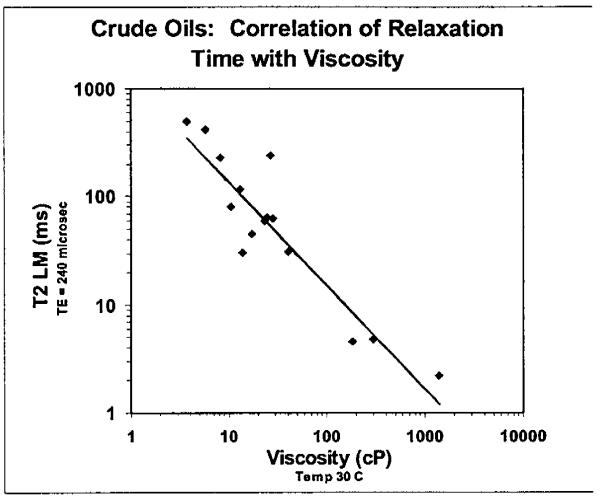

Fig. 8. Correlation of crude oil viscosities at 30°C.

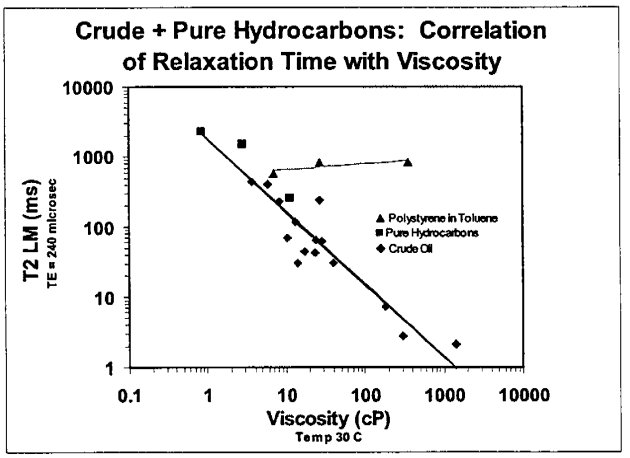

Fig. 9. Correlation of crude oil and pure hydrocarbon viscosities. Polystyrene solutions are shown for comparison.

Discussion of Results

The original objective of this investigation was to resolve the long tail in the relaxation time distributions. It was hypothesized that this tail was caused by the large molecular components such as the asphaltenes. These large molecules will have longer rotational correlation times and thus can be expected to have faster relaxation rates. If the correlation time approaches or exceeds the period of the Larmor frequency, then the system is no longer in the *extreme narrowing limit* and the T_1 is expected to be larger than the T_2 for these components. Thus we expected the short T_2 components in the tail of the distribution to be increased to longer T_1 values. In another words, the T_1 distribution was expected to have less of a tail. Some of the samples with the largest asphaltene content, M14, M13, and M4, show the entire T_1 distribution shifted to longer relaxation times compared to the T_2 distribution. On the other hand, other crude oils with moderately high asphaltene content, M10, SMID, and SMY, shows the leading edge and peak shifted but the shift in the tail is not so apparent. Thus the peak value was used to quantify the shift to correlate with the asphaltene content. If this shift is indeed due to the larger molecular components not being in the *extreme narrowing limit*, we expect to see a larger shift with a higher Larmor frequency. Thus we are making measurements in a high field spectrometer.

The finding that the *HI* decreases with increasing density of the crude oils and pure hydrocarbons at ambient conditions is consistent with our earlier claim that the *HI* of hydrocarbons is determined exactly by the density and *H:C* ratio and the correlation of the measured *HI* of Kleinberg and Vinegar (1996) with API gravity. Hydrocarbons with lower *H:C* ratio tend to have a higher density at ambient conditions. Our finding is in contrast to that of LaTorraca, et al. (1999) who claim that the *HI* is equal to 1 unless the viscosity is greater than 10,000 cp. Even then, their lowest *HI* determined by combustion was 0.95. Some of our most viscous oils such as M14 may have lost some of the signal due to the echo spacing limitation. However, the *HI* of toluene and 1-methylnaphthalene are 0.672 and 0.621, respectively and loss of signal do not occur with these pure hydrocarbons.

The solutions of polystyrene in toluene do not follow the viscosity correlation. The relaxation time of toluene remains near that of the pure fluid, even for the extremely viscous solutions. The area under the polystyrene peaks accounts for the quantity of polystyrene in the solution and the relaxation time gets shorter with increasing concentration and viscosity.

Conclusions

There is a shift between the T_1 and T_2 distributions that correlates with the asphaltene content.

HI significantly less than 1.0 is observed for heavy crude oils and pure hydrocarbons. Some loss of signal due to echo spacing may have occurred for the former but not for the latter.

The crude oil viscosity/T_2 log mean correlation is close to that in the literature. Deviation could be a result of an insufficient number of data points or

a result of the different temperatures (30°C for the tested samples versus 25°C for the literature values) at which viscosity was tested.

The polystyrene in toluene samples do not follow the viscosity correlation. The toluene peak forces the log mean to stay near the same value while the viscosity increases rapidly with the percentage of polystyrene dissolved.

References

Chuah, T.-L. *Estimation of Relaxation Time Distribution for NMR CPMG Measurements.* MS Thesis. Rice University, August *1996.*

Flores, Ariel. "Analysis of Bulk Oil Fluid." CENG *500* Project. Rice University, December *9, 1998.*

Fleet, Brandon. "Analysis of Crude Oil Samples." CENG *500* Project. Rice University, May *6,* 1999.

Huang, C.-C. *Estimation of Rock Properties by NMR Relaxation Methods.* MS Thesis. Rice University, August *1997.*

Kleinberg, R. L. and Vinegar, H. J., "NMR Properties of Reservoir Fluids," The Log Analyst, Nov.-Dec., 1996, 20-32.

LaTorraca, G. A., Stonard, S. W., Webber, P. R., Carlson, R. M., and Dunn, K. J., "Heavy Oil Viscosity Determination Using NMR Logs," paper PPP presented at the SPWLA 40th Annual Logging Symposium, May 30-June 3, 1999.

Morriss, C. E., Freedman, R., Straley, C., Johnston, M., Vinegar, H. J., Tutunjian, P. N. "Hydrocarbon Saturation and Viscosity Estimation from NMR Logging in the Belridge Diatomite," *The Log Analyst, 1997. p. 44-59.*

Zhang, Q., Lo, S.-W., et al. "Some Exceptions to Default NMR Rock and Fluid Properties." Rice University.

APPENDIX A: Table 1. Crude oil and pure hydrocarbon properties

Sample	Asphaltene Content (%)	Density at 30 C (g/cm^3)	Viscosity at 30 C (cp)	HI (using avg CuSO4 fs)	Hydrogen: Carbon ratio at 30 C	T2 short Log Mean (msec)	T1 Log Mean	T2 short Peak (msec)	T1 Peak (msec)	T1:T2 short Peak Ratio
M14	12.50			0.648		0.5	4.7	0.5	1.4	2.70
SNS		0.843	26.50	0.955	1.73	243.7	336.7	560.8	648.1	1.16
Diluted Bitumen		0.886	14.00	0.980	1.68	30.8	83.5	158.3	251.9	1.59
M13	9.00	0.938	302.00	0.847	1.34	2.8	9.8	5.1	12.7	2.48
SM		0.849		0.953	1.71	92.2	121.2	221.2	249.0	1.13
SMP69		0.870	13.10	0.954	1.67	118.3	131.3	241.3	291.7	1.21
SMP	3.10	0.940	184.00	0.902	1.43	7.2	11.0*	18.7	24.3**	1.29
SMT	2.30	0.890	40.60	0.924*	1.57	30.9*	49.5*	81.5**	116.9**	1.44
SMY	5.50	0.881	23.40	0.951	1.64	43.7	79.7	160.0	191.7	1.20
SMID	7.50	0.869	10.50	0.893	1.55	70.1	144.4	210.0	272.3	1.30
North Burbank	0.30	0.841	8.28	0.984	1.80	230.6	246.6	444.1	422.7	0.95
M11	0.20	0.831	3.70	0.942	1.73	438.7	452.1	706.0	720.1	1.02
M2	0.50	0.831	5.78	0.954	1.76	413.6	364.5	577.2	765.9	1.33
M4	6.81	0.959	1400.00	0.851	1.31	2.1	6.9	4.0	6.3	1.56
M1	0.71	0.901	28.40	0.949	1.59	62.3	64.8	129.1	132.4	1.03
SWCQ	1.60	0.902	24.40	0.967	1.62	64.8	85.1	135.5	139.9	1.03
M10	8.54	0.879	17.20	0.957	1.65	45.3	101.4	192.4	320.0	1.66
1-Methylnaphthalene	0.00	1.016	2.82	0.621	0.87	1549.1	1499.0	1543.1	1574.3	1.02
1-Phenyldodecane	0.00	0.849		0.907	1.62	541.4	516.3	561.4	542.5	0.97
Decahydronaphthalene	0.00	0.877		1.017	1.78	953.2	1054.0	1078.5	1083.2	1.00
Hexadecane	0.00	0.768		1.028	2.10	552.9	635.5	666.8	654.8	0.98
Squalene	0.00	0.852	11.00	0.911	1.62	262.6	268.6	299.1	277.5	0.93
Toluene	0.00	0.857	0.82	0.672	1.15	2329.7	2241.5	2494.6	2478.0	0.99
5% Polystyrene in Toluene	0.00	0.865	6.96	0.725	1.23	578.0	1908.7			
10% Polystyrene in Toluene	0.00	0.872	26.40	0.685	1.15	835.5				
20% Polystyrene in Toluene	0.00	0.896	337.00	0.688	1.12	835.4	1049.2			
43% Polystyrene in Toluene	0.00					201.0	254.0			

* Brandon Fleet's Data

** Qian Zhang's data

APPENDIX B

Relaxation Time Distributions

Relaxation Time Distributions are on the following pages in this order:

Crude Oils:
M14
SNS
Diluted Bitumen
M13
SM
SMP69
SMP***
SMT***
SMY
SMY (Run 2)*
SMID**
North Burbank
M11
M2
M4
M1
SWCQ
M10

Pure Hydrocarbons:
Decahydronaphthalene
Hexadecane
1-Methylnaphthalene
1-Phenyldodecane
Squalene
Toluene

Polystyrene in Toluene:
5%
10%
20%
43%

* Please take note of distribution repeatability
** Please take note of distribution dependence on alpha
*** Q. Zhang's distributions

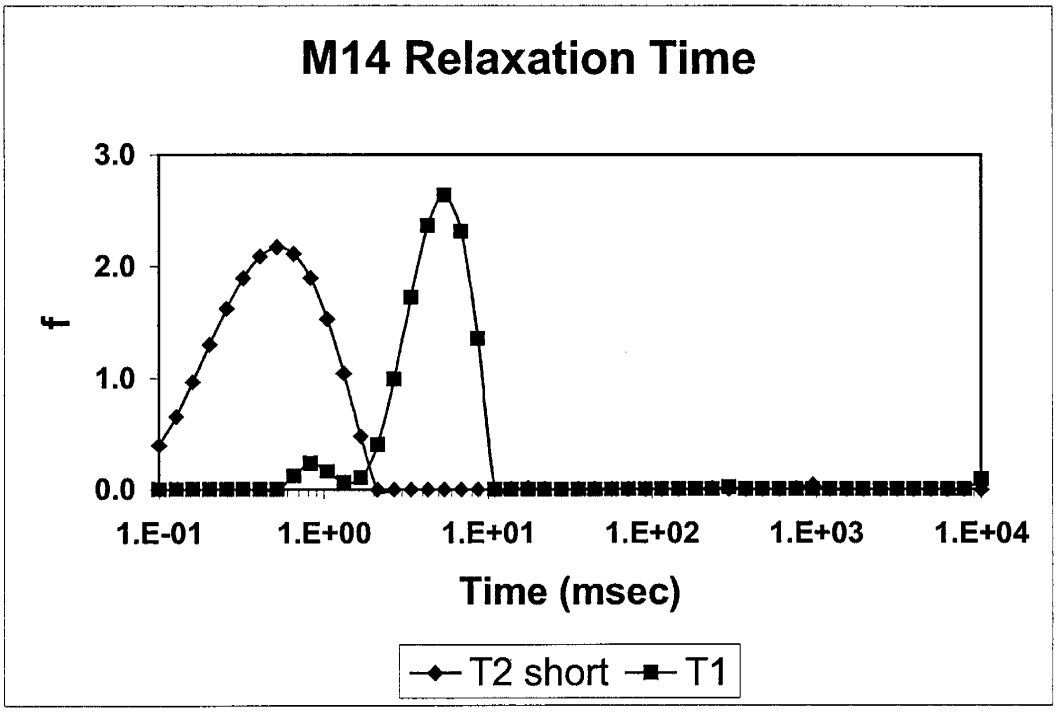
M14 Relaxation Time
3.0
2.0
1.0
0.0
f
1.E-01
1.E+00
1.E+01
1.E+02
1.E+03
1.E+04
Time (msec)
T2 short
T1

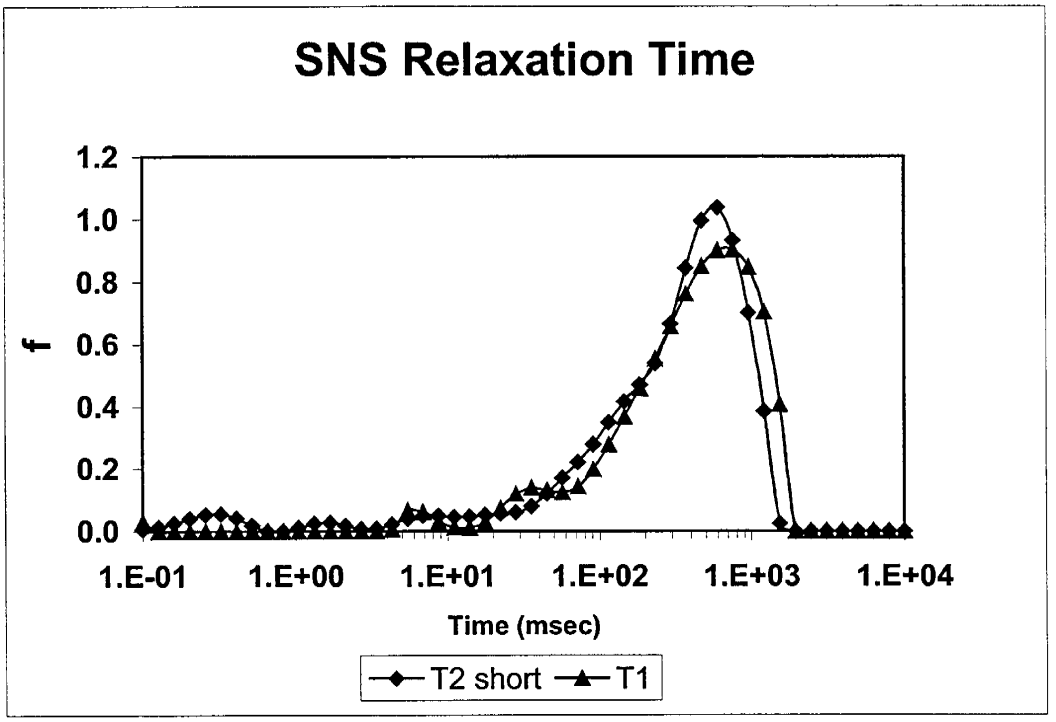
SNS Relaxation Time
1.2
1.0
0.8
0.6
0.4
0.2
0.0
f
1.E-01
1.E+00
1.E+01
1.E+02
1.E+03
1.E+04
Time (msec)
T2 short
T1

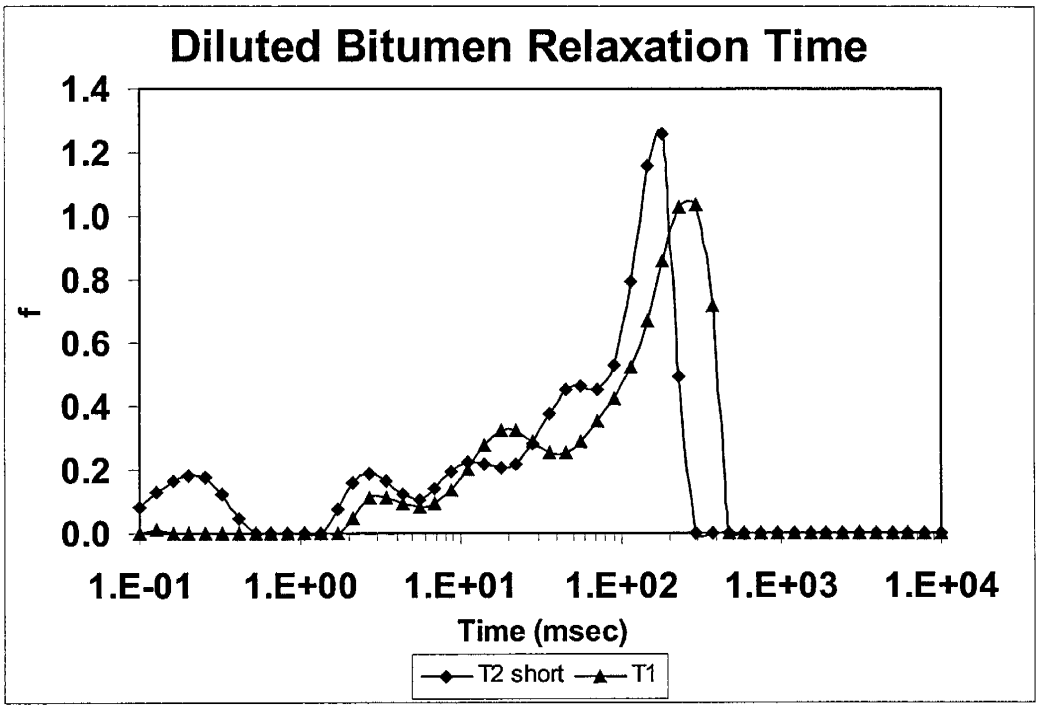
Diluted Bitumen Relaxation Time
1.4
1.2
1.0
0.8
0.6
0.4
0.2
0.0
f
1.E-01
1.E+00
1.E+01
1.E+02
1.E+03
1.E+04
Time (msec)
T2 short
T1

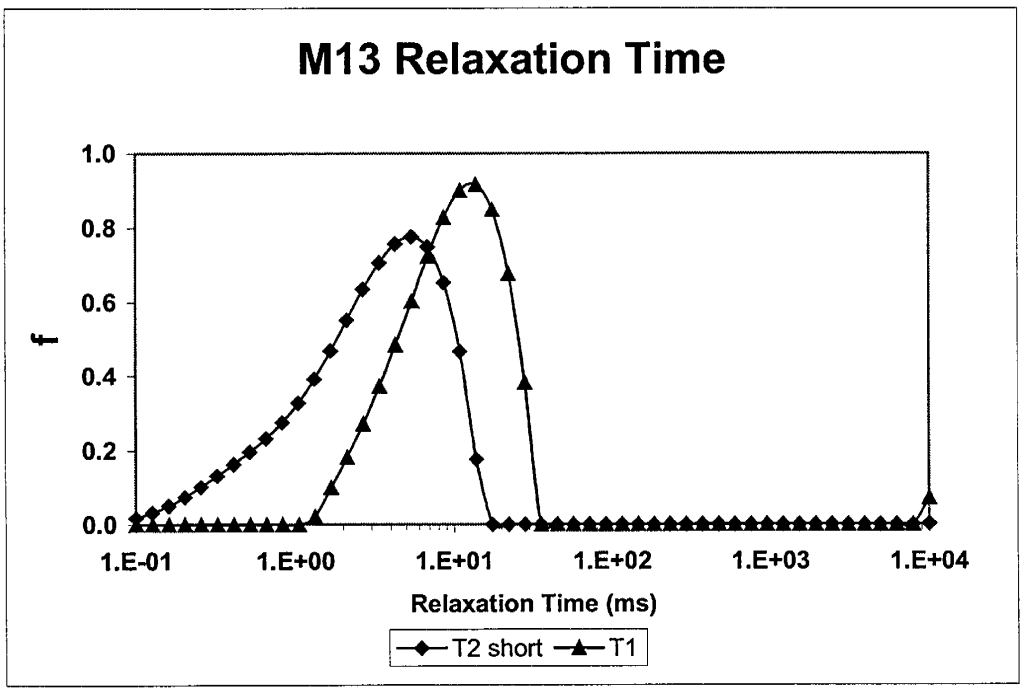
M13 Relaxation Time
1.0
0.8
0.6
0.4
0.2
0.0
f
1.E-01
1.E+00
1.E+01
1.E+02
1.E+03
1.E+04
Relaxation Time (ms)
T2 short
T1

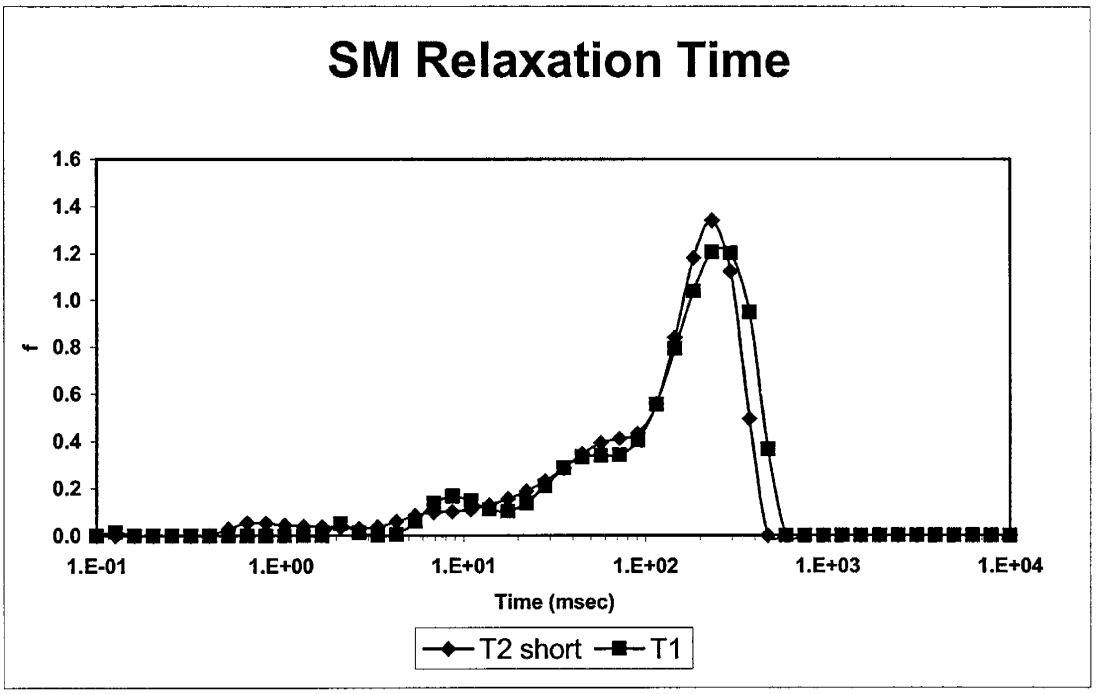
SM Relaxation Time
1.6
1.4
1.2
1.0
0.8
0.6
0.4
0.2
0.0
f
1.E-01
1.E+00
1.E+01
1.E+02
1.E+03
1.E+04
Time (msec)
T2 short
T1

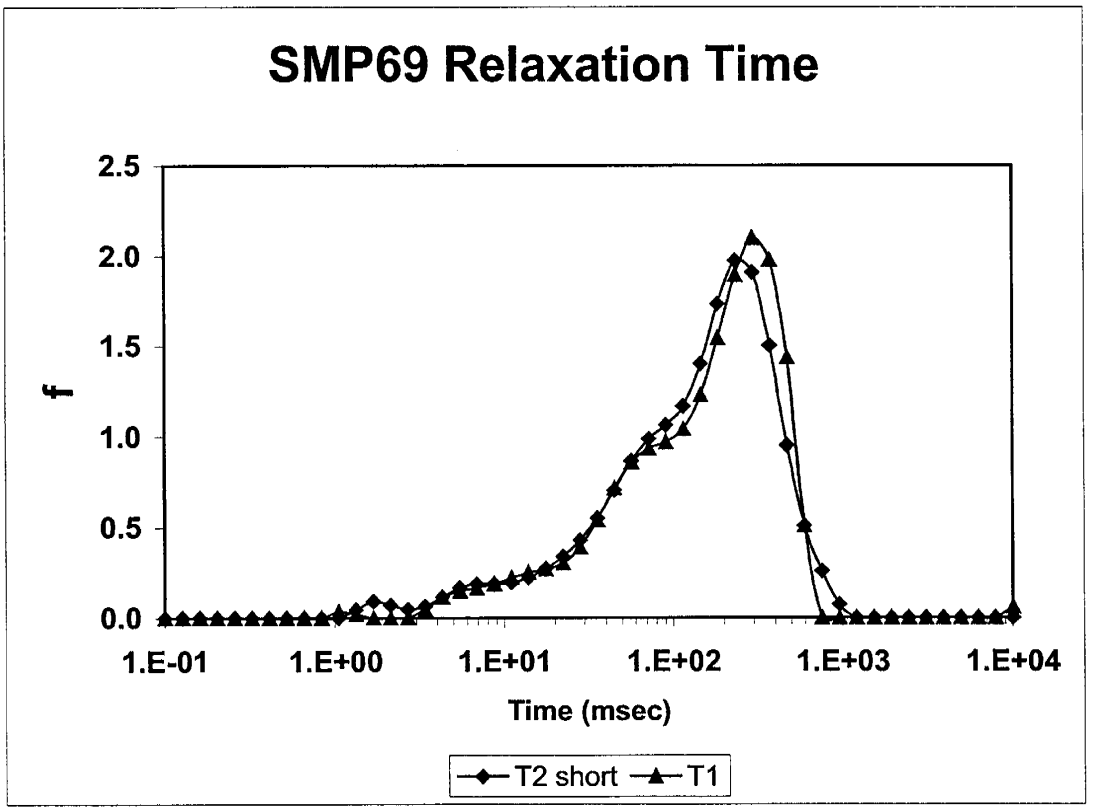
SMP69 Relaxation Time
2.5
2.0
1.5
1.0
0.5
0.0
f
1.E-01
1.E+00
1.E+01
1.E+02
1.E+03
1.E+04
Time (msec)
T2 short
T1

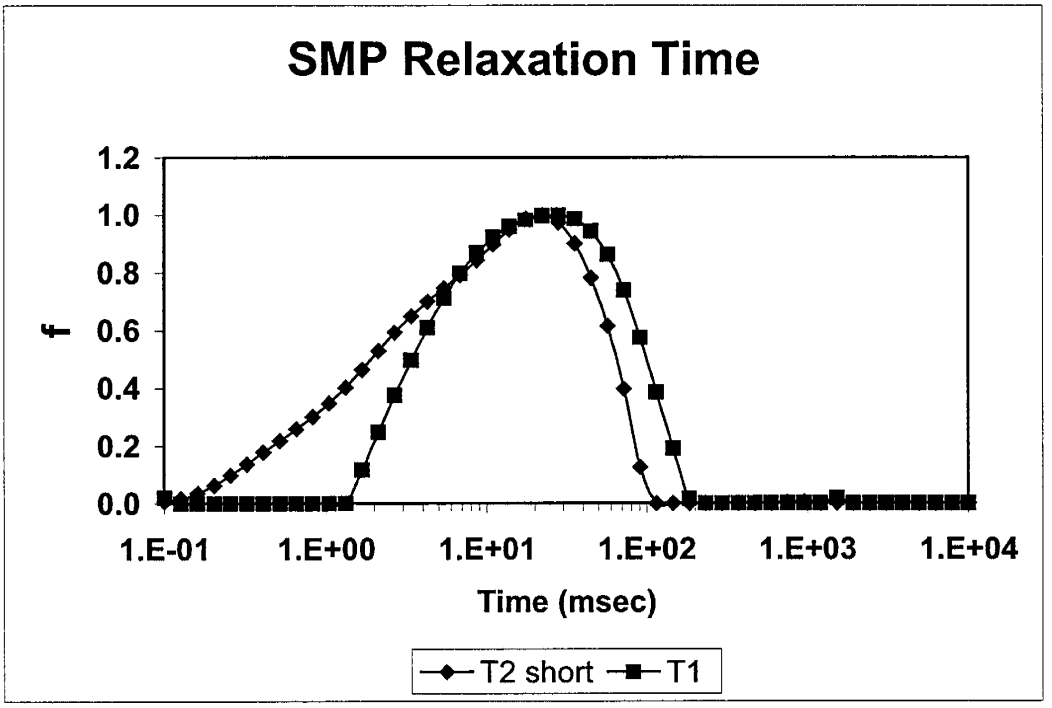
SMP Relaxation Time
1.2
1.0
0.8
0.6
0.4
0.2
0.0
f
1.E-01
1.E+00
1.E+01
1.E+02
1.E+03
1.E+04
Time (msec)
T2 short
T1

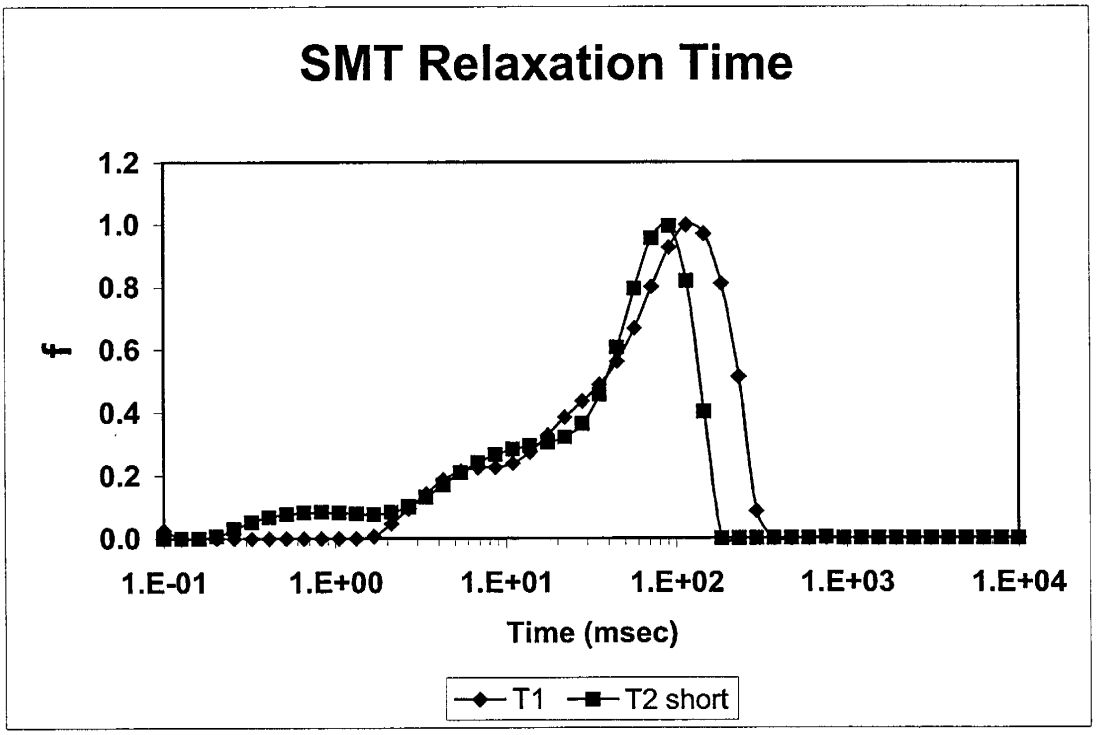
SMT Relaxation Time
1.2
1.0
0.8
0.6
0.4
0.2
0.0
f
1.E-01
1.E+00
1.E+01
1.E+02
1.E+03
1.E+04
Time (msec)
T1
T2 short

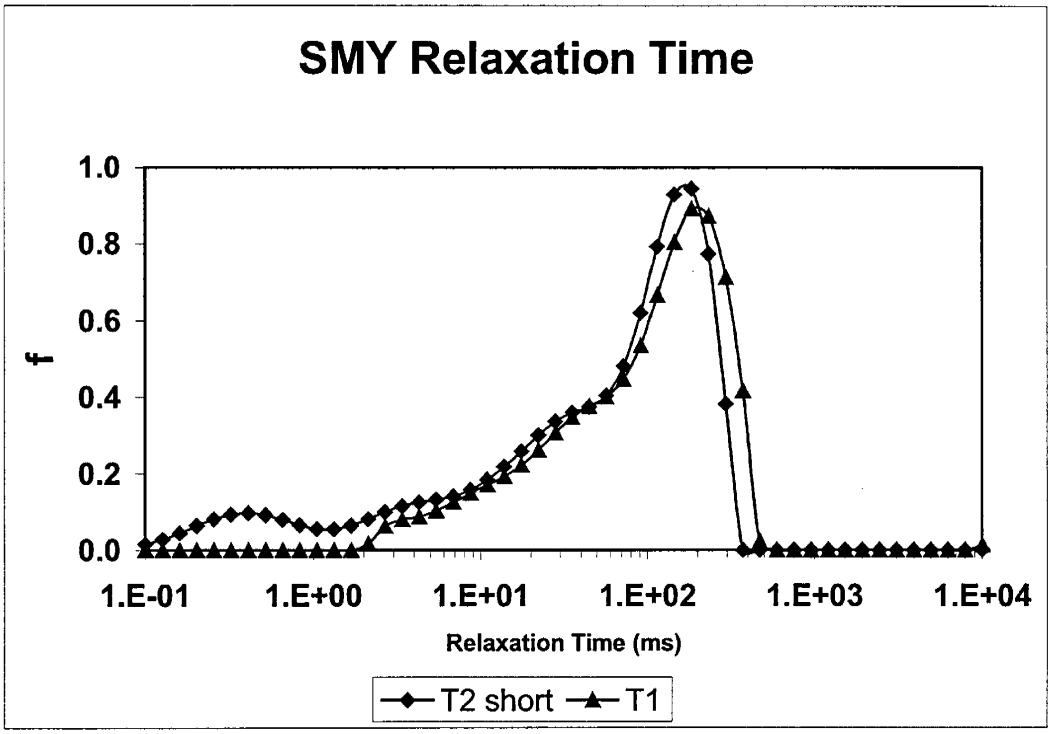
SMY Relaxation Time
1.0
0.8
0.6
0.4
0.2
0.0
f
1.E-01
1.E+00
1.E+01
1.E+02
1.E+03
1.E+04
Relaxation Time (ms)
T2 short
T1

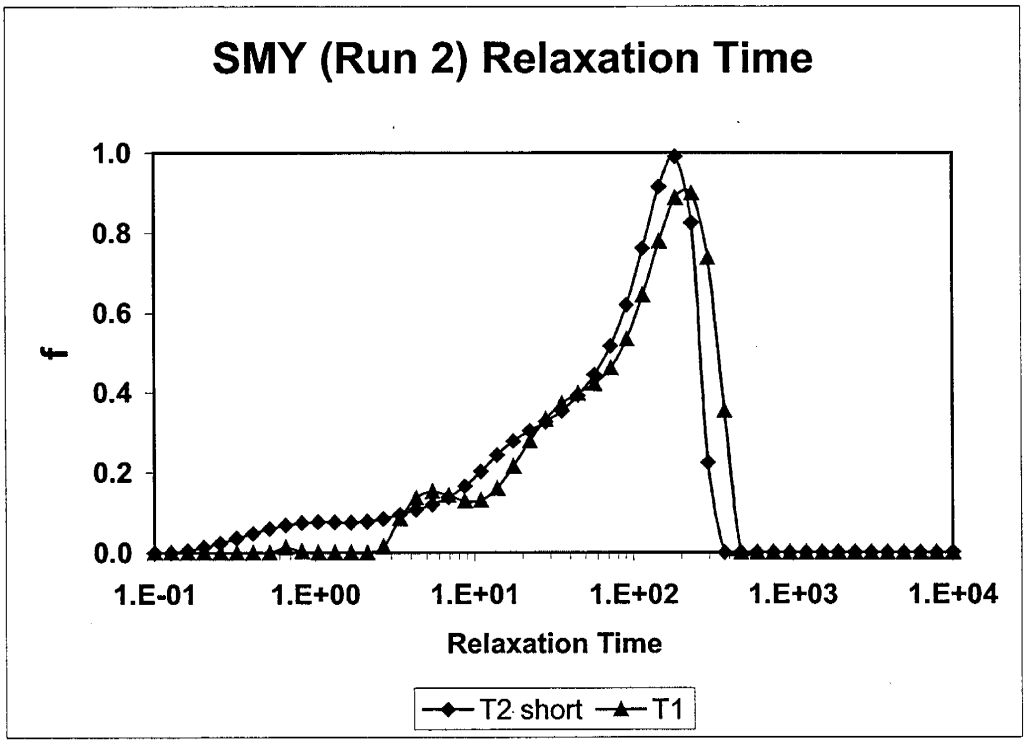
SMY (Run 2) Relaxation Time
1.0
0.8
0.6
0.4
0.2
0.0
f
1.E-01
1.E+00
1.E+01
1.E+02
1.E+03
1.E+04
Relaxation Time
T2 short
T1

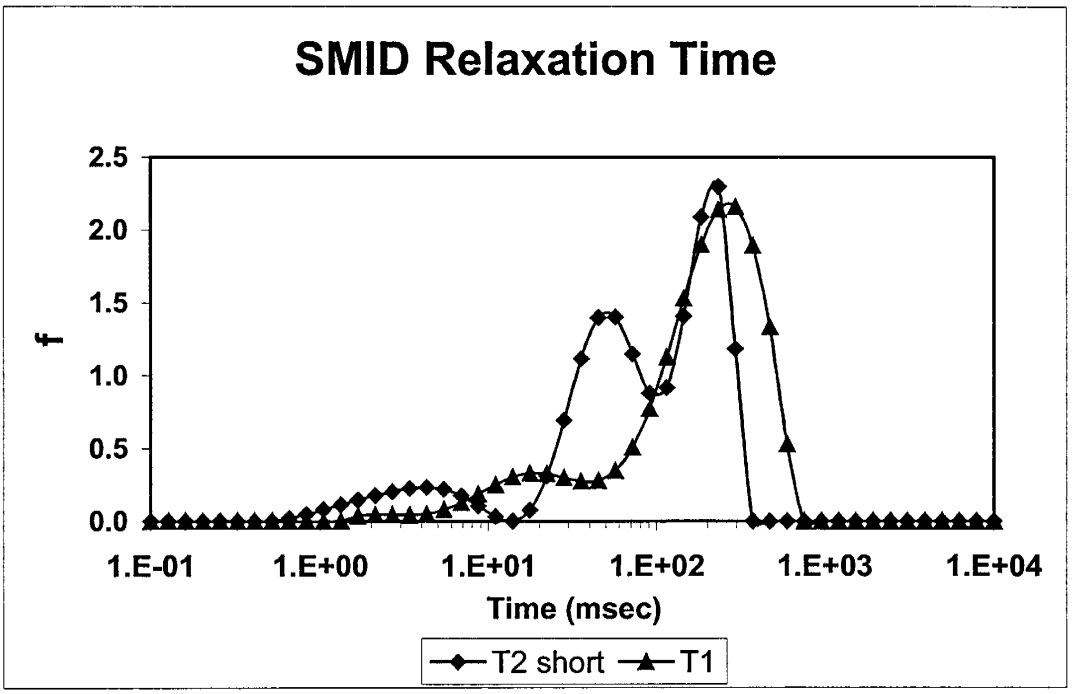
SMID Relaxation Time
2.5
2.0
1.5
1.0
0.5
0.0
f
1.E-01
1.E+00
1.E+01
1.E+02
1.E+03
1.E+04
Time (msec)
T2 short
T1

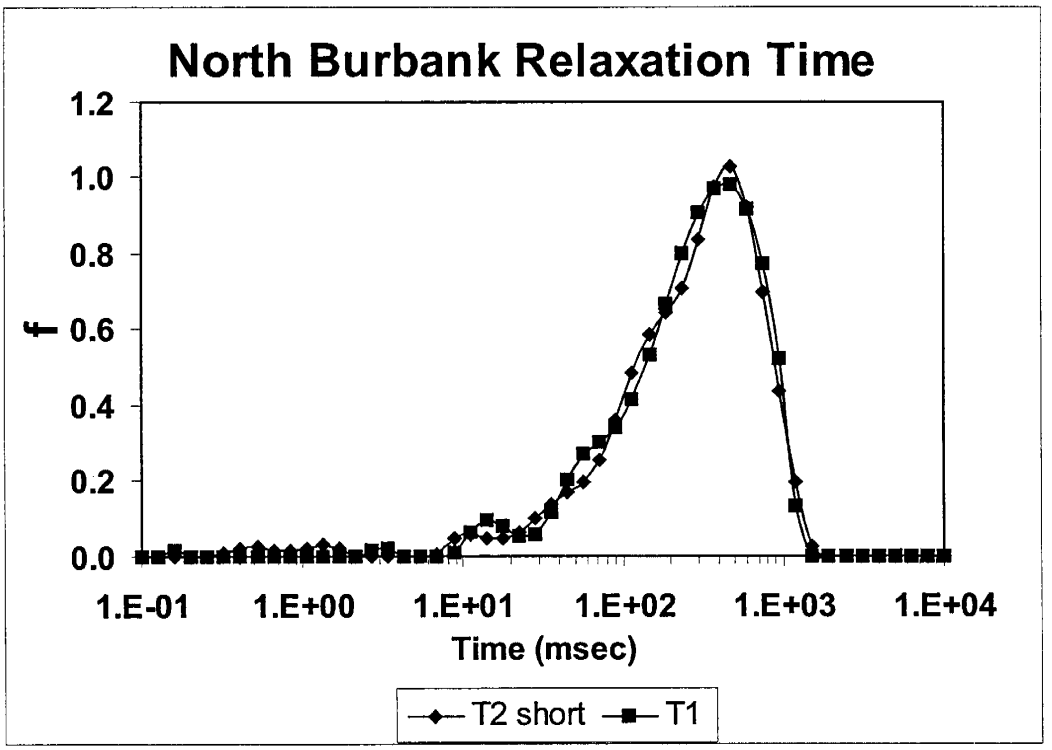
North Burbank Relaxation Time
1.2
1.0
0.8
0.6
0.4
0.2
0.0
f
1.E-01
1.E+00
1.E+01
1.E+02
1.E+03
1.E+04
Time (msec)
T2 short
T1

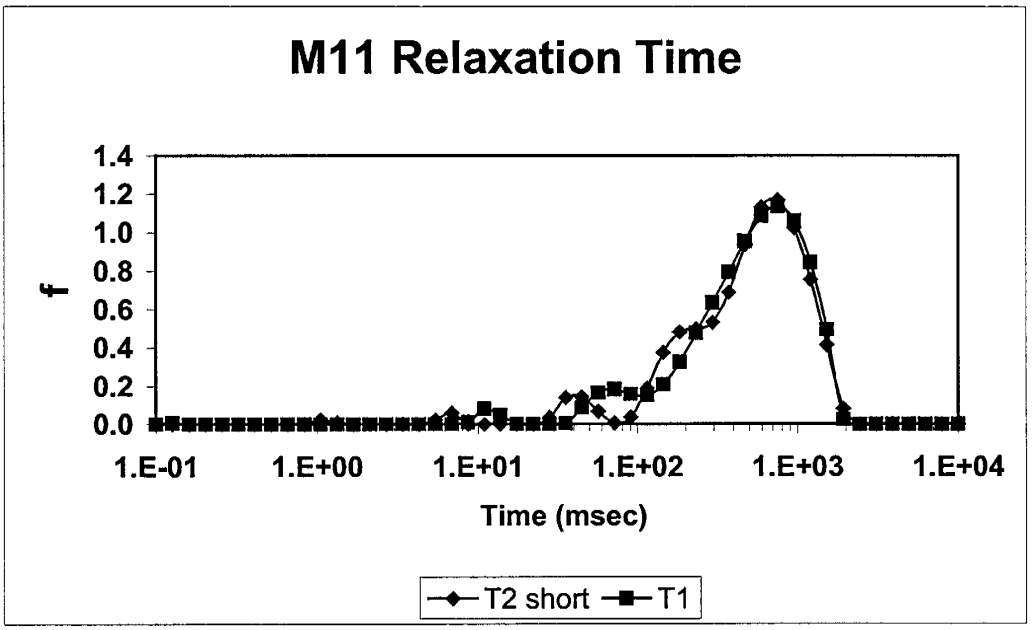
M11 Relaxation Time
f
1.4
1.2
1.0
0.8
0.6
0.4
0.2
0.0
1.E-01
1.E+00
1.E+01
1.E+02
1.E+03
1.E+04
Time (msec)
T2 short
T1

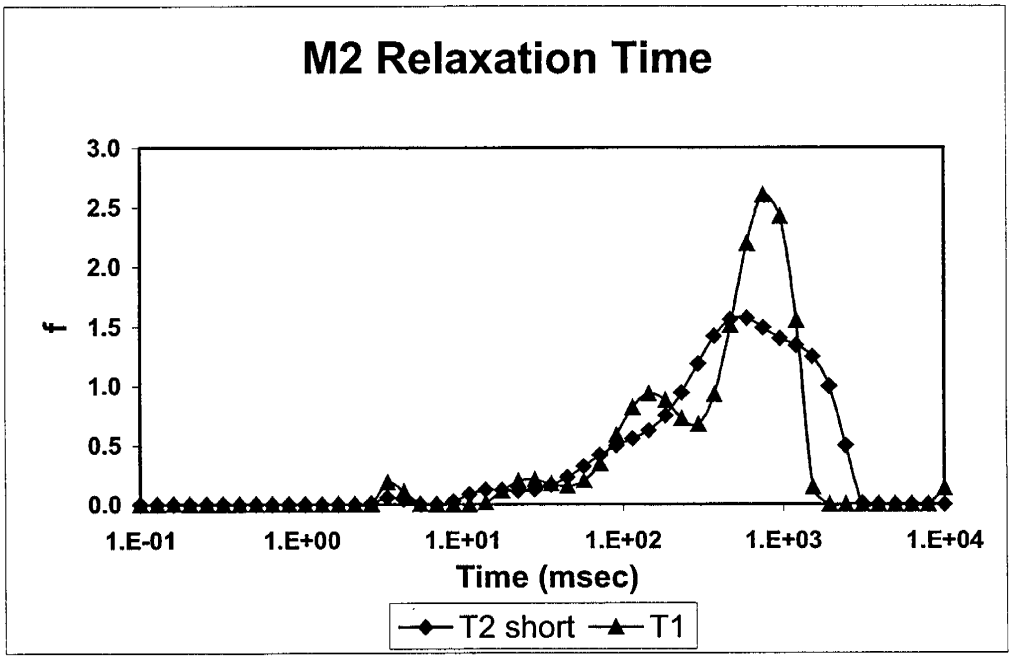
M2 Relaxation Time
f
3.0
2.5
2.0
1.5
1.0
0.5
0.0
1.E-01
1.E+00
1.E+01
1.E+02
1.E+03
1.E+04
Time (msec)
T2 short
T1

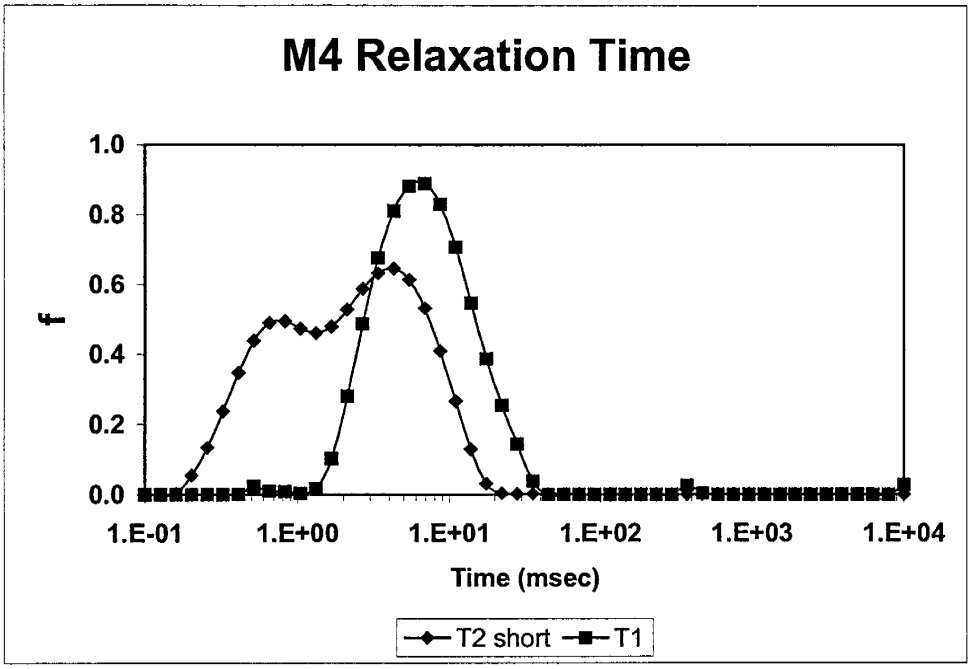
M4 Relaxation Time
1.0
0.8
0.6
0.4
0.2
0.0
f
1.E-01
1.E+00
1.E+01
1.E+02
1.E+03
1.E+04
Time (msec)
T2 short
T1

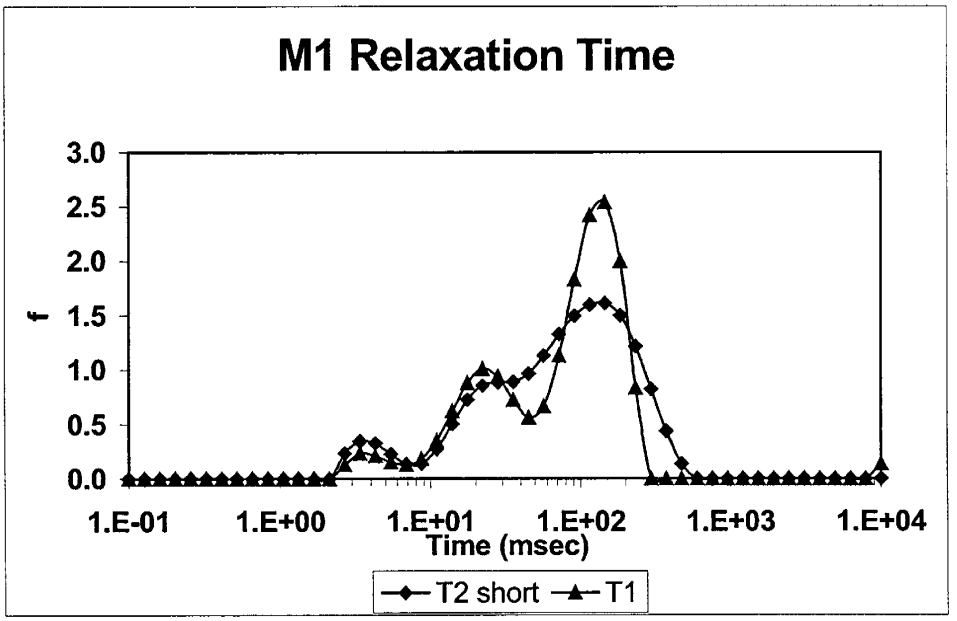
M1 Relaxation Time
3.0
2.5
2.0
1.5
1.0
0.5
0.0
f
1.E-01
1.E+00
1.E+01
1.E+02
1.E+03
1.E+04
Time (msec)
T2 short
T1

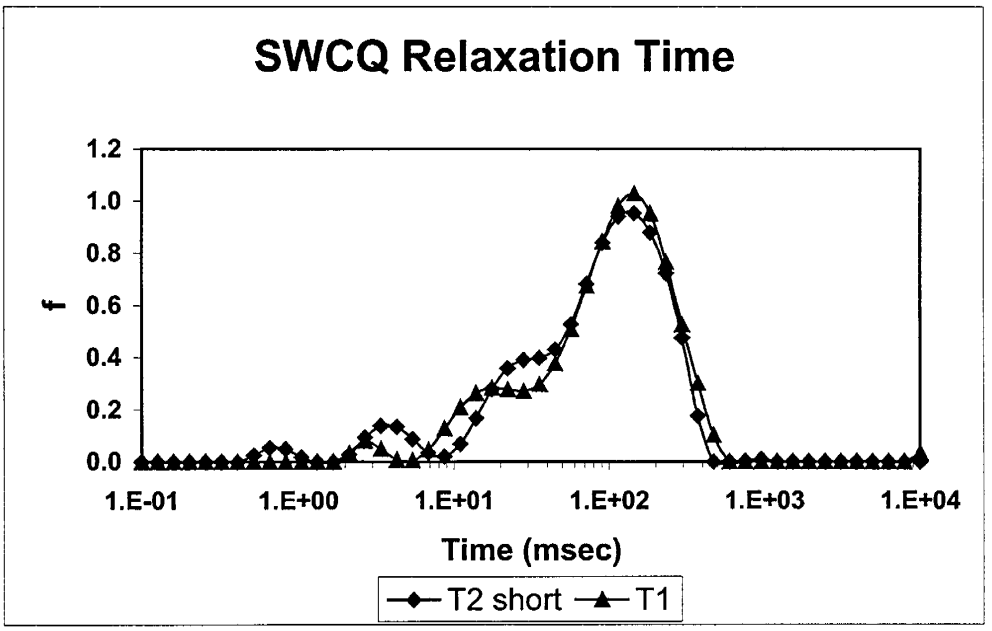
SWCQ Relaxation Time
1.2
1.0
0.8
0.6
0.4
0.2
0.0
f
1.E-01
1.E+00
1.E+01
1.E+02
1.E+03
1.E+04
Time (msec)
T2 short
T1

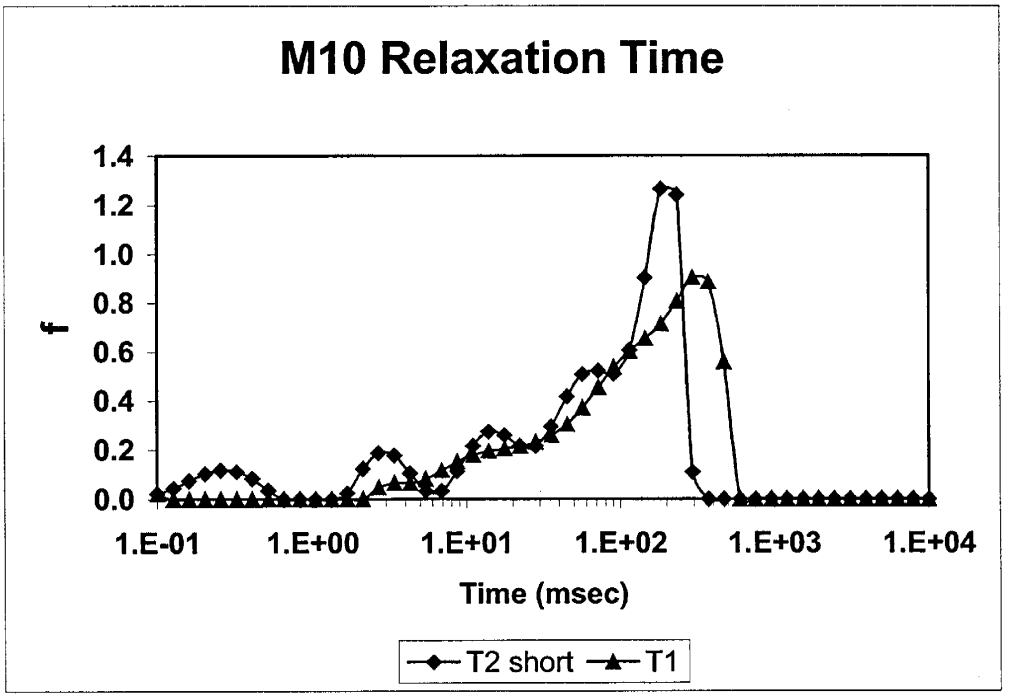
M10 Relaxation Time
1.4
1.2
1.0
0.8
0.6
0.4
0.2
0.0
f
1.E-01
1.E+00
1.E+01
1.E+02
1.E+03
1.E+04
Time (msec)
T2 short
T1

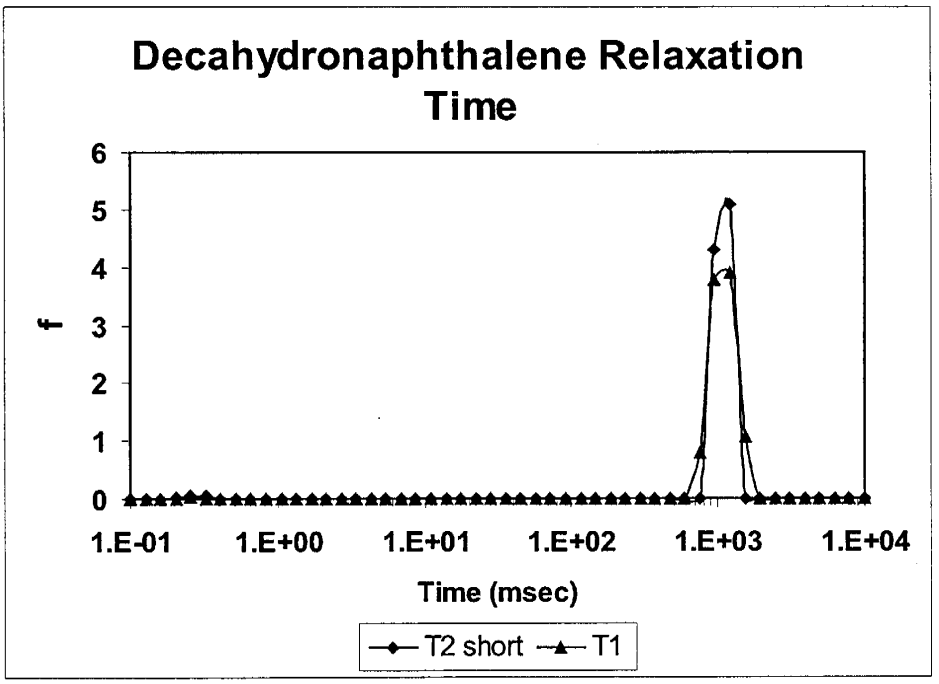
Decahydronaphthalene Relaxation Time
6
5
4
3
2
1
0
f
1.E-01
1.E+00
1.E+01
1.E+02
1.E+03
1.E+04
Time (msec)
T2 short
T1

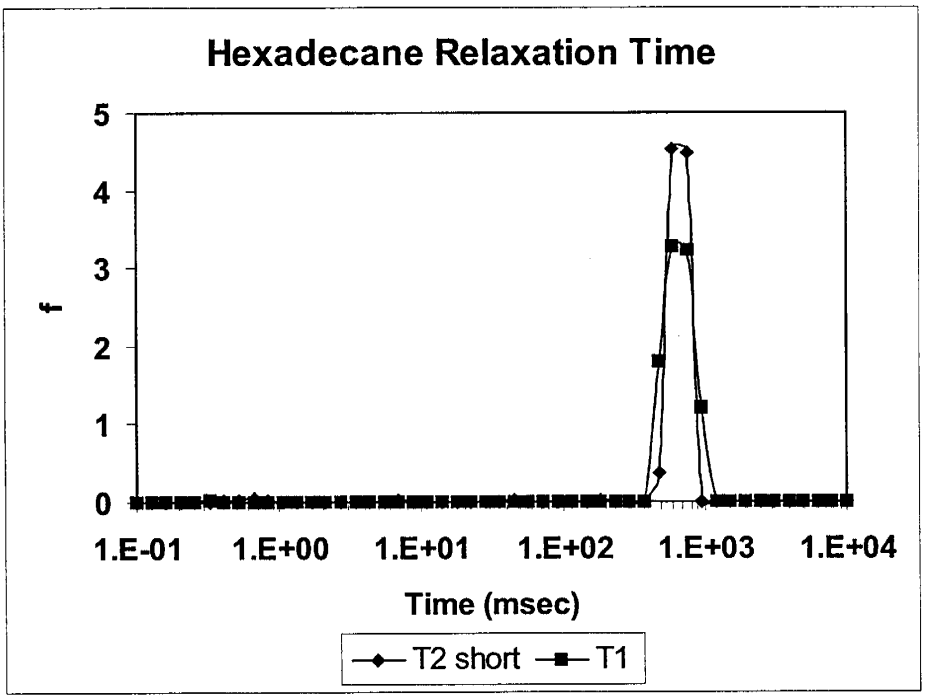
Hexadecane Relaxation Time
5
4
3
2
1
0
f
1.E-01
1.E+00
1.E+01
1.E+02
1.E+03
1.E+04
Time (msec)
T2 short
T1

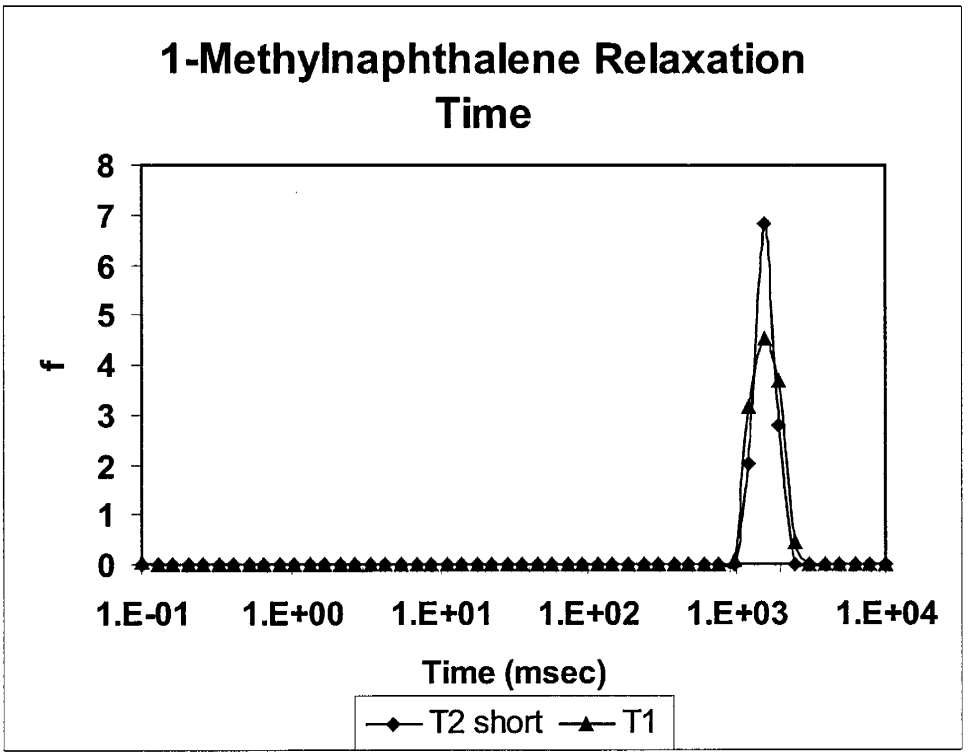
1-Methylnaphthalene Relaxation Time
8
7
6
5
4
3
2
1
0
f
1.E-01
1.E+00
1.E+01
1.E+02
1.E+03
1.E+04
Time (msec)
T2 short
T1

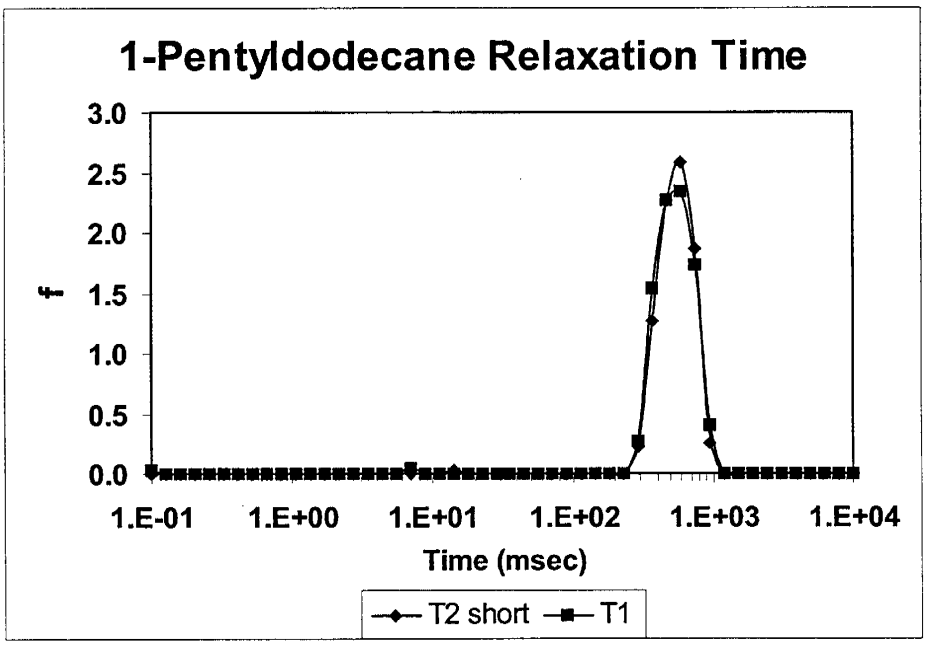
1-Pentyldodecane Relaxation Time
3.0
2.5
2.0
1.5
1.0
0.5
0.0
f
1.E-01
1.E+00
1.E+01
1.E+02
1.E+03
1.E+04
Time (msec)
T2 short
T1

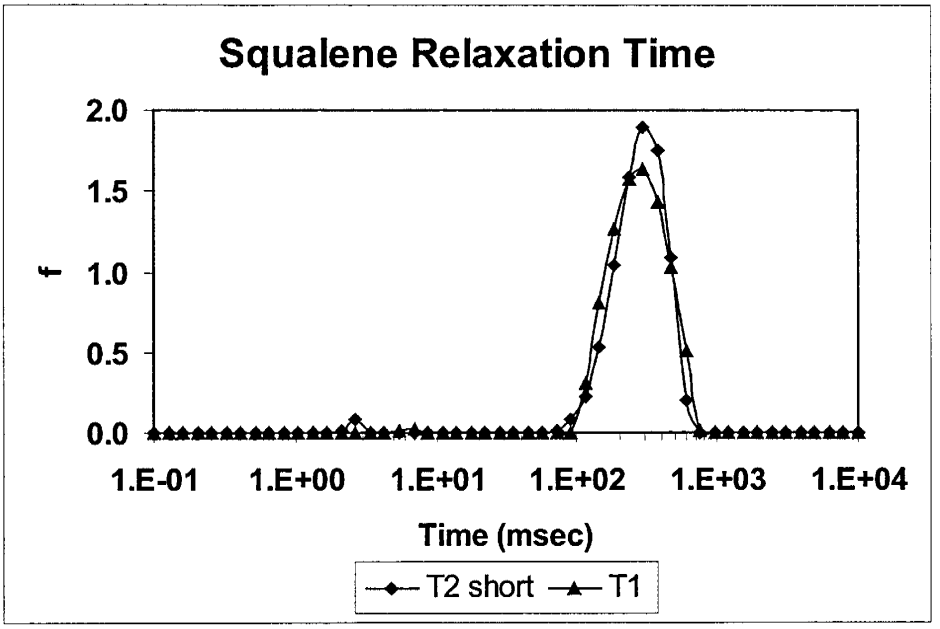
Squalene Relaxation Time
2.0
1.5
1.0
0.5
0.0
f
1.E-01
1.E+00
1.E+01
1.E+02
1.E+03
1.E+04
Time (msec)
T2 short
T1

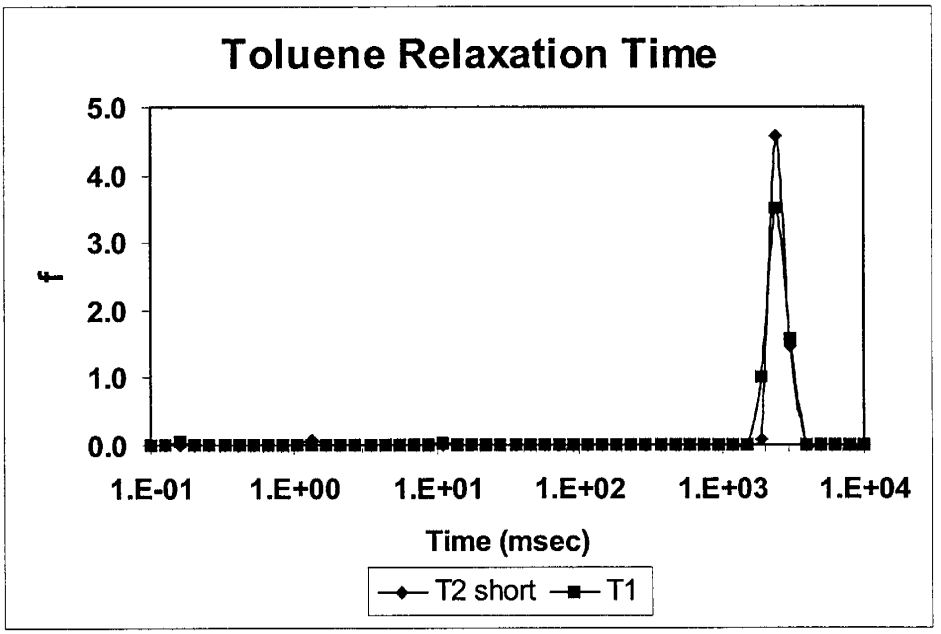
Toluene Relaxation Time
5.0
4.0
3.0
2.0
1.0
0.0
f
1.E-01
1.E+00
1.E+01
1.E+02
1.E+03
1.E+04
Time (msec)
T2 short
T1

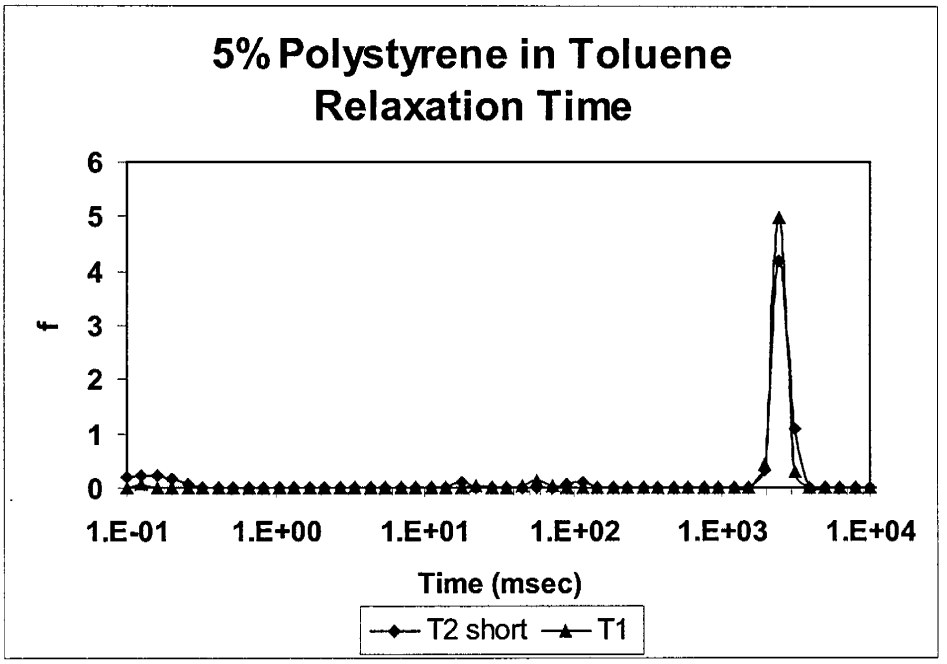
5% Polystyrene in Toluene
Relaxation Time
f
6
5
4
3
2
1
0
1.E-01
1.E+00
1.E+01
1.E+02
1.E+03
1.E+04
Time (msec)
T2 short
T1

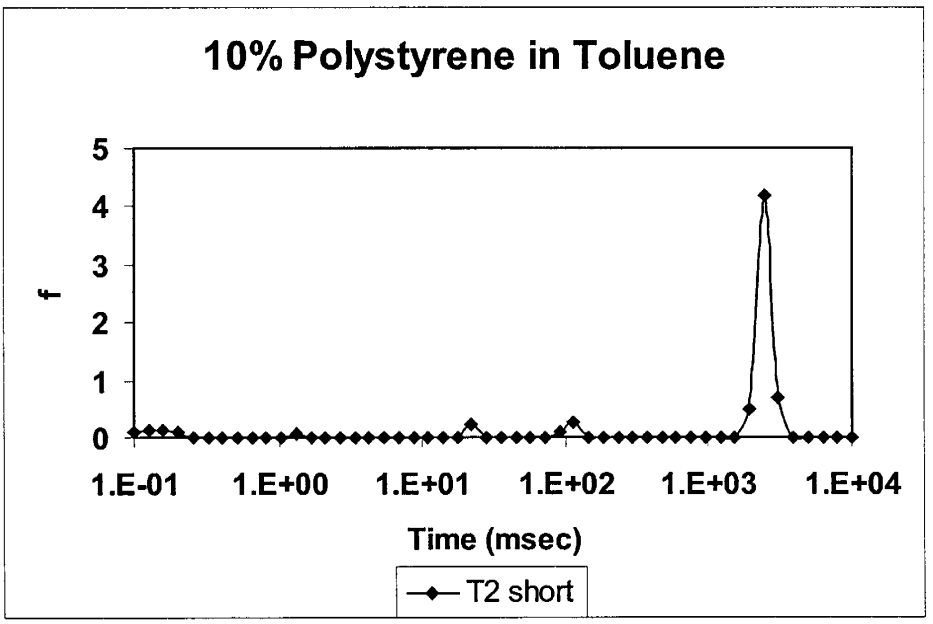
10% Polystyrene in Toluene
f
5
4
3
2
1
0
1.E-01
1.E+00
1.E+01
1.E+02
1.E+03
1.E+04
Time (msec)
T2 short

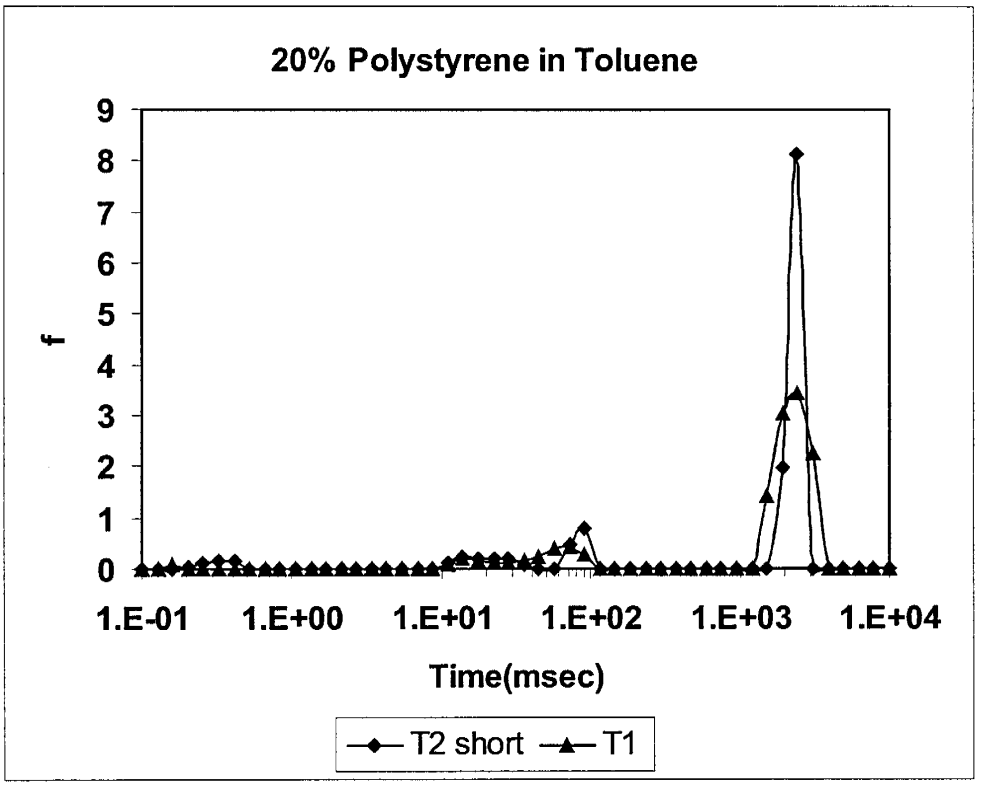
20% Polystyrene in Toluene
f
9
8
7
6
5
4
3
2
1
0
1.E-01
1.E+00
1.E+01
1.E+02
1.E+03
1.E+04
Time(msec)
T2 short
T1

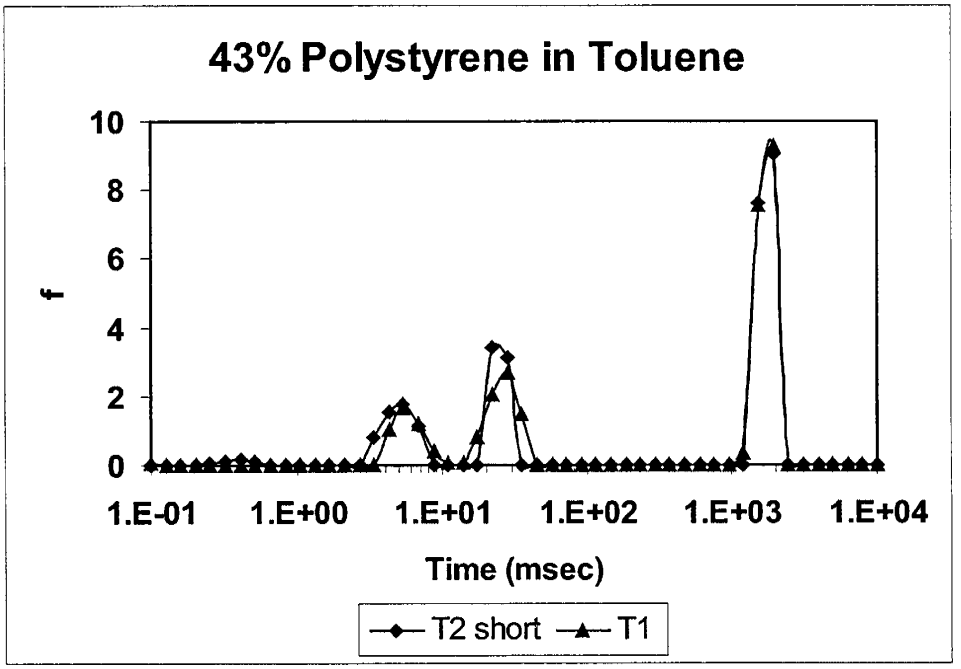
43% Polystyrene in Toluene
f
10
8
6
4
2
0
1.E-01
1.E+00
1.E+01
1.E+02
1.E+03
1.E+04
Time (msec)
T2 short
T1

Task 2.0 Fluid-Rock Interactions: Fluid-rock interactions having a significant effect on the estimation of capillary bound water and permeability are; Sub-Task 2.1 Wettability Alteration; Sub-Task 2.2 Diffusion in Internal Gradients; Sub-Task 2.3 Surface Relaxivity, and Sub-Task 2.4 Restricted Diffusion. A default assumption in the interpretation of NMR well logs is that there is a one-to-one relationship between T_2 relaxation time distribution of the water in the pores spaces of the rock and the surface/volume ratio of the pore in which the water exists. This implies that there is one value of surface relaxivity for sandstones and another for carbonates. This default assumption may be violated if there is wettability alteration, diffusion in internal field gradients, or an abnormal surface relaxivity. Restricted diffusion measurements offer a possibility of measuring pore size and tortuosity if relaxation processes do not excessively attenuate the signal.

Sub-Task 2.1 Wettability Alteration:

[1]Interpretation of Wettability in Sandstones With NMR Analysis

Gigi Qian Zhang, Chien-Chung Huang and George J. Hirasaki
Rice University, Houston, Texas

Abstract: Using nuclear magnetic resonance (NMR) analysis, a systematic interpretation of wettability alteration was carried out using three types of sandstones with varying clay content. Two fluid systems were investigated. Soltrol 130 was used as the refined oil. A deep-water Gulf of Mexico crude oil was used as the crude oil that is known to alter the wettability in restored-state core analysis.

Fluids that are in molecular contact with mineral surfaces have a relaxation time that is less than the bulk fluid relaxation time due to surface relaxation phenomena. Mixed wettability can result in lengthened NMR relaxation of brine compared to 100% brine saturation and shortened NMR relaxation of oil compared to bulk oil when oil comes in contact with part of the rock surfaces. Thus, NMR proton spin-lattice relaxation time (T_1) distribution provides a qualitative description of wettability alteration.

Bentheim and Berea were water-wet with refined oil. When saturated with crude oil and brine at S_{wir} they became mixed-wet after aging. After forced imbibition, residual oil had a shorter relaxation time compared to the bulk oil, indicating that patches of crude oil remained on the rock surfaces.

North Burbank sandstone was mixed-wet when either saturated with refined oil at S_{wir} or crude oil after aging. Micropores formed by chlorite flakes were filled with brine. Oil in the macropores was in contact with the tips of chlorite flakes. After forced imbibition, brine in the macropores was partially shielded from the pore walls by a film of oil spanning the tips of chlorite clays. The evidence for this was that brine in the macropores relaxed slower than 100% brine saturation but faster than bulk brine and oil relaxed faster than bulk oil. Thus North Burbank appeared mixed-wet with either refined oil or crude oil. However, the extent of wetting change was greater with crude oil. This

[1] Originally presented at 1999 International Symposium of the Society of Core Analysts, August 1-4, 1999, Golden, Colorado, USA, Paper 9921

special wetting behavior of North Burbank came from its microporous structure formed by pore-lining chlorite flakes.

INTRODUCTION

Wettability is defined as "the tendency of one fluid to spread on or adhere to a solid surface in the presence of other immiscible fluids" (Craig, 1971). It has effects on capillary pressure, relative permeability, and residual oil saturation. Knowledge of reservoir wettability is essential to efficient oil recovery processes. Anderson (1986, 1987) gave a comprehensive literature survey on wettability. Salathiel (1973) introduced the concept of "mixed wettability" in which the oil-wet surfaces form continuous paths for oil through the larger pores and the smaller pores remain water-wet. Morrow (1990) discussed measurements of wettability and the dramatic effects that wettability can have on oil recovery. Kovscek et al. (1993) developed a pore-level picture of how mixed wettability might form and evolve in reservoir rock initially filled with brine. Our definition of mixed wettability is that the smallest pores contain only brine, thus are water-wet, while the larger oil-filled pores have oil wetting the pore walls.

NMR measurements are sensitive to wettability because of the strong effect that the solid surface has on promoting magnetic decay (relaxation) of the contacting fluid. Historically, investigators have applied NMR techniques to study wettability on various unconsolidated materials. Brown and Fatt (1956) started the pioneering work by measuring T_1 relaxation times of water in uncoated sand packs as water-wet porous media, and Dri-film treated sand packs as oil-wet porous media. Saraf et al. (1970) measured T_1 relaxation times of water-wet glass bead and oil-wet polymer bead systems. Williams and Fung (1982) worked on commercial uncoated glass beads as the water-wet system and coated glass beads as the oil-wet system. Hsu et al. (1992) investigated wettability on glass beads. Doughty et al. (1993) investigated systems of glass or Teflon capillary tubings by NMR microscopy and spin-lattice relaxation.

A lot of research has also been done on consolidated materials. Borgia et al. (1991) studied the relaxation behavior of water-oil in well-characterized microporous porcelain structures. Straley et al. (1991) observed water-wet condition with sandstones partially saturated with kerosene. Hsu et al. (1992) investigated wettability on carbonate cores. Doughty et al. (1993) studied wettability on Fontainebleau sandstones. Howard and Spinler (1993) observed water-wet condition for chalk cores partially saturated with decane. Øren et al. (1994) conducted two-phase oil-water NMR measurements on sandstones with different wettabilities. Bobroff et al. (1994) investigated wettability in natural sandstone rocks saturated with deuterium oxide and dodecane. Rueslåtten et al. (1994) observed mixed wettability on North Sea sandstone reservoirs. Marschall et al. (1997) investigated the effects of invert oil muds on the wetting preference of rock surfaces in the North Sea area. Morriss et al. (1997) found that Belridge diatomite was water-wet when partially saturated with Soltrol and brine at S_{wir} and predominantly water-wet at native state. Spinler (1997) used NMR for a qualitative estimate of wettability for a carbonate field.

In this paper, we provide a systematic study of wettability on sandstones with refined oil/brine and crude oil/brine with the following procedures: 100% brine saturation, centrifuged in oil to irreducible brine saturation, aged in the case of crude oil, spontaneous imbibition of brine, forced imbibition of brine and finally D_2O brine

diffusion. Wettability will be interpreted from NMR T_1 relaxation times and compared with two quantitative methods, which are the spontaneous imbibition and forced imbibition wettability test proposed by Amott and residual oil saturation measurement.

EXPERIMENTAL METHOD

Suite of Test Sandstones

A suite of sandstones was selected to evaluate the effect of wettability on the NMR response of sandstones. The sandstones were selected based on different degree of shalyness. Their properties are listed in Table 1.

Table 1 Properties of sandstones

Rock Name	Bentheim	Berea	North Burbank
Porosity	22.9±0.4	18.9±0.8	23.1±1.0
Permeability (mD)	3003±20	205±20	237±64
Clays	<1 wt%	3 wt%	chlorite coated

Bentheim sandstone is nearly clay free. Berea sandstone is moderately shaly. Figure 1 provides a view of clays in Berea sandstone at 2000 magnification. The clays are primarily book-like kaolinite and needle-like illite. Berea also contains siderite as localized clusters of crystals. North Burbank sandstone was selected because Trantham and Clampitt (1977) reported that this reservoir was oil-wet due to the iron-rich, chamosite chlorite coating to the sand grains. Figure 2 is a photomicrograph of a North Burbank sand grain showing chlorite coating at 10,000 magnification. Chlorite flakes can be viewed as forming microchannels perpendicular to pore walls such that each micropore opens to a macropore (Straley et al., 1995).

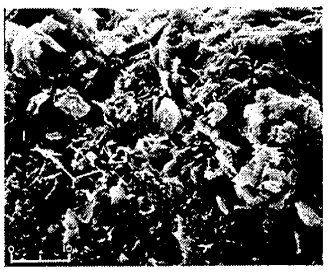

Fig. 1. View of clays in Berea sandstone (Shell Rock Catalog).

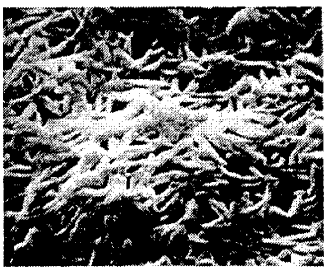

Fig. 2. Photomicrograph of North Burbank sand grain showing chlorite coating (adapted from Trantham and Clampitt, 1977).

Berea and North Burbank sandstones have similar porosity and permeability but are very different because of the type of clays. North Burbank sandstone has a significant diffusion effect due to internal field gradient that complicates the interpretation on NMR proton spin-spin relaxation time (T_2) measurements (Zhang et al., 1998). Thus only the T_1 response will be discussed to illustrate the effect of wettability.

Test Hydrocarbons

The effect of wettability on the NMR response was investigated with both refined oil and crude oil. Soltrol 130 is a refined aliphatic oil with a narrow range of molecular weights. A 30°API crude oil from a deep-water Gulf of Mexico turbidite formation was used as a crude oil that is known to alter the wettability in restored-state core analysis (Hirasaki, 1996). This crude oil has the code name SMY. The T_1 relaxation time distributions of these two oils are shown in Fig. 3. Soltrol has a narrow, log normal

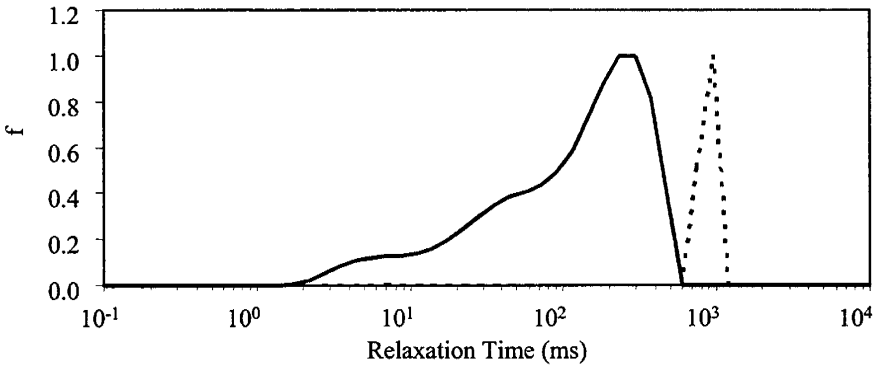

Fig. 3. Normalized T_1 distributions of Soltrol (dotted curve) and SMY crude oil (solid curve).

distribution. SMY crude oil has a broad distribution with a tail that extends to relaxation times in the region of BVI (below 50 ms $T_{1cutoff}$). The short relaxation times may be due to an asphaltene content of 3 wt% and 18-24 ppm paramagnetic nickel and 45-48 ppm vanadium concentrations.

NMR Measurements and Inversion Method

All NMR T_1 measurements reported here were made with a Maran-2 spectrometer. The T_1 measurements were made with the inversion recovery method with 50 measurements between 0.01 ms and 10,000 ms. The wait time between repetitions equaled to 4-6 times the longest relaxation time. A non-negative non-linear least-square inversion method was used to estimate T_1 relaxation time distributions. A regularization technique, norm smoothing, was used. A method of relating the optimum regularization parameter (α) to the optimum slope of the log-log plot of the standard error versus α, as recommended by Dunn et al. (1994) and Fordham et al. (1995), was adopted.

Cleaning Procedures

The sandstone samples were cleaned by flow-through of solvents. The following sequence was conducted: (1) flow ~20 pore volume (PV) chloroform/methanol azeotrope, ~10 PV tetrahydrofuran, and ~10 PV chloroform/methanol azeotrope in sequence, (2) shut in for overnight soak, (3) flow ~10 PV chloroform/methanol azeotrope, ~10 PV tetrahydrofuran, ~10 PV chloroform/methanol azeotrope, ~10 PV tetrahydrofuran, and ~10 PV chloroform/methanol azeotrope in sequence, (4) shut in for overnight soak, (5) flow ~10 PV column-treated tetrahydrofuran, ~10 PV column-treated chloroform/methanol azeotrope, and ~10 PV column-treated methanol in sequence, (6) blow methanol from core using nitrogen, (7) dry in vacuum oven overnight at 60°C.

WETTABILITY BEHAVIOR OF REFINED OIL SYSTEM

The cleaned sandstone samples were vacuum saturated with 5% NaCl brine to 100% brine saturation, then centrifuged in Soltrol to a capillary pressure of 70 psi. The experiments and NMR measurements were performed in triplicate for each type of sandstone, as reported in Table 2. Because of similarities among three samples, the relaxation time distribution of only one sample is illustrated. The T_1 relaxation time distributions of Soltrol with brine at S_{wir} are compared with those of 100% brine saturation for Bentheim, Berea, and North Burbank in Fig. 4. T_1 distribution of bulk Soltrol is also shown as the dashed curve.

When the bulk relaxation rate of brine is ignored, brine in 100% S_w rock samples will relax only by the surface-relaxation mechanism. Thus, the T_1 relaxation time distribution is akin to a pore-size distribution. The T_1 distribution of North Burbank is bimodal because of a significant amount of microporosity due to chlorite coating.

After centrifugation in Soltrol to 70 psi, Bentheim and Berea have the classic T_1 distributions where the irreducible water response appears at the region corresponding to small pores interpreted from 100% S_w condition. The peak at long relaxation times is the Soltrol response. Since the Soltrol peak centers on the T_1 distribution of bulk Soltrol, Bentheim and Berea were water-wet with Soltrol relaxing as bulk fluid.

In the North Burbank sample, irreducible brine response has a higher peak than the brine response in the micropores at 100% S_w condition. This is because after drainage with Soltrol, irreducible brine was isolated in each micropore, which no longer had diffusional coupling with macropore brine as in the 100% S_w condition (Straley et al., 1995; Ramakrishnan et al., 1998). Most importantly, the Soltrol peak has shorter relaxation times than bulk Soltrol. Soltrol apparently had surface relaxation as a result of contacting the tips of the chlorite flakes. Therefore, North Burbank was mixed-wet with refined oil. Figure 5 illustrates our interpretation of fluid distribution in these sandstones after saturation with Soltrol and brine at S_{wir}.

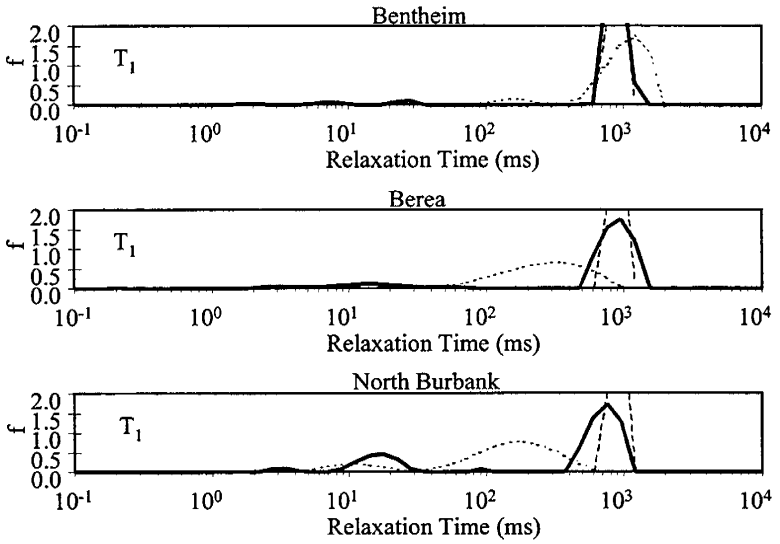

Fig. 4. T_1 relaxation time distributions of the sandstones at 100% brine saturation (dotted curve) and Soltrol saturated to S_{wir} (solid curve). The T_1 relaxation time distribution of bulk Soltrol is shown as the dashed curve..

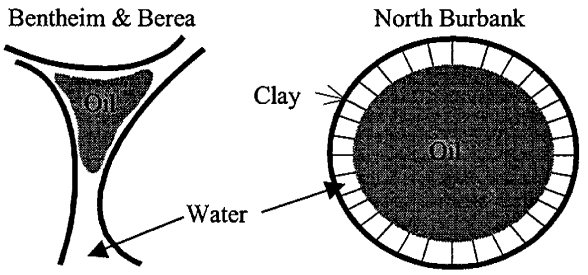

Fig. 5. Fluid distribution of refined oil systems with Soltrol and brine at S_{wir}.

The sandstone samples were then immersed into 5% NaCl brine solution. Only Bentheim and Berea had spontaneous imbibition of brine. Soltrol saturation decreased and brine filled some larger pores. Afterwards, they were centrifuged in brine for forced imbibition to a capillary pressure of –25 psi. Bentheim exhibited a greater increase of brine saturation than Berea after forced imbibition. Their T_1 distributions are shown in Fig. 6.

To separate the residual Soltrol response from the brine response after forced imbibition, the rock samples were soaked twice in D_2O brine solution. Water was replaced by D_2O, so that only residual oil gives a NMR signal (Morriss et al., 1997). Figure 6 compares T_1 distributions after forced imbibition with those after D_2O brine diffusion. The difference in relaxation time distributions is the brine response. For Berea, the peak at long relaxation times after forced imbibition is solely residual oil response. However, for Bentheim and North Burbank, this peak also includes some brine response.

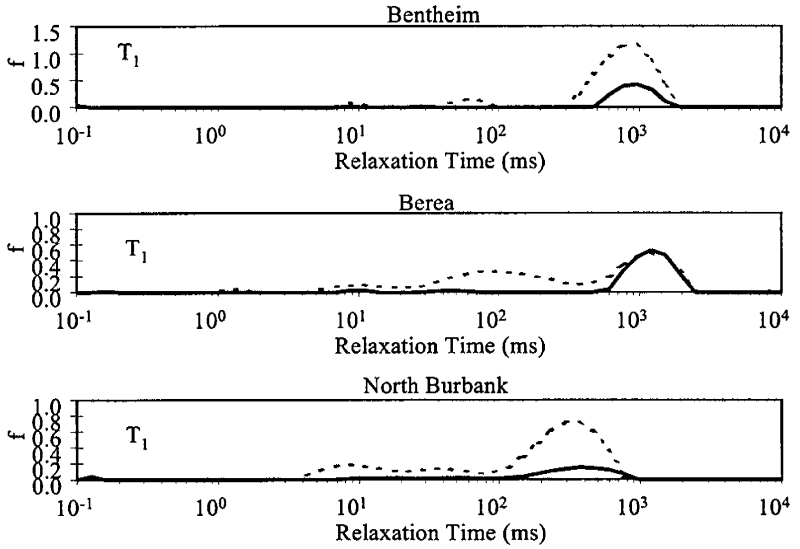

Fig. 6. T_1 relaxation time distributions of the sandstones after forced imbibition (dotted curve) and after D_2O brine diffusion (solid curve).

Wettability behavior for these sandstones after forced imbibition can be determined by comparing distributions after forced imbibition with 100% brine saturation, shown in Fig. 7, and comparing distributions after D_2O brine diffusion with bulk Soltrol, shown in Fig. 8.

In Bentheim, after forced imbibition, brine relaxed similarly to completely water-wet condition with the residual Soltrol response centering on the T_1 distribution of bulk Soltrol. Therefore, Bentheim was water-wet with Soltrol relaxing as bulk fluid.

In Berea, after forced imbibition, although the peak at long relaxation times appears to the right of the distribution of 100% brine saturation, it should not be interpreted as brine relaxing slower than completely water-wet condition due to wettability alteration. This is because from Fig. 6 this peak is mostly residual Soltrol response. As shown in Fig. 8, the residual Soltrol does not have shorter relaxation time than bulk Soltrol. (The unexplained T_1 being longer than that of the bulk Soltrol was observed in two out of the three Berea samples.) Therefore, Berea was water-wet too.

In North Burbank, after forced imbibition, the distribution at long relaxation times is to the right of the distribution at 100% brine saturation. It could be due to the brine in macropores relaxing slower than completely water-wet condition, and/or because the peak at long relaxation times contains some residual Soltrol response as shown in Fig. 6. However, from Fig. 8, the distribution of residual Soltrol apparently shifted from T_1 distribution of bulk Soltrol, meaning that Soltrol had surface relaxation due to the contact with the tips of chlorite flakes. Hence, North Burbank was mixed-wet, with brine in the macropores partially shielded from the pore walls by a film of Soltrol spanning the tips of chlorite flakes, as shown in Fig. 9 (Ben Swanson, private communication).

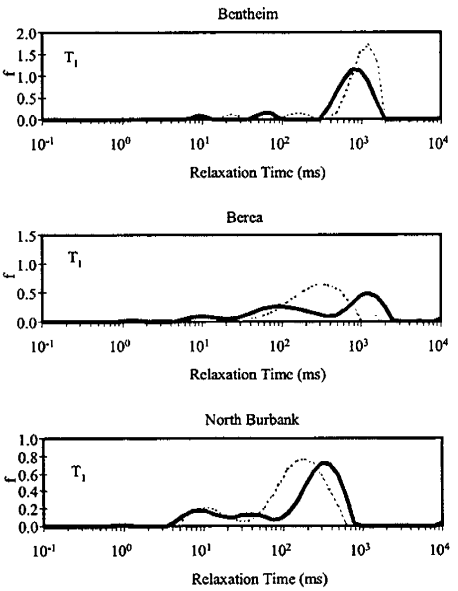

Fig. 7. T_1 relaxation time distributions of the sandstones after forced imbibition (solid curve) compared to 100% brine saturation (dotted curve).

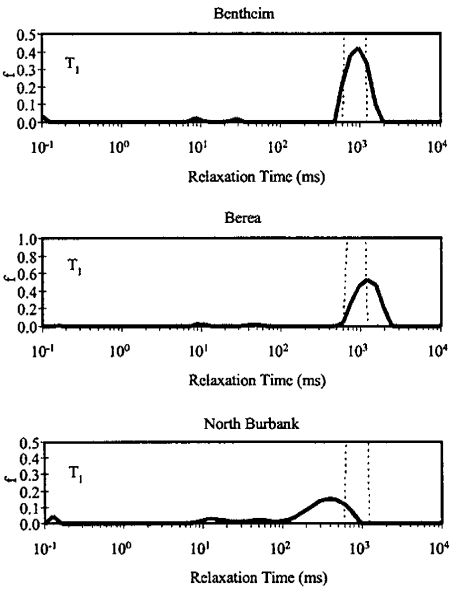

Fig. 8. T_1 relaxation time distributions of the sandstones after D_2O brine diffusion (solid curve) compared to bulk Soltrol (dotted curve).

The distributions of Soltrol and brine after forced imbibition for Bentheim, Berea and North Burbank are illustrated in Fig. 9. Due to the pore-lining chlorite, North Burbank was mixed-wet even with refined oil.

WETTABILITY BEHAVIOR OF CRUDE OIL SYSTEM

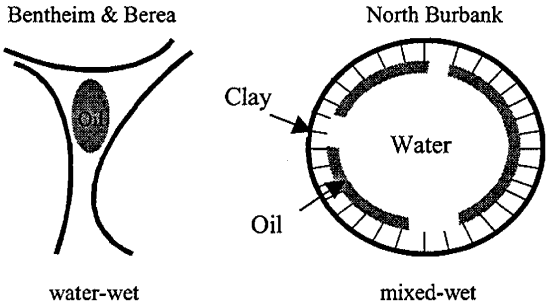

Fig. 9. Fluid distribution of refined oil systems after forced imbibition of brine.

The sandstone samples were cleaned and restored to 100% brine saturation. Then, they were centrifuged in SMY crude oil to a capillary pressure of 70 psi. NMR T_1 measurements were made and then the samples were immersed in a sealed bottle of SMY crude oil, aged for 3 weeks at a temperature of 50°C. Figure 10 compares the T_1 distributions before aging and after aging. The T_1 distribution of bulk SMY crude oil is scaled to oil saturation. For all three sandstones, before aging, T_1 distributions start from the same position as those of bulk SMY crude oil. (This behavior was observed with refined oil in all three rocks.) Since the crude oil relaxed at the bulk rate, this suggests that all three sandstones were water-wet before aging. After aging, all distributions shift to shorter relaxation times. Bentheim had the greatest surface relaxation of SMY crude oil, Berea in the middle, and North Burbank exhibited the smallest surface relaxation effect. In North Burbank, the peak interpreted as the brine response in micropores does not change position and amplitude after aging. Therefore, brine filled the micropores at all times; SMY crude oil did not invade into the micropores during aging. In conclusion, all sandstones changed from water-wet to mixed-wet after aging (Rueslåtten et al., 1994). The distribution of crude oil and brine after aging is illustrated in Fig. 11. Crude oil was either in contact with rock surfaces in Bentheim and Berea or in contact with the tips of chlorite flakes in North Burbank.

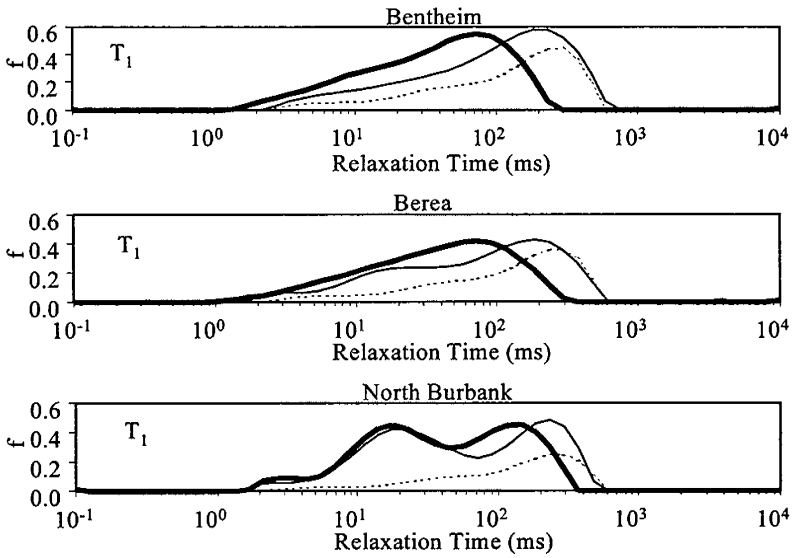

Fig. 10. T_1 relaxation time distributions of the sandstones with SMY crude oil saturated to S_{wir} before aging (solid curve) and after aging (bold solid curve). The T_1 relaxation time distribution of bulk SMY crude oil, scaled to oil saturation, is shown as the dotted curve.

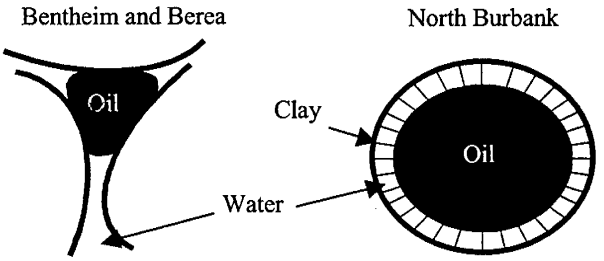

Fig. 11. Fluid distribution of crude oil systems after aging.

In order to prove that the wettability change after aging interpreted from NMR T_1 distributions was not due to change of the T_1 distribution of the bulk crude oil, the T_1 distributions of bulk SMY crude oil before aging and after aging under the same aging condition are compared in Fig. 12. There is negligible difference between the T_1 distributions before and after aging. Therefore, aging did not result in any bulk T_1 change of SMY crude oil.

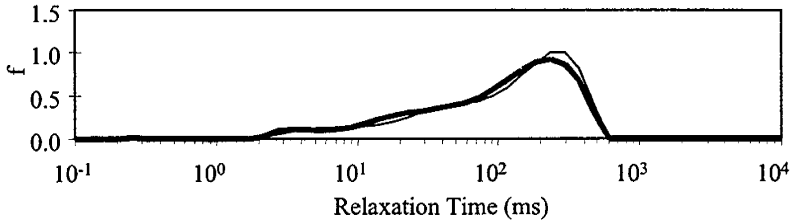

Fig. 12. T_1 relaxation time distributions of bulk SMY crude oil before aging (solid curve) and after aging (bold solid curve).

Following the same experimental procedures as with the refined oil systems, the sandstone samples were then soaked in 5% NaCl brine solution for spontaneous imbibition. Only Berea had small amount of spontaneous imbibition. Figure 13 compares T_1 distributions after forced imbibition of brine with those after D_2O brine diffusion. The difference between the two curves is the brine response.

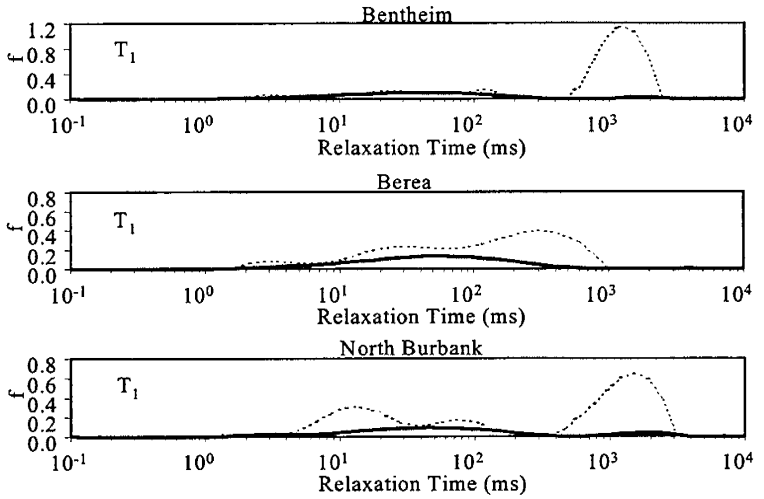

Fig. 13. T_1 relaxation time distributions of the sandstones after forced imbibition (dotted curve) and after D_2O brine diffusion (solid curve).

Figure 14 compares T_1 relaxation time distributions after forced imbibition of brine with 100% brine saturation. For Bentheim and Berea, the water response after forced imbibition appears at a similar range of relaxation times as 100% brine saturation. However, for North Burbank, the macropore brine relaxes slower than 100% brine saturation and faster than bulk brine. We interpret this as brine in macropores being partially shielded from pore walls by a film of SMY crude oil.

Residual oil response after D_2O brine diffusion is compared with T_1 distribution of bulk oil in Fig. 15. For all three sandstones, residual oil has surface relaxation due to wettability alteration. The small peaks between 1000 to 6000 ms are due to incomplete exchange of water by D_2O.

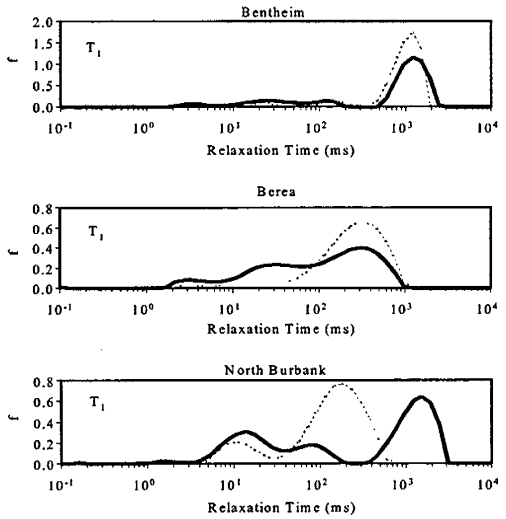

Fig. 14. T_1 relaxation time distributions of the sandstones after forced imbibition (solid curve) compared to 100% brine saturation (dotted curve).

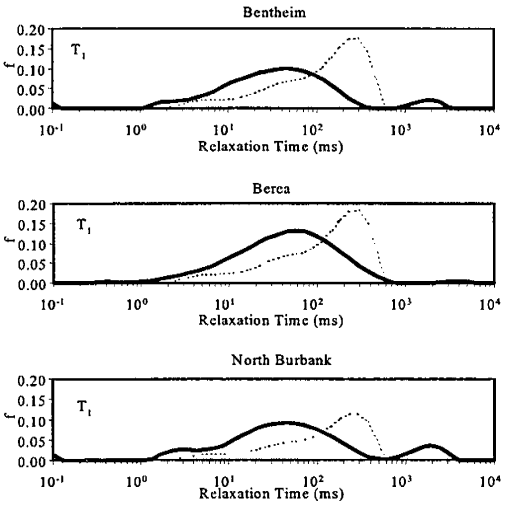

Fig. 15. T_1 relaxation time distributions of the sandstones after D_2O brine diffusion (solid curve) compared to bulk SMY crude oil (dotted curve), scaled to oil saturation.

Therefore, after forced imbibition of brine, all three sandstones were shown to be mixed-wet (Salathiel, 1973; Kovscek et al., 1993). These results are consistent with patches of crude oil in contact with sand grains in Bentheim and Berea, and residual SMY crude oil spanning part of the tips of chlorite clays in North Burbank, as shown in Fig. 16.

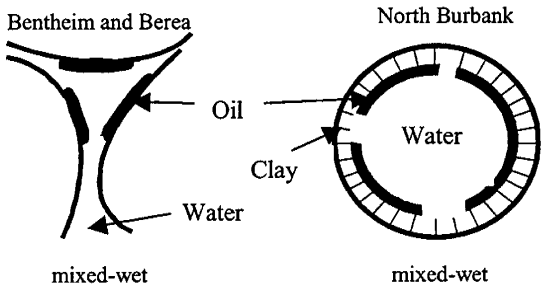

Fig. 16. Fluid distribution of crude oil systems after forced imbibition of brine.

AMOTT WATER WETTABILITY INDEX

Amott water wettability index (Amott, 1959) was determined by dividing the amount of oil displaced by brine by spontaneous imbibition with the amount of oil displaced by brine by both spontaneous and forced imbibition. Water-wet systems have Amott water wettability index about 1. Both intermediate-wet and oil-wet systems have Amott index value around 0.

Table 2 lists the Amott index values for Bentheim, Berea and North Burbank for refined oil and crude oil systems.

Table 2 Irreducible brine saturation, brine saturation after spontaneous imbibition and after forced imbibition determined by weighting for Bentheim, Berea and North Burbank. Amott water wettability index values were determined from these values.

	Soltrol/Brine					SMY Crude Oil/Brine				
	S_{wir}[b]	S_w after sp.	S_w after for.	Amott	Avg.	S_{wir}[b]	S_w after sp.	S_w after for.	Amott	Avg.
Bentheim-1	8.3	58.4	73.0	0.77	0.77	27.7	28.4	75.9	0.01	-0.04
Bentheim-2	2.0	51.8	67.1	0.77	±0.01	16.9[a]	15.8[a]	68.4	-0.02	±0.06
Bentheim-3	5.5	55.3	69.5	0.78		17.8[a]	13.1[a]	67.6	-0.10	
Berea-1	17.9	55.5	56.5	0.97	1.05	41.9	53.8	72.7	0.38	0.38
Berea-2	17.8	52.0[a]	48.2[a]	1.13	±0.08	34.4	44.6	60.7	0.39	±0.02
Berea-3	19.2	50.7[a]	49.1[a]	1.06		38.3	47.1	62.8	0.36	
N.B.-1	41.4	42.6	85.3	0.03	0.04	51.2[a]	50.5[a]	88.5	-0.02	-0.01
N.B.-2	45.7	47.2	86.5	0.04	±0.01	56.8[a]	55.4[a]	95.5	-0.03	±0.03
N.B.-3	40.8	43.7	92.5	0.05		52.0	52.7	91.4	0.02	

(a:) Because of experimental uncertainty, some of the brine saturation changed in the wrong direction.

(b:) The S_{wir} for the SMY crude oil is systematically larger than S_{wir} for the Soltrol. This was also observed with another system (Hirasaki, 1990).)

For refined oil systems, Bentheim and Berea had spontaneous imbibition and they were water-wet. North Burbank was not water-wet. For crude oil systems, after aging, only Berea displayed minor spontaneous imbibition and all three sandstones were not water-wet. Amott analysis is consistent with the wettability alteration inferred from NMR measurements.

RESIDUAL OIL SATURATION

Residual oil saturation provides another quantitative indication of wettability alteration. Residual oil saturation for refined oil and crude oil systems are determined by averaging S_{or} from weighting and NMR measurements after forced imbibition and after D_2O brine diffusion. Toluene-air counter current imbibition (CCI) was used to estimate the residual oil saturation under strong water-wet conditions. Figure 17 compares residual oil saturation for Bentheim, Berea, and North Burbank. The white bars are CCI residual, hashed bars are S_{or} for Soltrol, and shaded bars are for SMY crude oil. 'w' denotes water-wet condition and 'm' denotes mixed-wet condition.

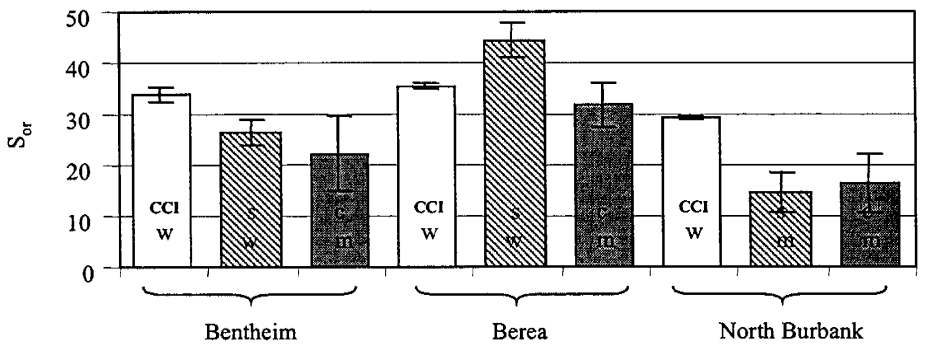

Fig. 17. Residual oil saturation from CCI (white bars), refined oil systems (hashed bars), and crude oil systems (shaded bars).

For Bentheim and Berea, Soltrol has higher residual oil saturation than SMY crude oil because the sandstones were water-wet with refined oil while mixed-wet with crude oil. For North Burbank, refined oil has similar S_{or} as crude oil because they were both mixed-wet. For both refined oil and crude oil systems, North Burbank has the smallest S_{or} due to its strongest mixed-wet condition. Berea has the highest S_{or} and has a 10% reduction of S_{or} from refined oil system to crude oil system. Bentheim, Berea, and North Burbank have similar CCI residual because it predicts the residual oil saturation when the rock is strongly water-wet. For North Burbank, CCI residual is significantly higher than S_{or} of refined oil and crude oil systems. This confirms that North Burbank is even mixed-wet with refined oil.

CONCLUSIONS

The NMR T_1 measurement is an effective tool in analyzing wettability alteration. Together with Amott wettability index and residual oil saturation estimate, they give a consistent description of wettability condition of core samples under various conditions. Our definition of mixed wettability is that the smallest pores contain only brine, thus are water-wet, while the larger oil-filled pores have the oil wetting the pore walls. Bentheim and Berea were water-wet with refined oil, but became mixed-wet with crude oil after aging. Due to the chlorite lining of North Burbank, it was mixed-wet even with refined oil. Wettability alteration does not always result in lengthening of the water relaxation time. However, in every case of wettability alteration, a shortening of the relaxation time of the residual oil was observed.

ACKNOWLEDGMENTS

The authors would like to acknowledge the financial support of Energy and Environmental Systems Institute in Rice University, USDOE, and an industrial consortium of Arco, Baker Atlas, Chevron, Exxon, GRI, Halliburton, Marathon, Mobil, Norsk Hydro, Phillips, Saga, Schlumberger, and Shell. We thank Peter Doe of Shell for centrifuge core preparation and supply of crude oil. We also thank Roger Shaver for helping with CCI measurements. The sandstone samples were provided by Shell, Phillips, and Norm Morrow (University of Wyoming).

REFERENCES

Amott, E., 1959, Observations relating to the wettability of porous rock, *Transactions, Society of Petroleum Engineers of AIME*, Vol. 216, p. 156-162.

Anderson, W. G., 1986-1987, Wettability literature survey – part 1 to part 6, *Journal of Petroleum Technology*, part 1 (1986, Vol. 38.2, No. 11, p. 1125-1144), part 2 (1986, Vol. 38.2, No. 12, p. 1246-1262), part 3 (1986, Vol. 38.2, No. 13, p. 1371-1378), part 4 (Vol. 39.2, No. 10, 1987, p. 1283-1300), part 5 (1987, Vol. 39.2, No. 11, p. 1453-1468), for part 6 (1987, Vol. 39.2, No. 12, p. 1605-1622).

Bobroff, S., Guillot, G., Kassab, G., Rivière, C., and Roussel, J. C., 1994, Microscopic arrangement of oil and water in sandstone by NMR relaxation times and NMR imaging, The 3rd International Symposium on Evaluation of Reservoir Wettability and Its Effect on Oil Recovery, Laramie, Wyoming, September 21-23.

Borgia, G. C., Fantazzini, P., Fanti, G., Mesini, E., Terzi, L., and Valdrè, G, 1991, A proton relaxation study of immiscible liquid arrangement in microporous structures, *Magnetic Resonance Imaging*, Vol. 9, No. 5, p. 695-702.

Brown, R. J. S. and Fatt, I., 1956, Measurements of fractional wettability of oilfield rocks by the nuclear magnetic relaxation method, *Transactions, Society of Petroleum Engineers of AIME*, Vol. 207, p. 262-264.

Craig, F. F., 1971, The reservoir engineering aspects of waterflooding, Monograph Volume 3 of the Henry L. Doherty Series, SPE.

Doughty, D. A. and Tomutsa, L., 1993, Investigation of wettability by NMR microscopy and spin-lattice relaxation, NIPER-720, prepared for U.S. Department of Energy.

Dunn, K. J., LaTorraca, G. A., Warner, J. L., and Bergman, D. J., 1994, On the calculation and interpretation of NMR relaxation time distributions, paper SPE 28367 presented at the 69th Annual Technical Conference and Exhibition of the SPE in New Orleans, LA, Sept. 25-28.

Fordham, E. J., Sezginer, A., and Hall, L. D., 1995, Imaging multiexponential relaxation in the (y, $\log_e T_1$) plane, with application to clay filtration in rock cores, *Journal of Magnetic Resonance*, series A Vol. 113, No. 2, p. 139-150.

Hirasaki, G. J., Rohan, J. A., Dubey, S. T., and Niko, H., 1990, Wettability evaluation during restored state core analysis, paper SPE 20506 presented at the 65th Annual Technical Conference and Exhibition of the SPE in New Orleans, LA, Sept..

Hirasaki, G. J., 1996, Dependence of waterflood remaining oil saturation on relative permeability, capillary pressure, and reservoir parameters in mixed-wet turbidite sands, SPE Reservoir Engineering, Vol. 11, No. 2, p. 87-91.

Howard, J. J., and Spinler, E. A., 1993, Nuclear Magnetic Resonance measurements of wettability and fluid saturations in chalk, paper SPE 26471 presented at the 68th Annual Technical Conference and Exhibition of the SPE in Houston, Texas, Oct..

Hsu, W.-F., Li, X., and Flumerfelt, R. W., 1992, Wettability of porous media by NMR relaxation methods, paper SPE 24761 presented at the 67th Annual Technical Conference and Exhibition of the SPE in Washington, DC, Oct..

Kovscek, A. R., Wong, H., and Radke, C. J., 1993, A pore-level scenario for the development of mixed wettability in oil reservoirs, *American Institute of Chemical Engineers Journal*, Vol. 39, No. 6, p. 1072-1085.

Marschall, D. M. and Coates, G., 1997, Laboratory MRI investigation in the effects of inverted oil muds on primary MRI log determinations, paper SPE 38739 presented at the 1997 Annual Technical Conference and Exhibition of the SPE in San Antonio, TX, Oct. 5-8.

Morriss, C. E., Freedman, R., Straley, C., Johnston, M., Vinegar, H. J., and Tutunjian, P. N., 1997, Hydrocarbon saturation and viscosity estimation from NMR logging in the Belridge diatomite, *The Log Analyst*, Vol. 38, No. 2, p. 44-59.

Morrow, N. R., 1990, Wettability and its effect on oil recovery, *Journal of Petroleum Technology*, Vol. 42.2, No. 12, p. 1476-1484.

Øren, P. E., Rueslåtten, H. G., Skjetne, T., and Buller, A. T., 1994, Some advances in NMR characterization of reservoir sandstones, North Sea Oil and Gas Reservoirs III, p. 307-316.

Ramakrishnan, T. S., Schwartz, L. M., Fordham, E. J., Kenyon, W. E., and Wilkinson, D. J., 1998, Forward models for Nuclear Magnetic Resonance in carbonate rocks, Society of Professional Well Log Analysts 39th Annual Logging Symposium, Keystone, CO., May 26-29.

Rueslåtten, H., Øren, P-E., Robin, M., Rosenberg, E. and Cuiec, L., 1994, A combined use of CRYO-SEM and NMR-spectroscopy for studying the distribution of oil and brine in sandstones, presented at the SPE/DOE 9th Symposium on Improved Oil Recovery, Tulsa, April 17-20.

Salathiel, R. A., 1973, Oil recovery by surface film drainage in mixed-wettability rocks, *Journal of Petroleum Technology*, Vol. 25.2, p. 1216-1224.

Saraf, D. N., Kumar, J., and Fatt, I., April, 1970, Determination of wettability of porous materials by the Nuclear Magnetic Resonance technique, *Indian Journal of Technology*, Vol. 8, p. 125-130.

Spinler, E. A., 1997, Determination of in-situ wettability from laboratory and well log measurements for a carbonate field, paper SPE 38733 presented at the Annual Technical Conference and Exhibition of the SPE in San Antonio, Texas, Oct..

Straley, C., Morriss, C. E., Kenyon, W. E., and Howard, J. J., 1991, NMR in partially saturated sandstones: laboratory insights into free fluid index, and comparison with borehole logs, paper C, in 32nd Annual Logging Symposium Transactions: Society of Professional Well Log Analysts.

Straley, C., Morriss, C. E., Kenyon, W. E., and Howard, J. J., 1995, NMR in partially saturated rocks: laboratory insights on free fluid index and comparison with borehole logs, *The Log Analyst*, Vol. 36, No. 1, p. 40-56.

Trantham, J. C. and Clampitt, R. L., 1977, Determination of oil saturation after waterflooding in an oil-wet reservoir – the North Burbank Unit, Tract 96 Project, *Journal of Petroleum Technology*, Vol. 29.1, p. 491-500.

Williams, C. and Fung, B. M., 1982, The determination of wettability by hydrocarbons of small particles by deuteron $T_{1\rho}$ measurement, *Journal of Magnetic Resonance*, Vol. 50, No. 1, p. 71-80.

Zhang, Q., Lo, S.-W., Huang, C. C., Hirasaki, G. J., Kobayashi, R., and House, W. V., 1998, Some exceptions to default NMR rock and fluid properties, 39th Annual Symposium of Society of Professional Well Log Analysts, Keystone Resort, CO., May 26-29.

Sub-Task 2.2 Diffusion in Internal Gradients:

INTERNAL FIELD GRADIENTS IN POROUS MEDIA

Gigi Qian Zhang, George J. Hirasaki, and Waylon, V. House
Rice University, Houston, TX

Abstract

Strong internal field gradients were observed on North Burbank (N. B.) sandstones and chlorite/fluid slurries. Evaluation of the effect of internal field gradients on nuclear magnetic resonance (NMR) spin-spin (T_2) relaxation is essential to formation evaluation. In this paper, systematic methods are developed to calculate magnetic fields and gradient distributions for three types of porous media. Magnetic fields of real systems like N. B. sandstone and chlorite slurry are simulated and gradient values from simulations are compared with experimental results.

For pores lined with clay flakes, field gradients are concentrated around the sharp corners of the clay flakes no matter the orientation of these clay flakes. The radius of curvature of the paramagnetic particle determines the maximum value of the field gradients. Pores lined with clay flakes have the dimensional gradient scaled to the width of clay flake, whereas for cylindrical or spherical systems, it is scaled to the radius of cylinder or sphere. So thin chlorite clay flakes will have much stronger gradients than larger spherical siderite particles.

Both N. B. sandstone and the chlorite slurry are simulated as a square pore lined with rectangular chlorite clay flakes with the fraction of micropores matching with that of real systems. The field gradients in the micropores of N. B. sandstone and those in between the clay flakes of chlorite slurry are similar. The mean gradient value of the big pore in the chlorite slurry is much higher than that of the macropore in N. B. sandstone. Both N. B. sandstone and chlorite slurry have much higher gradients than applied field gradients of logging tools.

T_1 and T_2 measurements at different echo spacings were performed on N. B. sandstone at various saturation conditions. Gradient values for the whole pore, micropore and macropore are determined from the slope of the first several data points on the plot of $1/T_2$ vs. τ^2. Gradient values from simulations using a clay width of 0.2 μm are close to experimental results for the whole pore and micropore. For the macropore, simulation matches the mean value of the experiments while individual experiment has larger variation. Simulation result for chlorite/fluid slurries with 0.2 μm clay width matches well to the mean gradient value of the experiments.

Introduction

A chlorite coated sandstone, North Burbank, showed significant departures from default assumptions about sandstone response in the interpretation of NMR logs (Zhang et al., 1998a, 1998b, 2001). These included strong echo spacing dependent shortening of NMR T_2 relaxation time distributions, large, echo spacing dependent surface relaxivity,

large T_1/T_2 ratio, and small T_2 cutoff for S_{wir}. These are due to spins diffusing in the strong internal field gradients induced by the pore lining chlorite flakes which have much higher magnetic susceptibility than surrounding pore fluids. Also, much stronger internal field gradients were observed in chlorite/fluid slurries than kaolinite/fluid slurries. Development of systematic methods to determine the magnetic fields and gradient distributions for complex porous media is essential to evaluate this diffusion effect in formation evaluation.

Historically, much research has been done to evaluate field inhomogeneities in heterogeneous systems. Menzel (1955) determined the distribution of magnetic field intensity for a sphere in a uniform external field. Durand (1968) gave the analytical solution of the magnetic fields induced by an isolated infinite diamagnetic cylinder placed in a medium of differing susceptibility. Roschach et al. (1973) estimated the field inhomogeneity in muscle samples which is derived for a sphere in a uniform field. Glasel and Lee (1974) expressed the analytical form for the induced fields due to a single spherical inclusion. The volume average of one component of the field gradient is determined. Eyges (1975) improved the integral equation method, previously derived by Phillips (1934) and exploited by Edwards and van Bladel (1961,1964), for solving the problem of a homogeneous permeable body of arbitrary shape in an external magnetostatic field by reducing it to the dielectric problem. Majumdar et al. (1988) developed a physical model for a suspension of spherical magnetized particles by considering the magnetostatic superposition of the fields induced by many microspheres randomly distributed in a medium of differing susceptibility. They also derived a relationship between the number density, composition and size of the particles and the variance of the resultant gradient field distribution. Bendel (1990) regarded the magnetic field of a saturated sand/water mixture as a superposition of many identical spherical particles. Zhong et al. (1991a, 1991b) modeled internal gradient distribution as Gaussian distribution to study the effects of susceptibility variations on NMR measurements of diffusion. Brown et al. (1993) used the magnetic dipole method to list the induced fields in a few idealized geometric shapes, like cone, wedge, cylinder, crack and sphere. Holt et al. (1994) verified the superposition of fields created by individual objects for a model of two spheres with reasonable accuracy. Bobroff et al. (1996) modeled the inhomogeneous magnetic field of the fluid surrounding infinite parallel cylinders in a regular square array. Hürlimann (1998) estimated effective field gradients, which relate to the field variations over the local dephasing length, for water-saturated sedimentary rocks. Clark et al. (1999) modeled the local magnetic susceptibility-induced gradients in human brain as Gaussian distribution.

In this paper, we will first develop theory and calculate the magnetic field and gradient distributions for three types of porous media: array of cylinders, array of spheres, and a square pore lined with clay flakes. Then we will simulate the pore space of chlorite coated North Burbank sandstone and chlorite/fluid slurry. Finally, we will compare the simulation results with experimental results.

Comparison of three types of porous media

Theory: Porous media are usually modeled as anarray of cylindrical or spherical particles. For an infinitely long cylinder or a sphere put in a homogeneous magnetic field (Figure 1a), magnetic dipole theory can be used to model the fields induced by these paramagnetic objects. For a cylinder, the induced fields can be viewed as those generated by two lines of current along the center of the cylinder, one flowing out and one in, with distance l apart. For a sphere, the induced fields arise from a ring of current at the center of the sphere (Figure 1b).

Additionally, a rectangular clay flake is modeled. For such a system, the clay/fluid interfaces are either parallel or perpendicular to the homogeneous magnetic field $\vec{B}_0$ (Figure 2a). Interfaces with other orientations can be decomposed into steps parallel and perpendicular to the applied field. Potential theory is developed as follows.

Start with Maxwell's equations:

$$\nabla \cdot \vec{B} = 0$$
$$\nabla \times \vec{H} = 0$$

and the nonferromagnetic condition:

$$\vec{B} = \mu_0 (1+\chi)\vec{H}$$

where χ is the magnetic volume susceptibility.

Since $\nabla \cdot \vec{B} = 0$, we can introduce a vector potential $\vec{A}$, such that $\vec{B} = \nabla \times \vec{A}$. With a series of steps and neglecting terms of $O(\chi^2)$, the following scalar partial differential equation is derived.

$$\frac{\partial^2 A_\delta}{\partial y^2} + \frac{\partial^2 A_\delta}{\partial z^2} = -B_0 \frac{\partial \chi}{\partial y} \qquad [1]$$

where A_δ is the vector potential deviating from that of the homogeneous magnetic field, $\vec{B}_0$. This equation states that A_δ satisfies the Laplace equation everywhere except at places where there is a change of χ over y. These places are the clay/fluid interfaces parallel to $\vec{B}_0$.

The right hand side of Eq. [1] is a singularity at the interface parallel to $\vec{B}_0$. However, the singularity is integratable to $-B_0 \Delta\chi$, where $\Delta\chi = \chi_{clay} - \chi_{fluid}$. Therefore, Eq. [1] can be rewritten as:

$$\frac{\partial^2 A_\delta}{\partial y^2} + \frac{\partial^2 A_\delta}{\partial z^2} = \begin{Bmatrix} \mp B_0 \Delta\chi \delta(y - y_0) & z \in C_{//} \\ 0 & z \notin C_{//} \end{Bmatrix} \qquad [2]$$

where y_0 is the y coordinate of the parallel interface. '–' sign is for the left parallel interface of the clay flake, whereas '+' sign is for the right parallel interface.

Since 2-D Green's function $G(y, z, y_0, z_0)$ satisfies Laplace equation everywhere except at singularity points (y_0, z_0), Green's function will give a solution to Eq. [2]. For

a single point of singularity along the interface (In analog of magnetostatics, it corresponds to a line of current with infinite length in x direction.), the solution is:

$$A_\delta^{line} = \frac{-B_0 \Delta\chi}{4\pi} \ln\left[(y-y_0)^2 + (z-z_0)^2\right] \qquad [3]$$

Then, for the interface parallel to $\vec{B}_0$ (viewed as a sheet of currents in magnetostatics, as shown in Figure 2b), the solution will be the integration of Eq. [3]:

$$\begin{aligned} A_\delta^{sheet} = {} & (z_{0u} - z)\log\left[(y-y_0)^2 + (z-z_{0u})^2\right] \\ & - 2z_{0u} + 2|y-y_0| \tan^{-1}\left(\frac{z_{0u}-z}{|y-y_0|}\right) \\ & - (z_{0l} - z)\log\left[(y-y_0)^2 + (z-z_{0l})^2\right] \\ & + 2z_{0l} - 2|y-y_0| \tan^{-1}\left(\frac{z_{0l}-z}{|y-y_0|}\right) \end{aligned}$$

where z_{0l} and z_{0u} are the z coordinates of the lower and upper ends of the parallel interface respectively. A_δ is then just the summation of A_δ^{sheet} over all parallel interfaces.

Knowing A_δ, the magnetic field gradient can be solved analytically. The gradient, $\bar{\bar{G}} = \nabla\vec{B}$, is a second order tensor. We define the magnitude of the gradient, $\left|\bar{\bar{G}}\right|$, as the square root of the absolute value of the only non-zero invariant of this tensor (Aris, 1989), i.e.,

$$\left|\bar{\bar{G}}\right| = \sqrt{G_{yz}^2 + G_{zz}^2}$$

where $G_{yz} = -\frac{\partial^2 A_\delta}{\partial y^2}$ and $G_{zz} = -\frac{\partial^2 A_\delta}{\partial y \partial z}$. It can be proved that $\left|\bar{\bar{G}}\right| = \left|\nabla|\vec{B}|\right|$. The magnitude of the gradient is made dimensionless with respect to the characteristic length, strength of the homogeneous magnetic field B_0, and magnetic volume susceptibility.

Results and Discussions: Contour lines of the dimensionless gradients of the induced fields for a single cylinder, sphere and clay flake are shown in Figure 3. For a sphere it is for the vertical plane through the center of the sphere. The values of the contour lines differ by a factor of 2. The field gradients are higher near the surface of the sphere than that of the cylinder. However, for the clay flake, on the whole, the induced field has higher gradients. Most importantly, much higher gradients are around the corners of the clay flake. The gradient at the corner will approach infinity as the resolution of the calculation grid is refined. Therefore, the radius of curvature of the paramagnetic particle determines the maximum value of gradients.

With superposition, an infinite cubic array of cylinders or spheres can be modeled. With 36 cylinders or 64 spheres, the resultant fields can well represent those of an infinite array. Contour lines of the dimensionless gradients are drawn for the central

pore space of a cubic array of 36 cylinders and for the vertical plane passing through the centers of the spheres at the innermost region of a cubic array of 64 spheres (Figure 4 a, b). Similarly, by superposition of Green's function, field gradients can be determined for a square pore lined with clay flakes. It is a system with two distinct pore sizes. One is the small pores in between clay flakes, referred to as micropores, the other is the central big pore, referred to as a macropore. It can be observed from Figure 4c that strong gradients are concentrated around the tips of clay flakes no matter the orientation of these clay flakes. Table 1 compares the mean value and standard deviation of the gradients. For the sphere system, the values are for the whole central pore volume. It can be concluded that infinite cubic array of spheres has higher gradient values than infinite cubic array of cylinders. Even though the mean value of the gradients of the clay flake system is similar to that of the cylinder and sphere system, the standard deviation is much higher because gradients are very high at the corners of the clay flakes.

Normalized cumulative distributions of dimensionless gradients are shown for an infinite cubic array of cylinders or spheres with different porosities, or a square pore lined with clay flakes with different fractions of micropores in Figure 5. Median value and the 95 percentile are marked by two dashed horizontal lines. Comparing the gradient values at the 95% line, it can be clearly observed that the values doubled from cylinder system to sphere system and then to clay flake system. For clay flake system, the maximum gradient value is infinite.

The following three equations convert dimensionless gradient to dimensional gradient for the cylinder, sphere and clay flake system respectively.

$$\left|\bar{\bar{G}}\right| = \frac{k-1}{k+1}\frac{B_0}{a}\left|\bar{\bar{G}}^*\right| \quad \text{for cylinder system}$$

$$\left|\bar{\bar{G}}\right| = \frac{k-1}{k+2}\frac{B_0}{a}\left|\bar{\bar{G}}^*\right| \quad \text{for sphere system}$$

$$\left|\bar{\bar{G}}\right| = \frac{\Delta\chi}{4\pi}\frac{B_0}{w}\left|\bar{\bar{G}}^*\right| \quad \text{for clay flake system}$$

where $k = \dfrac{1+\chi_{particle}}{1+\chi_{fluid}}$, a is either the radius of the cylinder or sphere, and w is the width of the clay flake. For cylinder and sphere systems, $\dfrac{k-1}{k+1}$ and $\dfrac{k-1}{k+2}$ are all in the order of $\Delta\chi$. However, the dimensional gradients are scaled to the radius of the cylinder or sphere whereas for the clay flake system, they are scaled to the width of the clay flake. This is very important because for the clay flake system, like pointedly shaped chlorite clays, the width is in the order of 0.1μm. For spherical systems like siderite crystals, their dimensions are in the order of 10 μm. So even though there is a factor of three between the χ values of siderite and chlorite, the difference due to dimensions is 100 times. So thin chlorite clay flakes will have much stronger gradients than larger spherical siderite particles.

Magnetic field simulation for N. B. sandstone and chlorite slurry

The magnetic fields of N. B. sandstone and chlorite slurry are simulated with the model of a square pore lined with clay flakes. First we need to determine the typical shape and spacing of the chlorite clay flakes. Based on the photomicrograph shown in Figure 6, we set the height of the clay flake as seven times the width, and the fluid gap between two clay flakes as the clay width. In the calculations, we will not consider the four corners. As the number of clay flakes on each side, (denoted as N) increases, the volume fraction of micropores decreases. With N below 3, the system is not realistic. If N equals 3, the fraction of micropores is 0.69 and decreases to 0.32 when N is 15. For the N. B. sandstone, the average S_{wir} from air-brine desaturation is 33%, so the fraction of micropores is 0.33. Therefore, N equals 15 is the choice for N. B. sandstone. For chlorite slurry, pores in between the clay flakes should be in abundance compared to the big pore formed by irregular stacking, so, N equals 3 and the fraction of micropores is 0.69.

The contour lines of dimensionless gradients for the whole pore of the N. B. sandstone and chlorite slurry are shown in Figure 7. The values of the contour lines differ by a factor of 2. For both systems, high gradients occur around the clay tips. Lower gradients are in the middle portion of the micropores and macropore. Contour lines of very weak gradients are closed and appear in between the clay flakes near the tips. These arise from the symmetry in the calculation. Be cautious not to let them mislead you as high gradients, which are actually at the corners.

Figure 8 shows the contour lines of dimensionless gradients for the micropores of N. B. sandstone and those in between the clay flakes of chlorite slurry. By looking at the positions of two contour lines of 20.5 and 0.32 and comparing the maximum, mean and standard deviation values, it can be concluded that the gradient distributions are similar in these two systems.

Figure 9 shows the contour lines of dimensionless gradients for the macropore of N. B. sandstone and the big pore of chlorite slurry. Due to the relatively large fraction of the macropore (0.68) in N. B. sandstone, a large portion of the macropore has relatively small gradients compared to the region near the clay tips. Whereas for chlorite slurry, the decay from high gradients to low gradients spans the whole big pore. Therefore, although very similar maximum values are achieved at the corners of the clay flakes for both systems, the mean value for chlorite slurry is much higher than that of N. B. sandstone, and the standard deviation is about twice as high. Dimensional gradient values in unit of gauss/cm can be easily determined from dimensionless values through the width of clay flakes. Using a clay width of 0.2 μm, the contour line of 0.01 is approximately 2 gauss/cm and the contour line of 0.16 is roughly 32 gauss/cm, close to the applied field gradients of logging tools. So, the magnetic field in the macropore of N. B. sandstone is not homogeneous, and gradients in the macropore still have considerable strength.

Comparison of simulations with experiments

For a square pore lined with chlorite clay flakes, dimensionless gradients for the whole pore, micropores and macropores are plotted as a function of the fraction of micropores in Figure 10. Solid line is the mean value and the dashed line is mean plus

standard deviation. As fraction of micropores increases, the mean and standard deviation of the dimensionless gradient remain almost unchanged for the micropores, while they increase for the macropore. The effect on the whole pore is in between the two. The simulation of N. B. sandstone is at the left end of the curves with the fraction of micropores of 0.32 and the simulation of the chlorite slurry is at the right end with the fraction of micropores of 0.69. The dimensionless gradient values for the whole pore, micropore and macropore of N. B. sandstone are shown on the figure, whereas for the chlorite slurry, only the value for the whole pore is considered. For other porous systems, the dimensionless gradient values can be looked up from these curves using a value of the fraction of micropores determined from S_{wir}. Table 2 lists the dimensional gradient values using a clay width of 0.2 μm. The gradient value for the whole pore of N. B. sandstone is in between the values for micropore and macropore, and they are all much higher than the applied field gradients of logging tools. The gradient in the whole pore of the chlorite slurry is about twice as high as that of N. B. sandstone. This is consistent with the experimental data.

T_1 and T_2 measurements at different echo spacings were performed on N. B. sandstone at various saturation conditions. Take 100% brine saturation as an example. Figure 11 shows the relaxation time distributions of T_1 and T_2 at the smallest echo spacing of 0.2 ms, up to the longest echo spacing of 2 ms. All distributions are bi-modal, with distinct peaks for brine response in micropores and macropores. To quantify the shifting of the distributions, log mean values were used for the whole pore, and mode values for micropores and macropores were estimated by fitting the peaks to a quadratic. $1/T_2$ vs. τ^2 are shown for the whole pore, micropore and macropore in Figure 12. $1/T_1$ is marked by a solid square at zero echo spacing. On each plot, results of three samples are shown for comparison. The data points are a little noisy but consistent among the three samples. For micropores, $1/T_2$ decreases at larger echo spacings because more fast-relaxing components are lost before the acquisition of the first echo. However for the whole pore, $1/T_2$ also decreases at larger echo spacings. And for macropore, $1/T_2$ first increases, levels off, then goes up again. Besides the uncertainty of the experiments, there may be reasons behind these phenomena since the field gradients are not uniformly distributed. At present, we still fit the first several data points to a straight line and then determine the gradient from the slope.

Mean values of the dimensional gradients from simulations are compared with experimental results for the whole pore, micropores and macropores of N. B. sandstone in Figure 13. The gray shaded bar is from simulation. Four hashed bars are from experiments at conditions of 100% brine saturation, SMY crude oil with brine at S_{wir} before aging, after aging and after forced imbibition of brine respectively. Error bars show the standard deviation among three samples. For the whole pore, brine diffusivity is used to calculate gradient from the slope for 100% brine saturated condition. A diffusivity value that is an average between that of brine and SMY crude oil according to the saturation is used for the other three conditions. For micropores, since they are always filled with brine, brine diffusivity is used for all four conditions. For macropores, brine diffusivity is used for the 100% brine saturated condition and after forced imbibition, while crude oil diffusivity is used for conditions of before aging and after aging. It can be

observed that simulation results are close to experimental results for the whole pore and micropore. However, the simulations give a good approximation to the mean value of the experiments for the macropore, but the experiments have a larger variation among different saturation conditions.

T_1 and T_2 measurements at different echo spacing were performed on four chlorite/fluid slurries. Figure 14 shows the relaxation time distributions with hexane as the fluid. The bold solid curve is T_1 for bulk hexane, the regular solid curve is T_1 for chlorite/hexane slurry, so there is some surface relaxation. The dashed curve is T_2 at echo spacing of 0.2 ms and the dotted curve is at echo spacing of 2 ms. So, there is a strong internal field gradient. Mode values from quadratic fitting are used to quantify the shifting of distributions. Figure 15 plots $1/T_2$ vs. τ^2 for chlorite/brine, hexane, soltrol and SMY crude oil slurries. Again, $1/T_1$ is shown as a solid square at zero echo spacing. The first several data points fit to a straight line, then as echo spacing increases, $1/T_2$ levels off. The mean gradient value from experiments is 350 gauss/cm, shown as the blank bar in Figure 16. Standard deviation is for the four fluids. Our simulation result matches well with the mean value of the experiments.

Conclusions

Magnetic dipole theory can be used to model cylindrical and spherical systems, while potential theory can be used to model more complex pore structures. For pore lined with clay flakes, the deviation of the vector potential from that of the homogeneous field satisfies Laplace equation everywhere except along clay/fluid interfaces parallel to the homogeneous magnetic field. Thus, this induced magnetic field can be solved analytically by means of superposition of Green's function.

Dimensionless magnetic field gradients are higher in a system of spheres than system of cylinders. For pore lined with clay flakes, field gradients are much higher at sharp corners (singularity points). Therefore, the radius of curvature of the paramagnetic object determines the maximum value of gradients.

Both N. B. sandstone and chlorite slurry are simulated by matching the fraction of micropores with that of real systems. The simulation results using a clay width of 0.2 μm match well with experimental results for both N. B. sandstone and chlorite slurry.

Acknowledgments

The authors would like to acknowledge the financial support of Energy and Environmental Systems Institute in Rice University, US DOE, and an industrial consortium of Arco, Baker Atlas, Chevron, Exxon, GRI, Halliburton, Marathon, Mobil, Norsk Hydro, Phillips, Saga, Schlumberger, and Shell. The authors thank Baker Atlas for the chlorite sample, Exxon for magnetic susceptibility measurements, Phillips for North Burbank samples, Norm Morrow for the Bentheim samples, and Shell for core sample preparations.

References

Aris, R., 1989, Vectors, Tensors, and the Basic Equations of Fluid Mechanics, Dover Publications, INC., New York, pp26.

Bendel, P., 1990, "Spin-Echo Attenuation by Diffusion in Nonuniform Field Conditions," *Journal of Magnetic Resonance*, 86, 509.

Bladel, J. V., 1964, *Electromagnetic Fields*, McGraw-Hill, New York.

Bobroff, S. and Guillot, G., 1996, "Susceptibility Contrast and Transverse Relaxation in Porous Media: Simulations and Experiments," *Magnetic Resonance Imaging*, 14, 819.

Brown, R. J. S. and Fantazzini, P, 1993, "Conditions for initial quasilinear T_2^{-1} versus τ for Carr-Purcell-Meiboom-Gill NMR with diffusion and susceptibility differences in porous media and tissues," *Physical Review B*, 47, 14,823

Clark, C. A., Barker, G. J., and Tofts, P. S., 1999, "An in Vivo Evaluation of the Effects of Local Magnetic Susceptibility-Induced Gradients on Water Diffusion Measurements in Human Brain," *Journal of Magnetic Resonance*, 141, 52.

Duffin, W. J., 1990, *Electricity and Magnetism*, 4th ed., McGraw-Hill UK.

Durand, E., 1968, *Magnétostatique*, Paris: Masson, pp 373.

Edwards, T. W. and Bladel, J. V., 1961, *Applied Scientific Research*, B9, 151.

Eyges, L., 1975, "Irregular Dielectric or Permeable Bodies in an External Field," *Annals of Physics*, 90, 266

Feynman, R. P., Leighton, R. B., and Sands, M, 1964, *Lectures on Physics*, Vol. 2, Addison-Wesley Publishing Company.

Glasel, J. A. and Lee, K. H., 1974, "On the Interpretation of Water Nuclear Magnetic Resonance Relaxation Times in Heterogeneous Systems," *Journal of American Chemical Society*, 96, 970.

Holt, R. W., Diaz, P. J., Duerk, J. L., and Bellon, E. M., 1994, *Journal of Magnetic Resonance Imaging*, 4, 809.

Hürlimann, M. D., 1998, "Effective Gradients in Porous Media Due to Susceptibility Differences," *Journal of Magnetic Resonance*, 131, 232.

Majumdar, S. and Gore, J. C., 1988, "Studies of Diffusion in Random Fields Produced by Variations in Susceptibility," *Journal of Magnetic Resonance*, 78, 41.

Menzel, D. H., 1955, *Fundamental Formulas of Physics*, Prentice-Hall, New York, N. Y., pp 315 and 325.

Phillips, H. B., 1934, "Effect of Surface Discontinuity on the Distribution of the Potential," *Journal of Mathematical Physics*, 13, 261.

Roschach, H. E., Chang, D. C., Hazelwood, C. F., and Nichols, B. L., 1973, *ibid.*, 204, 444.

Trantham, J. C. and Clampitt, R. L., 1977, "Determination of oil saturation after waterflooding in an oil-wet reservoir – the North Burbank Unit, Tract 96 Project", *Journal of Petroleum Technology*, May, 491.

Zhang, Q., Lo, S.-W., Huang, C. C., Hirasaki, G. J., Kobayashi, R., and House, W. V., 1998a, "Some exceptions to default NMR rock and fluid properties", 39th Annual Symposium of Society of Professional Well Log Analysts, Keystone Resort, CO., May 26-29.

Zhang, Q., Hirasaki, G. J., and House, W. V., 1998b, "Diffusion in internal field gradients", 1998 International Symposium of the Society of Core Analysts, the Hague, the Netherlands, Sept. 14-16.

Zhang, Q., Hirasaki, G. J., House, W. V., 2001 "Effect of Internal Field Gradients on NMR Measurements," *Petrophysics*, 42.1 (January-February), 37-47.

Zhong, J., Kennan, R. P., and Gore J. C., 1991a, "Effects of Susceptibility Variations on NMR Measurements of Diffusion," *Journal of Magnetic Resonance*, 95, 267.

Zhong, J. and Gore J. C., 1991b, *Magn. Reson. Med.*, 19, 276.

Table 1. Comparison of the mean values and standard deviations of dimensionless gradients for an infinite cubic array of cylinders (The distance between the centers of two cylinders is $3a$, with ϕ=65.1%.), spheres (same, except ϕ=84.5%), and a square pore with 15 clay flakes on each side (f_micro=0.32).

$\left\|\bar{\bar{G}}^*\right\|$	mean	std. dev.
array of cylinders	0.62	0.45
array of spheres	0.89	0.91
pore lined with clay flakes	0.81	2.28

Table 2. Dimensional gradient values for the simulation of N. B. sandstone and chlorite slurry.

$\left\|\bar{\bar{G}}\right\|$ (gauss/cm)	whole pore	micro-pores	macro-pores
N. B. sandstone	168	248	134
chlorite slurry	390	—	—

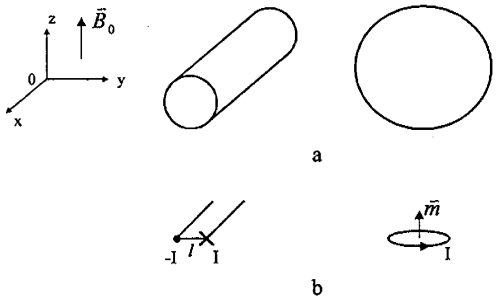

Figure 1. Paramagnetic particles of infinite cylindrical or spherical shape in a homogeneous magnetic field (a). Magnetic dipole theory for modeling the induced fields (b).

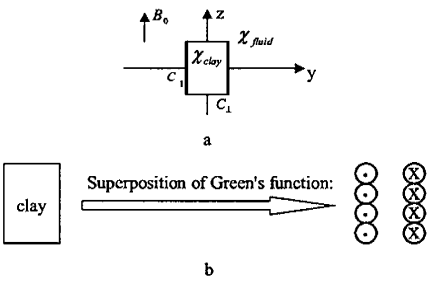

Figure 2. A rectangular clay particle in a fluid with interfaces either parallel or perpendicular to the homogeneous magnetic field (a). Green's function solves A_δ for a clay flake in a fluid, which in analog of magnetostatics, corresponds to two sheets of current flowing in opposite directions (b).

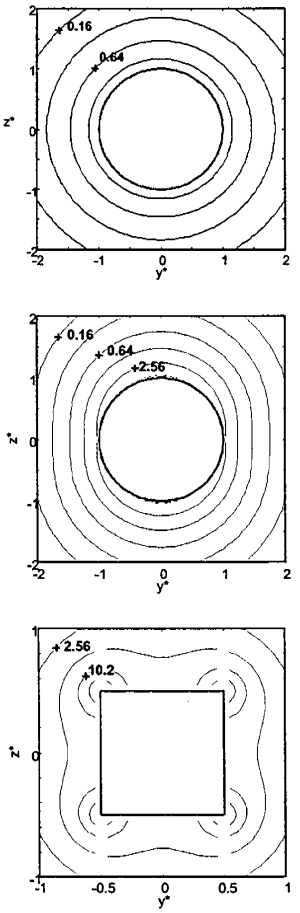

Figure 3. Contour lines of dimensionless gradient for a single cylinder, sphere and clay flake.

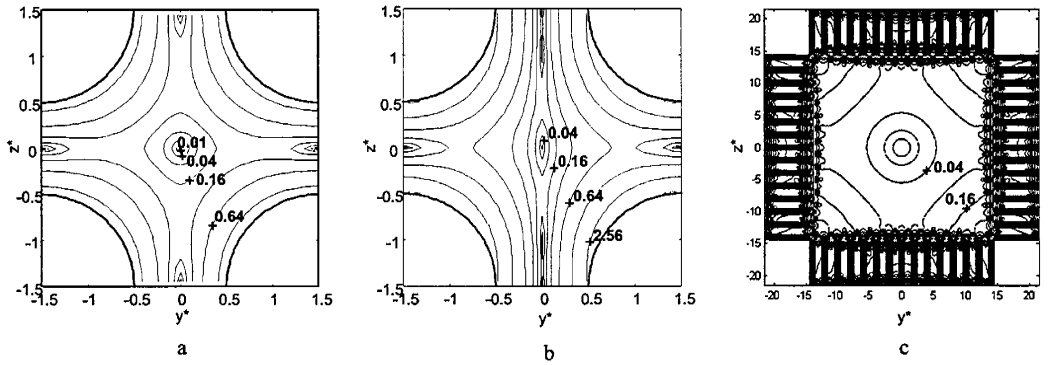

Figure 4. Contour lines of the dimensionless gradients for the central pore space of a cubic array of 36 cylinders (a); for the vertical plane passing the centers of spheres at the innermost of a cubic array of 64 spheres (b); for a square pore lined with 15 clay flakes on each side (c).

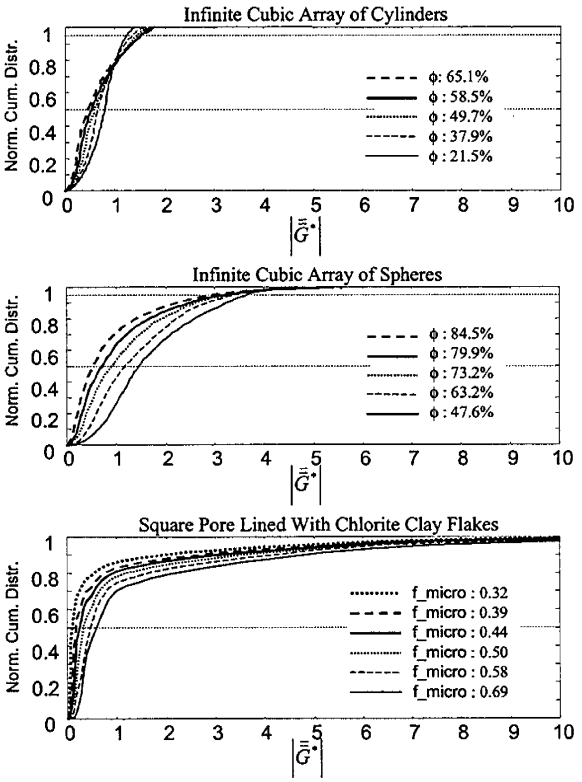

Figure 5. Normalized cumulative distributions of dimensionless gradients for an infinite cubic array of cylinders or spheres with different porosities, or a square pore lined with clay flakes with different fractions of micropores.

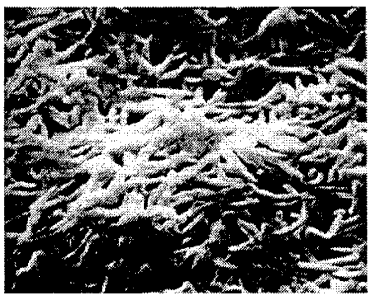

Figure 6. Photomicrograph of North Burbank sand grain showing chlorite coating (adapted from Trantham and Clampitt, 1977).

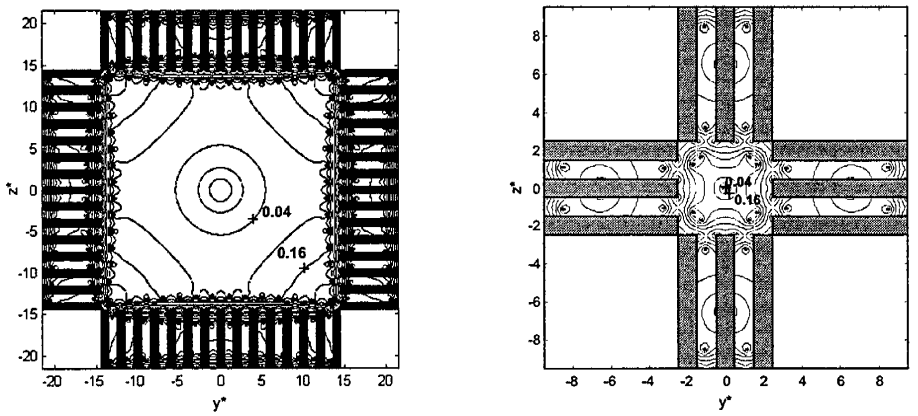

Figure 7. Contour lines of the dimensionless gradients for the whole pore for the simulation of N. B. sandstone (left) and chlorite slurry (right). The corners are not included as part of the system.

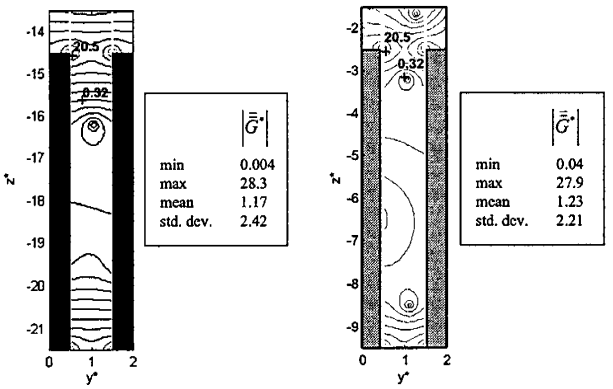

Figure 8. Contour lines of the dimensionless gradients for the micropore of N. B. sandstone (left) and those in between the clay flakes of chlorite slurry (right).

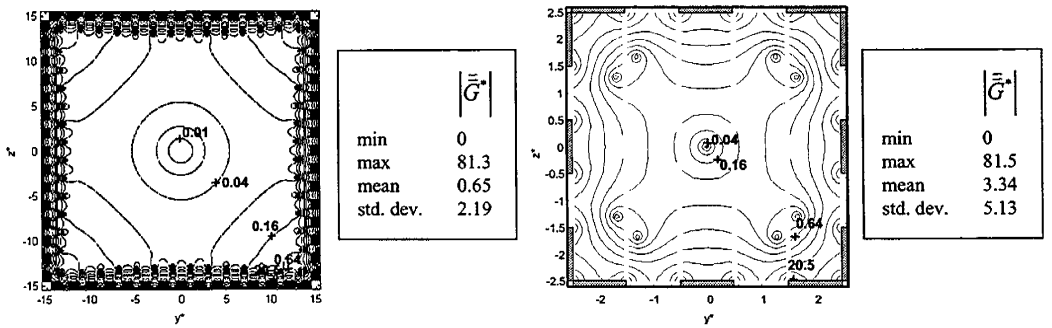

Figure 9. Contour lines of the dimensionless gradients for the macropore of N. B. sandstone (left) and the big pore of chlorite slurry (right).

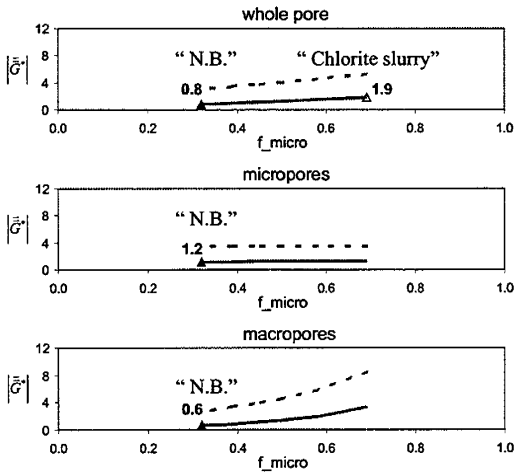

Figure 10. Dimensionless gradients as a function of the fraction of micropores for the whole pore, micropore and macropore of a square pore lined with chlorite clay flakes. The simulation of N. B. sandstone is at the fraction of micropores of 0.32, while the simulation of chlorite slurry is at the fraction of micropores of 0.69.

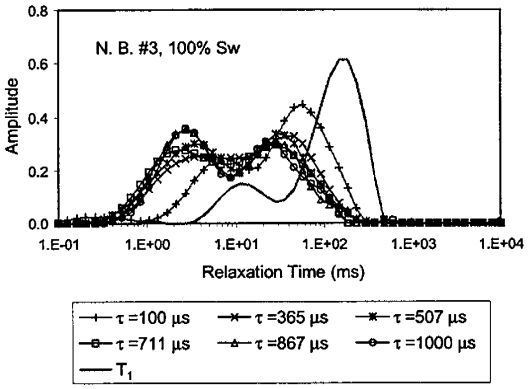

Figure 11. The relaxation time distributions of T_1 and T_2 at different echo spacings for a N. B. sandstone at 100% brine saturated condition.

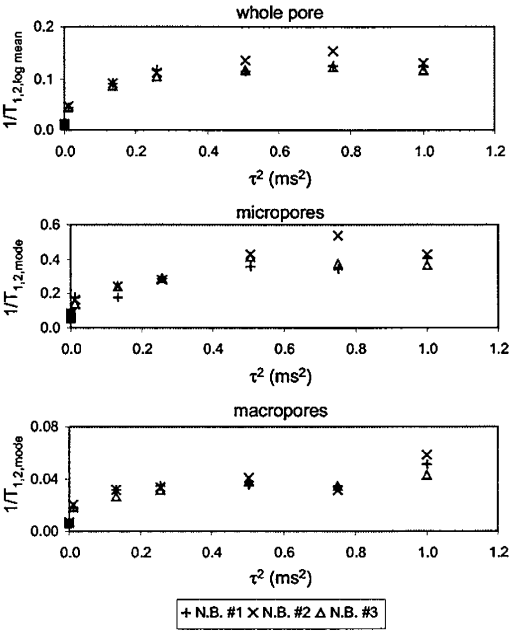

Figure 12. $1/T_2$ vs. τ^2 for the whole pore, micropores and macropores of a N. B. sandstone at 100% brine saturated condition. $1/T_1$ is shown as a solid square at zero echo spacing.

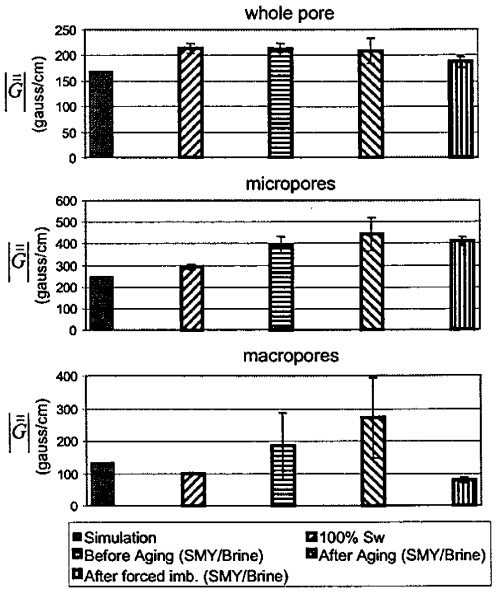

Figure 13. Comparison of dimensional gradient values from simulations with experimental results for the whole pore, micropores and macropores of N. B. sandstone.

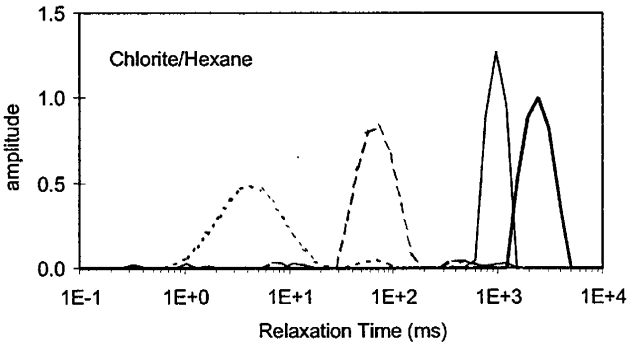

Figure 14. Relaxation time distributions for chlorite/hexane slurry: regular solid curve corresponds to T_1, dashed curve to T_2 at echo spacing of 0.2 ms, and dotted curve to T_2 at echo spacing of 2 ms. T_1 for bulk hexane is also shown as the bold solid curve.

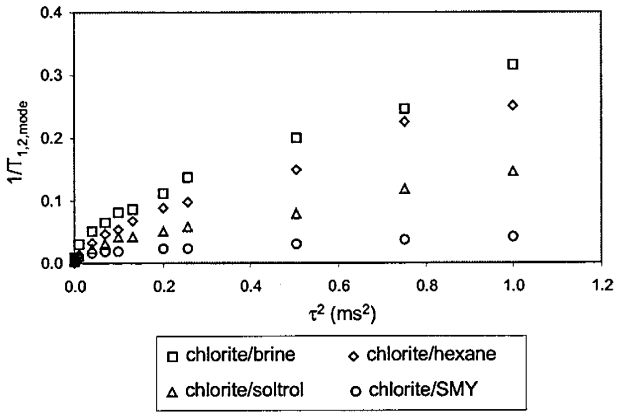

Figure 15. $1/T_2$ vs. τ^2 for four chlorite/fluid slurries. $1/T_1$ is shown as solid square at zero echo spacing.

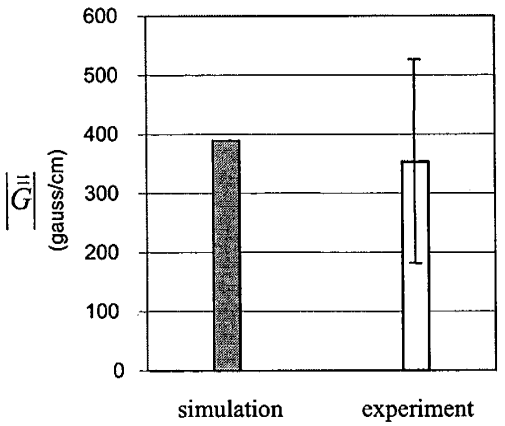

Figure 16. Comparison of dimensional gradient value from simulation with experimental results for chlorite slurry.

Task 3.0 Pore Morphology / Rock Characterization

Subcontract to Rice University on

DOE Award Number: DE-AC26-99BC15201

Annual Report

Reporting Period Start Date: 8-1-1999

Reporting Period End Date: 7-31-2000

Kishore K. Mohanty

August 2000

University of Houston

4800 Calhoun Road

Houston, TX 77204-4792

Abstract

A pore reconstruction method has been developed to recreate three-dimensional porous media from two-dimensional images that reproduce some of its key statistical properties. A Monte Carlo simulation technique has been developed to calculate the magnetization decay in fluid saturated porous media given its pore structure. In order to mimic real porous media, spatially correlated porous media are generated. Permeability of these media is computed by the lattice Boltzmann method. NMR relaxation response of these media is simulated by a random walk technique. The formation factor of these media is computed by solving a Laplacian equation. The testing of commonly used NMR permeability correlations shows that three conditions should be met for the validity of these correlations. The surface relaxivity should not vary significantly. The formation factor should depend only on porosity. And the characteristic pore body radius should be proportional to the characteristic throat radius. The correlations are modified by including surface relaxivity and formation factor. Ten carbonate core plugs have been borrowed from Shell. In the next six months, we anticipate determining NMR response and transport properties of these samples.

1. Introduction

The goal of this research is to develop a mechanistic model of NMR response and petrophysical properties for vuggy carbonates. Vuggy carbonates have been problematical because the vugs may be too large for the fast diffusion limit and although the vugs contribute to the porosity, they may not contribute to the permeability if they are not well-connected. The concepts from percolation theory and network modeling may give insight into porosity-permeability correlation of vuggy carbonates. Also, measurement of restricted diffusion may offer an estimate of the connectivity of the pore system. This work is subdivided into three sub-tasks: Sub-Task 3.1 Microscopic Imaging, Sub-Task 3.2 Corefloods and CT Imaging, Sub-Task 3.3 Network Modeling.

Sub-Task 3.1 Microscopic Imaging: Thin-sections of the porous media will be imaged and digitized. Three-dimensional images of the pore structure will be recreated on the basis of the porosity and three statistical spatial functions measured on the two-dimensional images. The three statistical spatial functions are: two-point autocorrelation function, chord-length distribution function and lineal path function. The reconstruction process is performed by a simulated annealing method which is discussed in more detail in the next section.

Sub-Task 3.2 Corefloods and CT Imaging: Core analysis will be performed on the carbonate cores to determine porosity, permeability, irreducible water saturation and residual oil saturation. The cores will be CT (computer tomography) scanned to identify the vugs, their macroscopic distribution, effective porosity and dead end porosity. The combination of the microscopic and CT imaging will provide the morphology of the pore structure. Core have been acquired from Shell Rock Catalog to conduct this study; it is discussed in detail in Section 3.

Sub-Task 3.3 Network Modeling: A differential material balance equation can be derived for the fluid magnetic moment during an NMR experiment of a porous rock; it is a reaction-diffusion equation with both bulk reaction and surface reaction (surface relaxivity). A particle-based Monte Carlo technique has been developed to solve the differential equation and has been validated against the analytical solutions for simple-shaped pores. The reconstructed porous media derived from Sub-Task 3.1. will allow us to perform Monte Carlo simulation in porous media that approximate the actual carbonate samples. Reconciliation of pore morphology, core properties and NMR response will help us understand NMR logging mechanistically. The Monte Carlo simulation technique is described in more detail in Section 4.

2. Stochastic Reconstruction of 3D Porous Media by Simulated Annealing Method

With advances in computer, simulations can be done at a smaller scale than before. In fluid dynamics, simulation of flow and transport in porous media can be done by random-walk techniques and lattice Boltzman methods. Brownian motion in constricted porous media can be simulated and effective diffusion and reaction rate can be calculated. Pore-level modeling can be performed to simulate as close as possible the actual physical event in the porous media. However, all these methods are still using assumptions that simplify the pore geometry, such as using spherical pore bodies and cylindrical pore throats connected in a regular lattice. With reconstruction techniques, these simulations can be done in more realistic pore geometry.

A number of reconstruction techniques can be found in the literature. An extensively studied reconstruction method is the convolution method, which basically convolutes linearly a normalized uncorrelated random Gaussian field to give a correlated random Gaussian field. Then this Gaussian field is passed through a nonlinear filter to yield the discrete values of the final structure. Another method is by simulated annealing, which we reported in our last report issued on January 28, 2000. Simulated annealing is an optimization method that minimizes the "Energy" by changing the spatial arrangement of the phase voxels of interest. In this case, the energy is the the sum of the squared difference between the reference function (determined on the real medium) and the reconstructed image function. The simulated annealing method has the following advantages over the convolution method:

1. The method is very simple to implement compared to the convolution technique which requires solving a nonlinear system of equations.

2. It preserves the porosity.

3. We can include any type and any number of statistical functions.

The key challenges that are met in porous media reconstruction are selecting appropriate statistical properties or functions that can capture important features of the porous media. Other important issues include having enough properties that allow acceptable reconstruction but not too many that the CPU is bogged down with excessive calculations. Also, what determines if a particular reconstruction is 'good enough?' If these challenges can be overcome, reconstruction techniques offer a fast, cheap, and nondestructive way to estimate macroscopic properties of porous media.

In order to represent a given porous medium exactly, an infinite set of statistical functions is needed. However, we are limited by the practical aspect of extracting statistical functions from the reference structure in a reasonable amount of time. We choose four statistical functions to determine the real and generated images: one-point pore correlation function (porosity), two-point pore-pore correlation function, chord length,

and lineal path length distributions. The porosity is defined as the volume fraction of the pore space. The two-point pore-pore correlation function, or autocorrelation function, is the probability that two points are both in the pore space for a given distance and direction. Chord length is the length through the pore space in between two rock voxels for a given direction. The distribution is obtained by dividing the total number of individual chord lengths by the total number of chords found. Lineal path length is the length through the pore space whether bounded by two rock voxels or not. Its distribution is determined by normalizing the total number of individual lineal path lengths by the number of lineal path lengths of length equal to 1.

In this present work, we study the effect of different combination of statistical functions. First, we reconstruct reference structures by the convolution method (refer to section "Calculation of Transport Properties of Microporous Media by Simulated NMR Response). Second, we perform 3D reconstruction with different combinations of statistical functions. Finally we compute the macroscopic properties of the structures; specific surface area (S/V), permeability and formation factor. We also do the sensitivity study of random number seed and the initial guess on the reconstructed structure.

2.1 SIMULATED ANNEALING METHOD

For a 3D binary image, a phase function $Z(i, j, k)$ is defined as

$$Z(\mathrm{i,j,k}) = \begin{Bmatrix} 1 & \text{if the voxel at position (i, j, k) is in the pore space} \\ 0 & \text{otherwise} \end{Bmatrix} \quad (1)$$

The porosity is the probability that a voxel will be in the pore space, or

$$\phi = \overline{Z(\mathrm{i,j,k})} \quad (2)$$

The 2-point autocorrelation function $S_2(r)$ is the probability that two voxels are both in the pore space at a given distance r for a particular direction,

$$S_2(r) = \frac{\overline{(Z(i,j,k)-\phi)(Z(i,j,k+r)-\phi)}}{(\phi-\phi^2)} \quad (3)$$

This function is the same for all directions for isotropic media.

The initial guess for the simulated annealing method is an image with randomly placed 0's and 1's with an equivalent porosity as the real data. The porosity is then guaranteed to be correct from the outset. Basically the initial guess can be any structure as long as it has

the same porosity. The energy E is represented by the sum of the squared difference between the reference function (f_{ref}) and the reconstructed image function (f_{out}):

$$E = \sum_i \left[f_{ref}(r_i) - f_{out}(r_i) \right]^2 \tag{4}$$

For a combination of functions, this can be written as

$$E = \sum_j \sum_i \alpha_j \left[f_{ref,j}(r_i) - f_{out,j}(r_i) \right]^2 \tag{5}$$

where j is the number of the functions and α_j is the weight for the corresponding function. In this paper, we use the same weight for each function.

Then we randomly choose two voxels of opposite phase and swap them. The new energy E' is calculated for the new arrangement and the energy difference $\Delta E = E - E'$ between the two iterations is also determined. This move is accepted by the following rule

$$p(\Delta E) = \begin{cases} 1, & \Delta E \le 0 \\ \exp(-\Delta E / T), & \Delta E > 0 \end{cases} . \tag{6}$$

A swap that lowers the energy will always be accepted, but the move that increases the energy will be accepted by a probability so that trapping by local minima is avoided. T is the cooling schedule and is decreased during the simulation by a commonly used power law schedule, $T_i = \lambda T_{i-1}$.

2.2 GENERATION OF REFERENCE STRUCTURE

We use the convolution method to generate the reference structure, the same method used in section "Calculation of Transport Properties of Microporous Media from Simulated NMR Response". Here, we just give a brief overview of the method.

An uncorrelated Gaussian field $\xi_\lambda(\underline{\mathbf{x}})$ is generated. A linear filter with exponential kernel will linearly convolute the uncorrelated Gaussian field, yielding a correlated Gaussian field, $Y(\underline{\mathbf{x}},\lambda)$ The convolution process is given by

$$Y(\underline{\mathbf{x}}, \lambda) = \left(\frac{4\lambda}{\pi} \right)^{d/4} \int_{E^d} \exp\left(-2\lambda u^2\right) \xi_\lambda(\underline{\mathbf{u}} + \underline{\mathbf{x}}) d\underline{\mathbf{u}} \ . \tag{7}$$

Exponential kernel is chosen because most of the correlation functions of the rock porous media exhibit exponential behavior. The relationship between λ and the correlation length L_c is given by $\frac{L_c}{a} = \frac{2}{a\sqrt{\lambda}}$. It should be noted that the correlation length L_c is inversely proportional to the square root of λ. In this work, we use the term λ instead of L_c. Finally, the Gaussian correlated field is transformed into a binary correlated field of desired porosity (ϕ) by the following non-linear filter:

$$Z = G(Y, \phi) \quad \text{, where}$$

$$\begin{aligned} G(Y,\phi) &= 1 \qquad \text{when } P(Y) \le \phi \\ &= 0 \qquad \text{otherwise, and} \end{aligned} \tag{8}$$

$P(Y)$ is the cumulative distribution function given by $P(Y) = \frac{1}{2\pi} \int_{-\infty}^{y} e^{-y^2/2}\, dy$.

2.3 FORMATION FACTOR AND PERMEABILITY

The permeability of the generated or reconstructed porous media can be calculated by solving the Stokes equations for low Reynolds number flow of an incompressible Newtonian fluid :

$$\nabla p = \mu \nabla^2 \mathbf{v} \tag{9}$$

and the continuity equation:

$$\nabla . \mathbf{v} = 0, \tag{10}$$

where **v**, p and μ are the velocity vector, pressure and viscosity of the fluid respectively. No slip boundary condition is applied on the solid wall, **v** = 0. If we take the divergence of the Stokes equation and then combine with the continuity equation, we get the Laplacian equation for the pressure :

$$\nabla^2 p = 0 \ , \tag{11}$$

with macroscopic pressure gradient across the system (∇p) is specified. First, Eq. (11) is solved to give the pressure field inside the porous medium. Then the velocity field is obtained by solving Eq. (9) from the known pressure field. The continuity equation must be satisfied for each voxel. It is found that the Eq. (11) must be solved very accurately in order to minimize the residual in continuity equation.

The pressure is calculated at the center of each voxel and the velocity is calculated at the edge of each voxel. Successive Over Relaxation (SOR) iterative method is used to solve the resulting finite difference scheme. The average flux (q_{av}) between the inlet face and the outlet face is calculated and is used to compute the permeability :

$$\frac{q_{av}}{A} = -\frac{k}{\mu}\nabla p, \tag{12}$$

where A is the area and k is the permeability. Assuming isotropic properties, we only compute the permeability in the x-direction.

The formation factor (F) is defined as the ratio of the conductance of the bulk fluid (σ_o) to the conductance of the porous media saturated with the fluid (σ), thus:

$$F = \frac{\sigma_o}{\sigma}. \tag{13}$$

F is always greater than one and it quantifies the effect of pore structure on the conductance of the porous medium. Formation Factor can also be calculated by solving the electrical conduction or thermal conduction problem that satisfies the Laplace's equation,

$$\nabla^2 U = 0, \tag{14}$$

where U is the local electric or thermal field, with no flux boundary condition across the solid surface,

$$\mathbf{n}.\nabla U = 0 \qquad \text{on } S \tag{15}$$

where $\mathbf{n}$ is a unit normal vector to S. An overall $\overline{\nabla U}$ across one axis of the system is imposed. Again, the average flux can be calculated after solving Eq. (14), and the effective conductivity is calculated by

$$q_{av} = \sigma\overline{\nabla U}. \tag{16}$$

Then the formation factor (F) is calculated from Eq. (13). The problem is solved by a second order finite difference scheme. The finite difference matrix system is solved by Successive Over Relaxation (SOR) method.

2.4 RESULTS

Five different spatially correlated porous media are generated with different correlation length and porosity. The dimensions of the porous media are 71^3 voxel^3 and the voxel size is 1 μm. The parameter λ is chosen between 0.1 and 0.5, and the porosity ranges from 0.2 to 0.35. Table 1 lists the specific surface area (S/V), the permeability and the formation factor of the generated media.

TABLE 1. Macroscopic properties of the reference structure.

λ	Porosity (ϕ)	S/V (μm^{-1})	Permeability (k) (mD)	Formation Factor
0.1	0.20	1.4223	15.72	66.60
0.1	0.30	1.1869	96.41	16.39
0.1	0.35	1.0836	166.80	10.58
0.3	0.35	1.8245	61.18	12.76
0.5	0.3	2.5599	16.09	28.61

Four different statistical function combinations are studied, and they are:

1. Two-point autocorrelation function only (S100).
2. Two-point autocorrelation function and chord length distribution function (S110).
3. Two-point autocorrelation function and lineal path function (S101).
4. Two-point autocorrelation function, chord length distribution function and lineal path function (S111).

The simulated annealing process can start from any initial structure, as long as the porosity matched the reference structure porosity. Random structure initial guess is generated by assigning random voxel as a pore space until the porosity matched the reference structure porosity.

2.4.1 Effect of random number seeds

Since simulated annealing is a stochastic process using several random number seeds, it is important to study the effect of those seeds on the computed macroscopic properties of these media. There are three random number seeds that are used in the process; the first one is used for random structure generation for the initial guess, the second one is used for choosing the voxel for spatial interchange in the annealing process and the last one is used in the Metropolis algorithm for spatial interchange acceptance probablity.

Fig. 1 shows the computed specific surface area (S/V) for the reconstructed structure. We perform five different realizations for each case. From Fig. 1., we observe that the random number seeds effect the specific surface area. The standard deviations are less than 0.2. This can be rationalized because the specific surface area for a 3D digitized medium is given as the initial slope of the two-point autocorrelation function,

$$\left.\frac{dS_2(r)}{dr}\right|_{r=0} = -\frac{S/V}{6}. \tag{17}$$

Therefore, if we match the two-point autocorrelation function accurately, the specific surface area will also be automatically match.

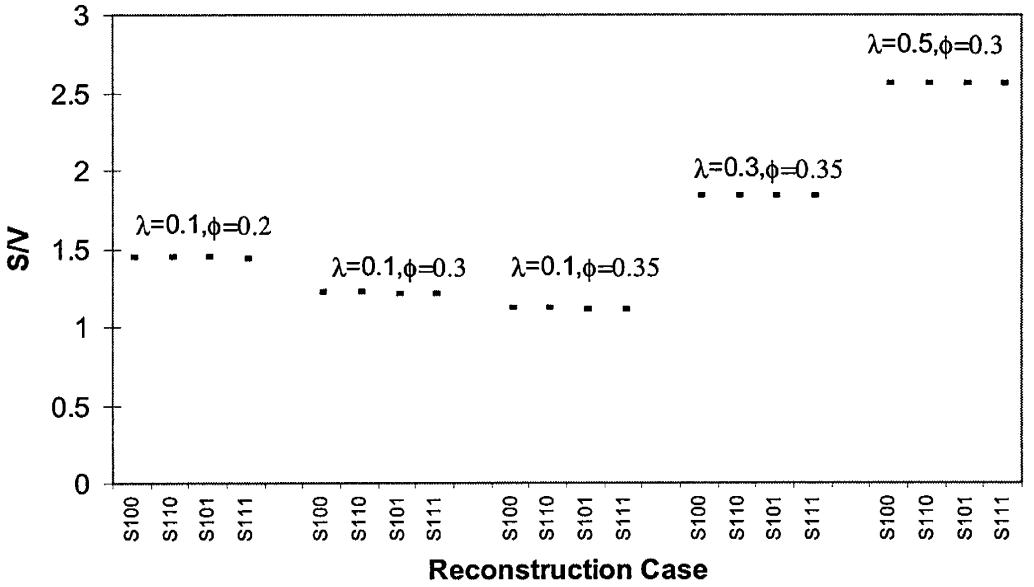

FIG. 1. Effect of random number seed on the specific surface area.

The effect of random seeds becomes more pronounced in the permeability calculations as shown in Fig 2. The uncertainty in the estimated permeability decreases with increasing λ (or decreasing correlation length). For a given λ, the standard deviation increases as the porosity decreases towards the percolation threshold. However, in most cases as the porosity decreases, the permeability is also decreases. So the absolute number of variations becomes smaller also. The structure with λ=0.1 and ϕ=0.2 serves as an example. Although the standard deviation is 18.5%, the permeability varies only from 8.34 mD to 13.17 mD. It should be noted that the reconstruction is based on realizations of the reference structure, so the appearance of the reconstructed structure will differ in each realizations. Thus, computed permeability can vary from realization to realization.

FIG. 2. Effect of random number seeds on permeability estimation.

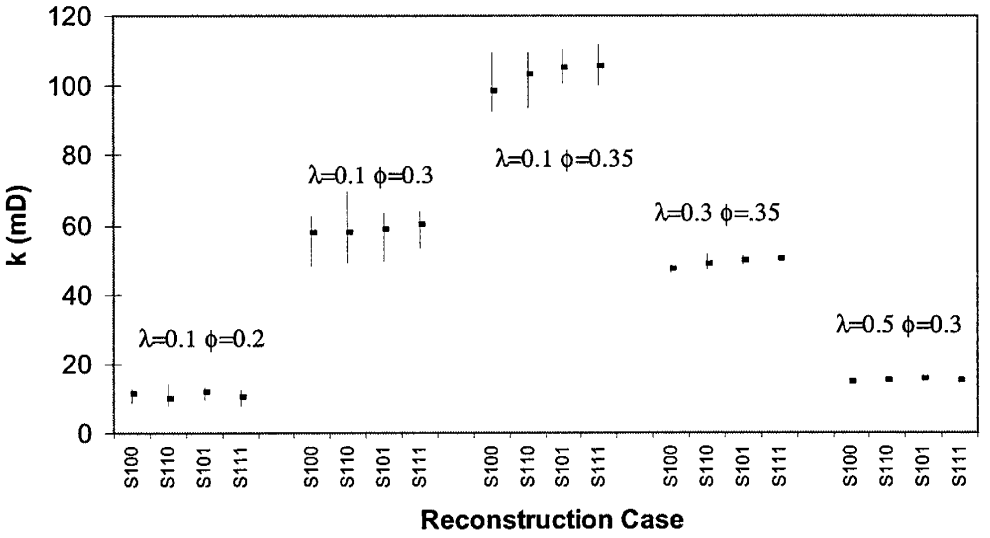

The variation of formation factor from different realizations is shown in Fig. 3. The calculated formation factor is not varying much with different seed numbers and the average standard deviation is 3.1%, except for the structure with λ=0.1 and ϕ=0.2. This structure has high formation factor which also means that the tortuosity is very high. Probably it becomes more difficult to reproduce a structure that has a very high tortuosity factor based only the statistical function that we choose.

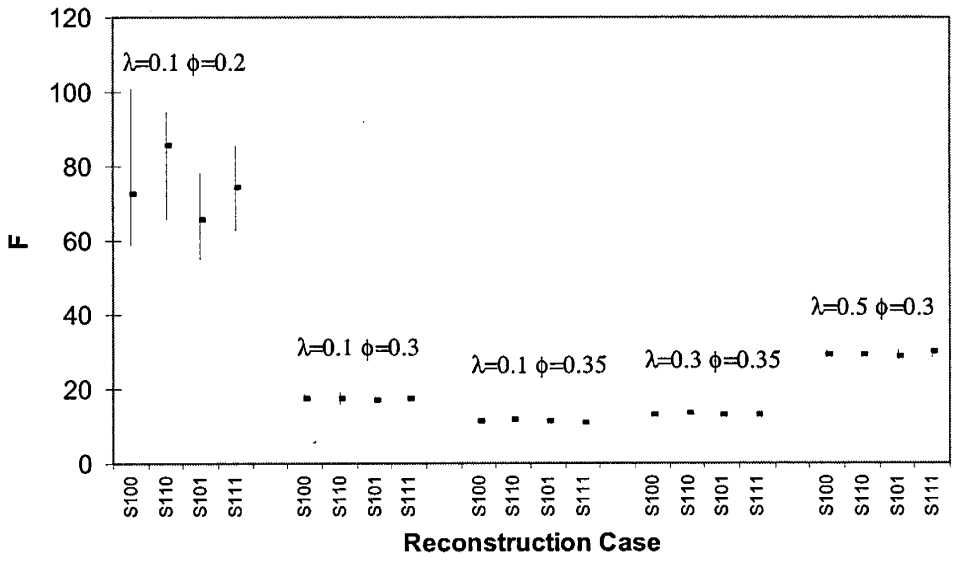

FIG. 3. Effect of random number seeds on formation factor estimation.

2.4.2 Reconstructed porous media from random intial guess

Fig. 4 shows the comparison between the specific surface area for the reconstructed structure and for the reference porous media. The value plotted is the average value of five different realizations. It is no surprise that they match very well since the specific surface area of a porous medium is related to the slope of the autocorrelation function.

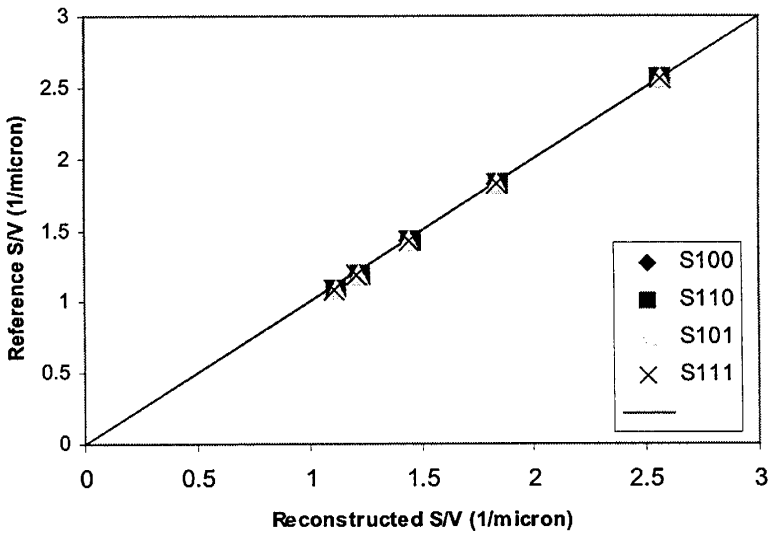

FIG. 4. Specific surface area comparison based on random initial guess.

Permeability comparison between the reconstructed structure and the reference structure is plotted as Fig. 5. In all cases, the reconstructed structures have a lower permeability compare to the reference structure. We also observe that the permeability deviation between the reconstructed structure and the reference structure increases at higher permeability value. They differ by a factor of 1.6. Surprisingly, adding more statistical functions to the annealing process does not improve the reconstruction result significantly. In most cases, S111 gives the highest permeability value. However, the difference is not to the extent that we can claim it is better than the others.

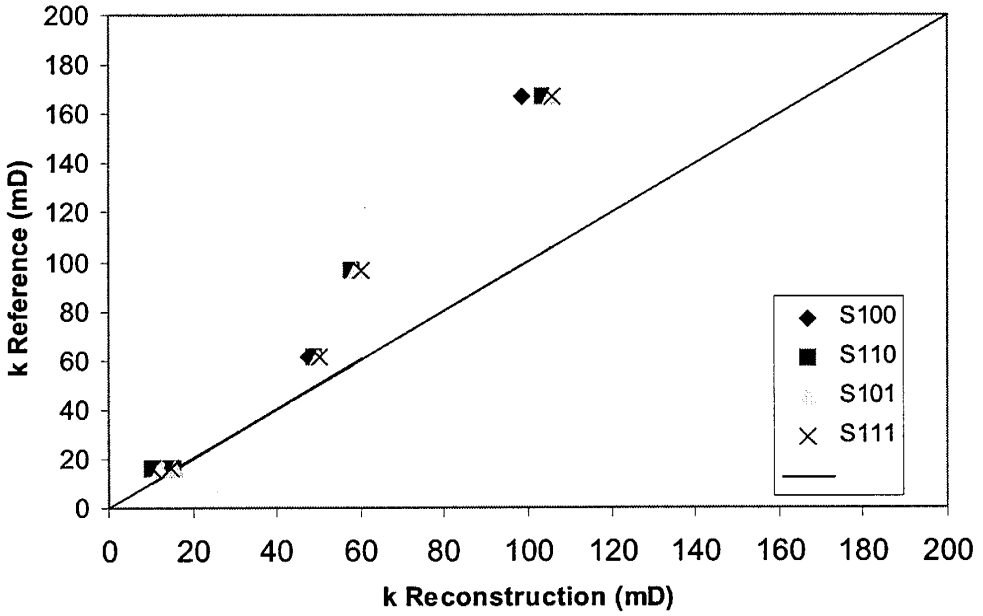

FIG. 5. Permeability comparison based on random initial guess.

As shown in Fig. 6, the formation factor of the reconstructed structure with any combination of statistical functions agrees very well with the value of the reference structure , except for the structure with λ=0.1 and ϕ=0.2 which has a very high formation factor. The S101 case has the worst formation factor compare to the other three cases. The S110 yields the best formation factor. However, at this point we cannot make any conclusion yet that S110 is the best statistical function combination for reconstruction. We need to do more reconstruction to check whether it behaves consistently.

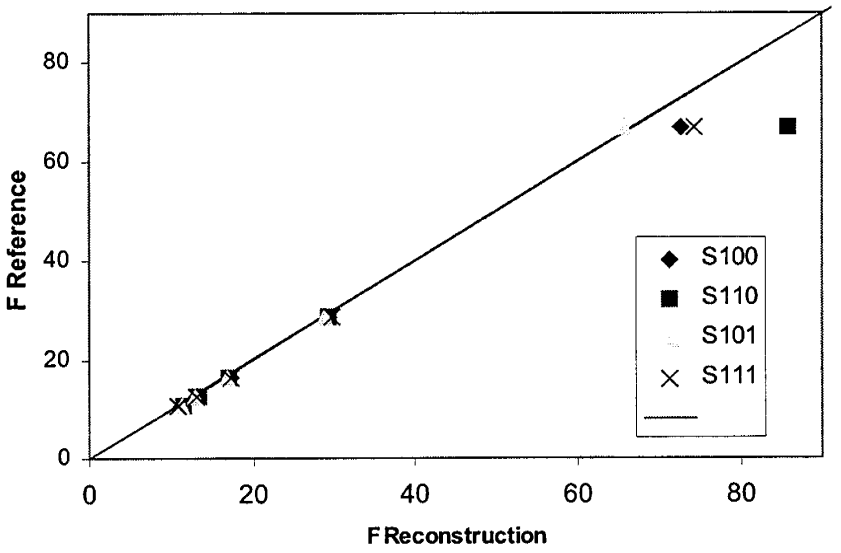

FIG. 6. Formation factor comparison based on random initial guess.

2.4.3 Conditional simulated annealing

We also examine the so called conditional simulated annealing. Here we take one slice or slices of real data (multiple thin section images) and put them directly into the reconstruction. The idea is to include as much as possible any available information and also to allow unusual features of the real image to be captured in our simulation that might be missed otherwise. The more slices we include in the reconstruction, the more the reconstructed image resembles the real data. Pore voxels in the remaining slices to are assigned such that the overall porosity matches the reference image porosity. This will be our initial guess for the simulated annealing process. The slices obtained from the real data are fixed during the simulated annealing and not allowed to be included in the phase interchange process.

In this study, we choose the first slice in the x-direction as our conditional slice. Fig. 7, Fig. 8, and Fig. 9 show the comparison of specific surface area, permeability, and the formation factor respectively. The specific surface area agrees very well with the reference structure value. The permeability and the formation factor exhibit the same behavior as the reconstructed structure from random guess. Again, the reconstructed porous media have lower permeability values than the reference value and also the deviation is larger at higher permeability. However, the difference factor is 1.4 and the difference is lower than in the random initial guess case. S111 gives the best permeability match.

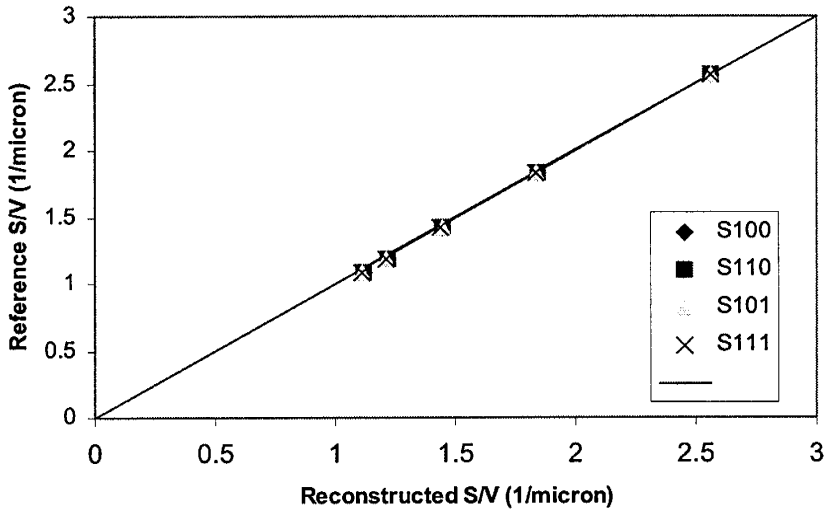

FIG. 7. Specific surface area comparison for conditional simulated annealing.

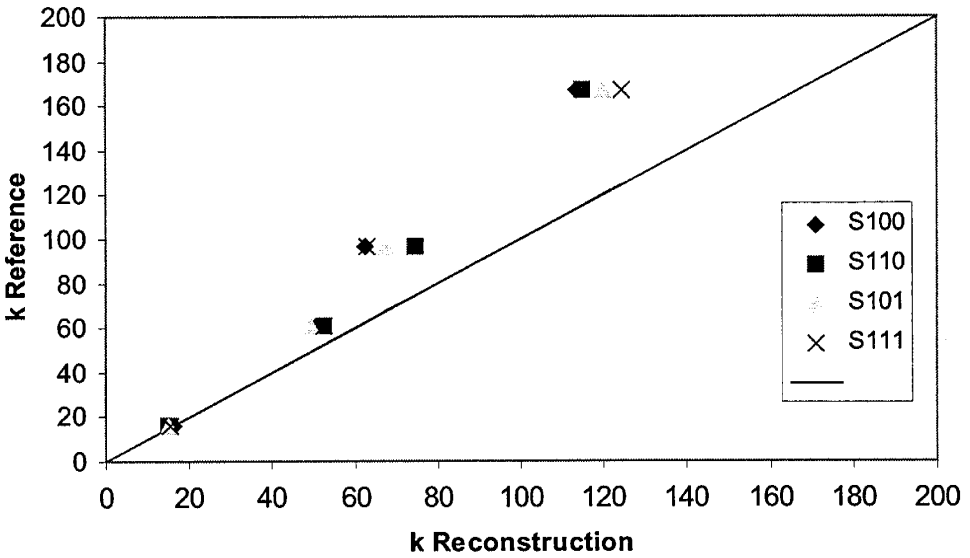

FIG. 8. Permeability comparison for conditional simulated annealing case.

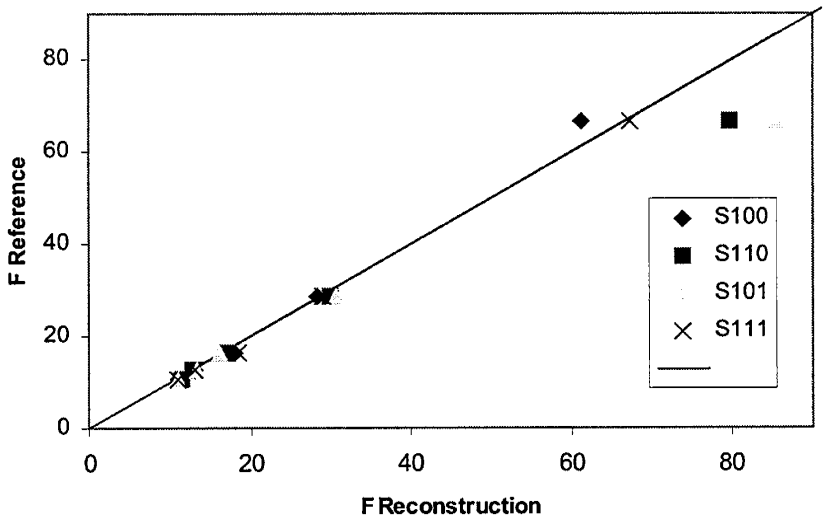

FIG. 9. Formation factor comparison for conditional simulated annealing case.

2.5 Conclusions

We have studied the sensitivity of the reconstruction process to the random seed numbers, the different combination of statistical functions and the initial guess for the reconstruction process. Specific surface area is clearly independent of the random seed numbers used, the combination of the statistical functions and the initial guess for the reconstruction process. As long as the two-point autocorrelation is matched, the specific surface area will be automatically matched also. The permeability is more sensitive to the random seed numbers at high permeability value and small λ (or equivalently larger correlation length). The conditional reconstruction yields the closest permeability value, though the improvement is not big. The formation factor is effected by the seed number only at high formation factor. The structure with λ=0.1 and ϕ=0.2 exhibits very high formation factor. The initial guess does not seem to effect the result very much. In many cases, S111 has the best formation factor and it never was the worst case.

The two-point autocorrelation function is the dominant statistical function in characterizing random porous media. The combination of two-point autocorrelation function, chord length distribution function and lineal path function yields the macroscopic properties closer to reference properties than other combinations. The improvement is not big, but the behavior is more consistent.

3. Corefloods and CT Imaging

The following carbonate core plugs were obtained from Shell:

	Depth, ft	Estimated ϕ, %	k, md
(i)	McElmo Dome		
	4060c	17.5	21.4
	4060d	17.5	15.6
(ii)	Yates		
	3956b	19.7	40.8
	3957c	19.4	26.5
(iii)	Chester		
	3672g	17.3	141
	3672h	17.8	115
(iv)	Wassan		
	3926a	21.4	88.6
	3926b	19.7	147
(v)	Cold Springs		
	3681d	14.4	65.3
	3681d	12.5	26.5

These cores are being analyzed for their petrophysical and NMR properties.

4. NMR Response Simulation Technique

The spin relaxation in NMR response of a fluid saturated porous medium, assuming no magnetic gradient, can be modeled by a reaction-diffusion material balance equation. The differential material balance equation is given as:

$$\frac{\partial[M]}{\partial t} = D\nabla^2[M] - \frac{[M]}{T_{2B}}, \tag{1}$$

with initial and boundary conditions:

$t = 0, \quad [M] = [M_0]$ and

$D\tilde{n}.\nabla\,[M] = \rho\,[M]$,

where $[M]$ is the magnetization per unit volume, and D is the diffusion coefficient. The magnetization profile can be obtained by solving the differential equation. The total magnetization ($M(t)$) at a given time can be calculated by integrating the magnetic concentration over the whole volume.

For simply-shaped pores, such as sphere, cylinder, cube and rectangular parallelepiped, an analytical solution can be derived for the decay of the total magnetization. Consider a spherical pore of radius, r. We can define a dimensionless group $L = \rho\, r / D$. The total magnetization is given by:

$$M(t) = M_0 \exp\left(-\frac{t}{T_{2B}}\right)\sum_{n=1}^{\infty}\frac{6L^2 \exp\left(-\frac{\beta_n^2 Dt}{r^2}\right)}{\beta_n^2(\beta_n^2 + L^2 - L)}, \tag{2}$$

where β_n is the root of $\beta_n \cot\beta_n + L - 1 = 0$. In the fast diffusion limit ($L \ll 1$), $\beta_1 \cong 3\,L$ and $\beta_{n+1} > \beta_n + \pi$. Thus, the magnetization decay follows a single exponential, i.e.,

$$M(t) = M_0 \exp^{-\frac{t}{T_2}} \tag{3}$$

where M_0 is the initial transverse magnetization and the decay rate T_2 is given by:

$$\frac{1}{T_2} = \frac{1}{T_{2B}} + \rho\frac{S}{V}. \tag{4}$$

S is the surface area of the pore and V is the pore volume. S/V for a sphere is equal to $3/r$. Eq. 4 is valid for other simply-shaped pores in the fast diffusion limit; a similar equation is also valid for T_1. For small pores or large surface relaxivity, the first term on the right hand side of Eq. 4 can be neglected, i.e.,

$$\frac{1}{T_2} = \rho\frac{S}{V}. \tag{5}$$

Note, in the slow diffusion limit ($L >> 1$), the single exponential approximation is no longer valid because β_1 is no longer close to $3L$. For operating conditions of NMR logging, the fast diffusion approximation is often valid.

A real porous medium comprises of pores of different sizes and shapes. Therefore, the magnetization decay cannot be represented by a single exponential term, even in the fast diffusion limit of each pore. A multi-exponential expression representing a distribution of T_2 constants is more suited for the magnetization decay of a real porous medium,

$$M(t) = M_0 \sum_{i=1}^{n} A_i e^{-\frac{t}{T_{2i}}} \tag{6}$$

where A_i is the volume fraction of pores of size i and T_{2i} is the T_2 time constant associated with pores of size i.

Many models have been developed to predict the transport properties from NMR relaxation time distribution (T_{1i} or T_{2i}). In early works, Seevers estimated permeability of a uniform sandpack based on porosity (ϕ) and T_1,

$$k \sim \phi T_1^2. \tag{7}$$

Kenyon et.al. found the form $\phi^4 T_{1s}$ was significantly better than that proposed by Seevers. T_{1s} is the characteristic decay time from stretched exponential fitting given as:

$$M(t) = M_0 \exp(-(\frac{t}{T_{1s}})^{\alpha}). \tag{8}$$

More recent work claimed that sandstone permeability (in mD) can be better predicted by using T_2 instead of T_1 without significant change in exponents. For example, an often used permeability correlaton is

$$k = 4.6\, \phi^4\, (T_{2lm})^2 \tag{9}$$

where T_{2lm} (in ms) is the logarithmic mean of T_2 distribution. The logarithmic mean is defined as:

$$T_{i,lm} = \exp\left(\frac{\sum A_j \log(T_i)_j}{\sum A_j} \right) \tag{10}$$

Many variations of permeability correlations similar to Eqs. (7) and (9) with different exponents are reviewed in Kubica (1995). The rationalization for such correlation comes from the following. T_{2lm} is related (approximately) to the specific surface area, S/V, of the porous medium because T_2 of a pore is related to its S/V through Eq. (5). A common but not very mechanistic model for permeability is the Carman-Kozeny model, which states

$$k \sim \frac{\phi}{\tau} \left(\frac{S}{V} \right)^{-2}, \tag{11}$$

where τ is the tortuosity of the porous medium. Tortuosity is defined as the square of the ratio of the effective average path length L' through the porous medium to the shortest distance L measured along the direction of macroscopic flow , i.e.,

$$\tau = \left(\frac{L'}{L} \right)^2. \tag{12}$$

The correlation from Eq. (9) can be rationalized from Eq. (11) if $\tau \sim \phi^3$. Mechanistically, there are three issues associated with such correlations.

First, the NMR permeability correlations shown above do not include the surface relaxivity term explicitly. From Eq. (5), it is clear that the surface relaxivity will change the measured T_1 or T_2 value. If the surface relaxivity data is available for the corresponding porous media, it should be included in the permeability correlation explicitly to give more accurate estimation. Surface relaxivity can be measured by comparing *S/V* from NMR measurement with *S/V* from nitrogen BET adsorption, for example. Alternatively, it also can be obtained by comparing pore size distribution from image analysis of thin sections.

Second, the correlations assume that the tortuosity is proportional to ϕ^3. Tortuosity is not a function of porosity alone. It is related to the formation factor, F defined as

$$F = \tau/\phi. \tag{13}$$

The formation factor is defined as the ratio of conductance of bulk fluid (σ_0) to the conductance of the porous media saturated with the fluid (σ). Formation factor of a medium can be obtained from resistivity logs and is usually available for most oil wells. By including the known value of F or equivalently τ, one can improve the NMR permeability correlation. Difficulties may arise from the fact that the rock is not fully saturated with brine, and F cannot be directly estimated from the resistivity logs.

Third, the specific area (*S/V*) one estimates by NMR is the inverse of a typical pore body size for porous media composed of fairly smooth grains. Pore throats contribute little to *S/V*. However, it is the throats, the narrow channels between the pore bodies, that are supposed to control the hydrodynamic pressure drop and hence the permeability. Starting from percolation concepts, Katz and Thompson have related the permeability of a porous medium to a length scale l_c,i.e.,

$$k = \frac{1}{226}\frac{l_c^2}{F} \tag{14}$$

where l_c is the size of the smallest throat invaded by a non-wetting phase at the percolation threshold of the porous medium. It can be estimated easily from a mercury capillary pressure curve of the medium. This would tend to imply that the above NMR permeability correlations could work only if the pore body radii and throat radii are correlated.

Another widely used permeability model is in the form $\phi^{4.4} / S_{wi}^2$, where S_{wi} is irreducible water saturation. Timur showed that the volume of water that cannot be removed from a sample by centrifuging (at a particular speed) is a good basis for estimating permeability. Coates developed the Free Fluid Model which estimates the permeability based on the Free Fluid Index (FFI) (or free moving water in the porous media) and the Bulk Volume Irreducible (BVI) (or the bound water in the porous media),

$$k = 10^4 \phi^4 \left(\frac{FFI}{BVI}\right)^2 \tag{15}$$

and

$$FFI + BVI = \phi. \tag{16}$$

Given a T_2 distribution, $T_{2cutoff}$ divides the pore volumes into free fluid and bound fluid. In the absence of the laboratory data, 33 ms and 92 ms are the commonly used $T_{2cutoff}$ values for sandstones and carbonates, respectively. These correlations also suffer from the same criticisms as does the SDR model.

The objective of this work is to demonstrate the above three mechanistic issues of NMR permeability correlations by direct simulation. In this paper, we generate spatially-correlated porous media with a given porosity and a two-point correlation function and compute their permeability by the lattice Boltzmann method. The NMR relaxation response in these media is simulated by using a random walk technique. The simulation provides the magnetization amplitude as a function of time. T_2 distribution is then calculated by a multi-exponential fitting. We also calculate the formation factor by a finite difference method. Our methodology is described in the next four sections. We compare the specific surface area estimated from simulated NMR response with the actual ones. The permeability estimated from the NMR correlations based on the simulated NMR response is compared with the permeability calculated by a lattice Boltzmann algorithm in section 6. Important conclusions are summarized in the last section.

4.1 Generation of Correlated Porous Media

Generation of correlated porous media can be regarded as an application of the recently developed reconstruction methods. This reconstruction is a typical inverse problem, where a porous medium is generated given some of its low order statistical properties such as porosity and two-point pore-pore correlation function.

Let P be the pore space in a porous medium described by the characteristic function

$$Z_P = \begin{cases} 1, & x \in P \\ 0, & elsewhere \end{cases} \tag{17}$$

The porosity (ϕ) is given by $\phi = \langle Z_P \rangle$ and the normalized two-point pore-pore correlation function is given by

$$C_{2Z}(x) = \frac{\langle [Z_P(y) - \phi][Z_P(y+x) - \phi] \rangle}{\phi - \phi^2} \tag{18}$$

Note that $\langle Z_P^n(x) \rangle = \langle Z_P(x) \rangle = \phi$ for every n>0. If the material is isotropic and homogeneous, $C_{2Z}(x)$ is a function of |x| alone and a generic cross-section of the material is representative of the entire three-dimensional (3D) structure.

A correlated field $\{Y(\underline{x}, \lambda)\}$ can be generated from a Gaussian uncorrelated process $\xi_\lambda(\underline{x})$ with zero mean and unit variance by convoluting with an exponential kernel:

$$Y(\underline{x},\lambda)=\left(\frac{4\lambda}{\pi}\right)^{d/4}\int_{E^d}\exp\left(-2\lambda u^2\right)\xi_\lambda(\underline{u}+\underline{x})d\underline{u} \tag{19}$$

where $E^d=\{\underline{x}\,|-\infty<x_i<\infty\ (i=1,...,d)\}$ is the Euclidean d-dimensional space. The correlated field $\{Y(\underline{x},\lambda)\}$ is still Gaussian with zero mean and unit variance but exhibits an exponential two-point correlation function:

$$C_{2Y}(\underline{x},\lambda)=\exp\left(-\lambda x^2\right) \tag{20}$$

A unique dimensionless correlation length $\frac{L_c}{a}=\frac{2}{a\sqrt{\lambda}}$ characterizes these exponentially random correlations, where a is the voxel size of the generated medium. It should be noted that the correlation length L_c is inversely proportional to the square root of λ. Hereafter, this relationship between L_c and λ will be used without restating this fact.

This Gaussian correlated field $\{Y(\underline{x},\lambda)\}$ can be transformed into a binary correlated field $Z(\underline{x},\lambda)$ which represents a porous medium of porosity ε by the following nonlinear filter,

$Z=G(Y,\varepsilon)$, where

$$\begin{aligned} G(Y,\varepsilon)&=1 \qquad \text{when } P(Y)\le\varepsilon \\ &=0 \qquad \text{otherwise, and} \end{aligned} \tag{21}$$

$P(Y)$ is the cumulative distribution function given by $P(Y)=\frac{1}{2\pi}\int_{-\infty}^{y}e^{-y^2/2}\,dy$.

4.2 Lattice Boltzmann Algorithm

In the lattice Boltzmann method, space is divided into a regular lattice and real numbers at each lattice site represent the single-particle distribution function at that site. More specifically, the single particle distribution function at a single site in the lattice is represented by a set of real numbers, $n_i(\boldsymbol{x},t)$, the expected number of particles at lattice site $\boldsymbol{x}$ and time t moving along the lattice vector i, where each value of the index i specifies one of the allowed directions of motion. At every node $\boldsymbol{x}$, the macroscopic density and momentum are defined as

$$\rho_f(\underline{x},t)=\sum_{i=1}^{q}n_i, \quad \text{and} \tag{22}$$

$$\rho_f \underline{u}(\underline{x},t) = \sum_{i=1}^{q} n_i \underline{e}_i. \tag{23}$$

The discrete Boltzmann equation governs the local evolution of the population on the links connecting adjacent sites, i.e.,

$$n_i(\underline{x}+\underline{e}_i, t+1) = n_i(\underline{x},t) + \Omega_i(\underline{x},t), \qquad i = 1,...,q \tag{24}$$

where q is the total number of allowed directions of motion.

The collision operator Ω_i is given by the Bhatnagar-Gross-Krook (BGK) approximation,

$$\Omega_i = -\beta^{-1}(n_i - n_i^{EQ}) \tag{25}$$

which drives each population toward its equilibrium value n_i^{EQ} at a rate determined by the relaxation time β. The equilibrium population n_i^{EQ} depends on the local values of ρ_f and u, and it is formulated specifically to recover the low Mach-number limit of the Navier-Stokes equations with Galilean invariance.

The pressure in the fluid is governed by an equation of state:

$$p = c_s^2 \rho_f \tag{26}$$

where c_s is the speed of sound. The kinematic shear and bulk viscosities are, respectively,

$$\nu = \frac{(2\tau - 1)}{6}, \quad \kappa = \frac{7(2\tau - 1)}{6} \tag{27}$$

and the dynamic viscosities are given by $\mu = \rho_f \nu$ and $\mu_v = \rho_f \kappa$.

Spatial extrapolation technique is used to specify the inlet and outlet pressures for the flow field. For most of the simulations in this study, the flow was started from a zero velocity throughout the computational domain. Since we are interested in the steady state flow profile within the porous medium, the use of any initial condition is justified. A more detailed description of the lattice Boltzmann method used in this study can be found in Singh & Mohanty (2000) and the references therein.

4.3 NMR Response Simulation Method

NMR response simulation is carried out based on a random walk technique . The algorithm is based on simulating the Brownian motion of a diffusing particle (called walkers or random walkers). Initially, the walkers are placed randomly in the pore space. At each time step, the walkers are moved from their initial position to a new position on

the surface of a sphere with radius ε centered on the initial position. The time step is given by

$$dt = \frac{\varepsilon^2}{6D} \tag{28}$$

where D is the diffusion coefficient of the bulk fluid. The new position is given by

$$x_2 = x_1 + \varepsilon \sin\theta \cos\varphi \tag{29}$$

$$y_2 = y_1 + \varepsilon \sin\theta \sin\varphi \tag{30}$$

$$z_2 = z_1 + \varepsilon \cos\theta \tag{31}$$

The angles θ and φ are randomly selected.

For simulation of a big system, use of a small fixed step ε may not be computationally effective. Zheng and Chiew used an optimized step size at each time step. At each time step, the largest possible imaginary sphere within the pore space centered at the walker position is constructed without overlapping any solid surface. Then the walker is moved to a randomly chosen position on the imaginary sphere surface. The time is updated by the first passage time probability distribution:

$$P(t:r) = 1 + 2\sum_{m=1}^{\infty}(-1)^m \exp\left(-\frac{Dm^2\pi^2 t}{r^2}\right). \tag{32}$$

P(t:r) is the cumulative distribution function associated with the time taken t for the random walker to move to a distance r.

However, for a real porous medium, the construction of the largest possible sphere within a pore space that does not overlap any solid surface can be very computationally intensive, especially if the construction is performed at each time step for each walker. In this study, we use a semi-fixed step method. We choose two fixed step sizes, one is small (ε) and the other step size is large and is of the order of the pixel size. If all 26 neighbors of a pore pixel belong to the pore space, then the large step size is selected and the time is updated by first passage time probability distribution (Eq. 32). Otherwise, a small step size is selected and the time is updated by Eq. (28).

If the walker goes into the solid, it is killed with a finite killing probability. The killing probability γ is related to the surface relaxivity ρ as

$$\gamma = \frac{2\rho\varepsilon}{3D}. \tag{33}$$

If the walker survives, the position of the walker is not changed and time is advanced by the time step given in Eq. (28). By repeating this procedure for a large number of walkers, the life time distribution of random walkers is generated. This life time distribution is used to calculate the magnetization amplitude as a function of time. The T_2 distribution is obtained by fitting a multi-exponential model given in Eq. (6) to the magnetization amplitude by using a nonnegative-least-square-technique (NNLS) with regularization.

4.4 Formation Factor

Formation factor can be calculated by solving the electrical conduction or thermal conduction problem that satisfies the Laplace's equation ,

$$\nabla^2 U = 0, \tag{34}$$

where U is the local electric or thermal field, with no flux boundary condition across the solid surface,

$$\mathbf{n}.\nabla U = 0 \qquad \text{on } S, \tag{35}$$

where $\mathbf{n}$ is a unit normal vector to S. An overall $\overline{\nabla U}$ across one axis of the system is imposed. Eq. (34) is solved by a second order finite difference scheme. The finite difference matrix system is solved by Successive Over Relaxation (SOR) method. To improve accuracy, the problem is solved twice, once each with mesh size of h and $h/2$. Then the result is extrapolated using Richardson's extrapolation to reduce the error in the extrapolated solution U^* to $O(h^4)$:

$$U^* = \frac{4U\left(\frac{h}{2}\right) - U(h)}{3} + O(h^4). \tag{36}$$

The total flux q on across any slice is obtained by summing the local contributions. The effective conductivity (σ) of the porous medium is calculated as

$$q = \sigma \overline{\nabla U}. \tag{37}$$

F can be calculated from σ by

$$F = \frac{\sigma_o}{\sigma} \tag{38}$$

4.5 Results

In this study, six different spatially correlated porous media are generated with different correlation length and porosity. The dimensions of the porous media are 71^3 voxels and each voxel is assumed to be 1 μm. The parameter λ is chosen between 0.1 and 0.5, and the porosity ranges from 0.3 to 0.4. The percolation threshold for correlated simple cubic lattices would be lower than 0.3. We have considered correlated porous structures with porosity ≥ 0.3. Fig. 1 and 2 show the generated porous media for different values of porosity and correlation length. The permeabilities of the generated porous media are measured by the lattice Boltzmann method. Table 1 lists the permeability which ranges from 19.8 to 164.5 mD (1 mD ~ 10^{-15} m^2).

Table 1. **Permeability of the exponentially correlated 3D porous media with different λ and different porosities.**

λ	Porosity	Permeability (mD)
0.1	0.3	90.5
0.1	0.35	164.5
0.3	0.35	73.0
0.3	0.4	115.9
0.4	0.35	56.8
0.5	0.3	19.8

For reasons of computation time and accuracy, it is important to use an optimum number of walkers to simulate the NMR response. For a simple and symmetric geometry, such as a spherical pore or cube, only a small number of walkers is sufficient. For example, in a single isolated spherical pore one thousand walkers are enough to give a reasonably accurate result. However, for more complex systems, a larger number of walkers is required. For the NMR simulation in the generated porous media, the number of walkers used is arbitrarily chosen to be slightly higher than the number of pore pixels. The NMR response is recalculated using twice the number of walkers. The calculated T_{2lm} did not show a significant variation. So, for all the simulations, we have chosen to use the total number of walkers slightly larger than the number of pore pixels in the porous medium. The idea being that each pore pixel should get at least one walker in a statistical sense. With a surface relaxivity (ρ) of 10 $\mu m\ s^{-1}$ and the number of walkers as determined above, the simulation takes about three days to finish on a time-shared 166 MHz DEC Alpha workstation. We have also developed a parallel version of the random walk code. This enables us to finish the same simulation in as low as an hour of real-time computation depending on the number of processors used.

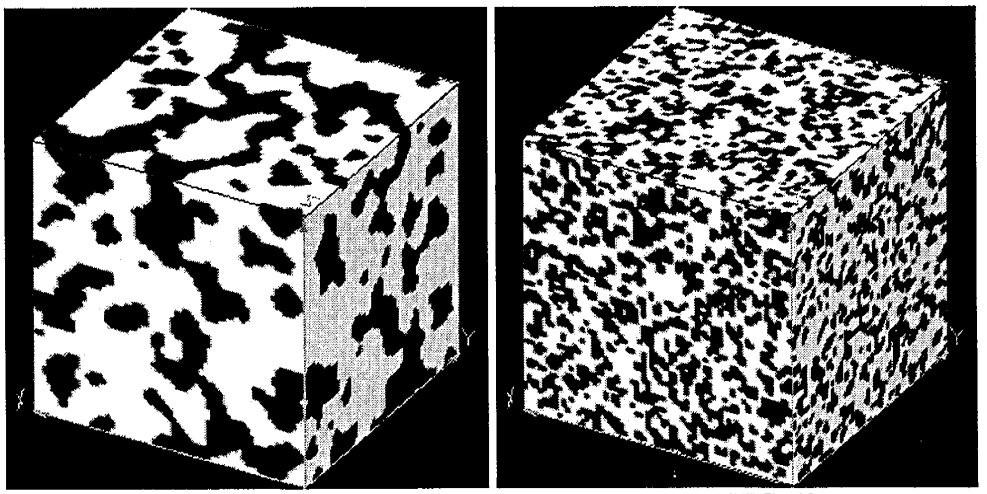

FIG. 1a FIG. 1b

FIG. 1. The effect of correlation length on pore space structre. (a) $\lambda = 0.05$, $\phi = 0.4$ (b) $\lambda = 0.5$, $\phi = 0.4$

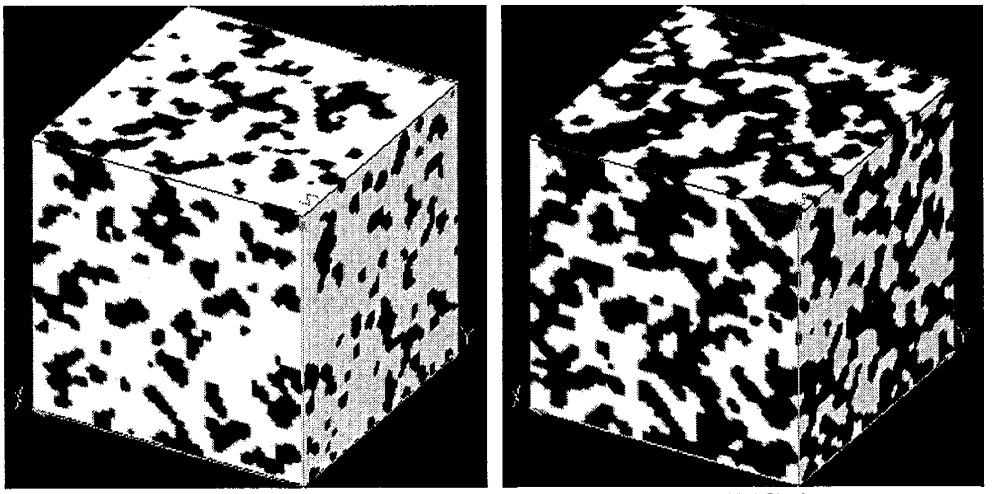

FIG. 2a FIG. 2b

FIG. 2. The effect of porosity on pore space structure. (a) $\lambda = 0.1$, $\phi = 0.3$ (b) $\lambda = 0.1$, $\phi = 0.5$

The T_2 value for the bulk liquid is chosen as 2,800 ms. The typical ρ value for sandstone is about 20 μm s^{-1}. A study by Huang for a different type of sandstone yields ρ for T_2 in the range 21.2 ± 6.3 μm s^{-1}. Therefore in this study, surface relaxivity (ρ) is varied from 10 to 30 μm s^{-1}. The simulation is stopped if time is greater than five times the expected longest T_2 component. We set the longest T_2 component as 1000 ms, and we find that the actual longest T_2 component for all the simulations is much smaller than 1000 ms.

4.5.1. T_2 distribution

Fig. 3 shows the T_2 distribution from the NMR simulation for the six different generated porous media at a ρ of 20 μm s^{-1}. The T_2 distribution provides information about the pore size distribution, based on Eq. (5). The T_2 distribution and thus the pore size distribution appear narrow, unimodal and approximately log normal. As λ increases, the correlation length decreases and the T_2 distribution shifts to the shorter relaxation time implying that pores become smaller. For a given λ, as the porosity increases, the T_2 distribution is shifted to longer relaxation time implying that the pores are larger.

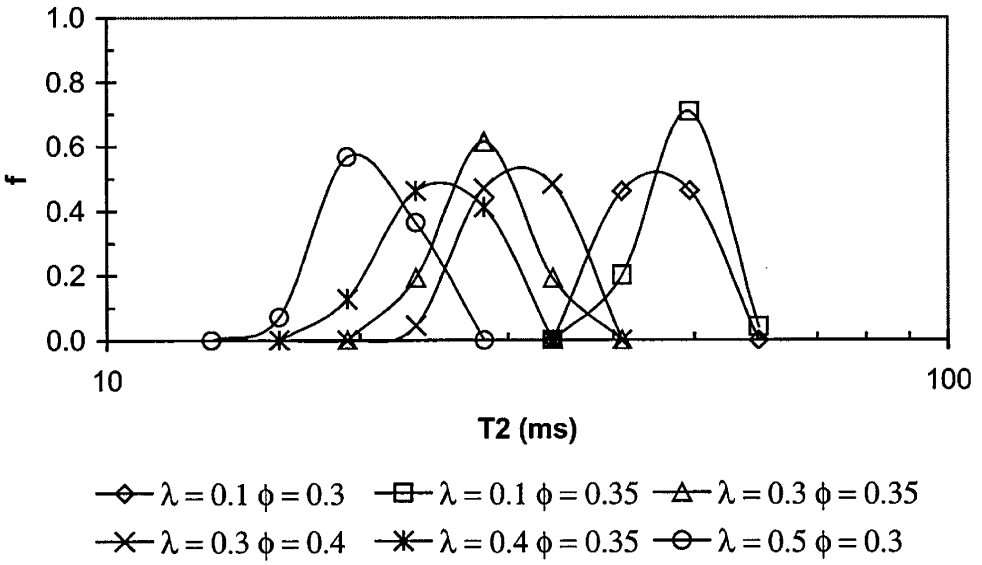

FIG. 3. T_2 distribution for different generated structures with $\rho = 20$ microns/second.

4.5.2. Specific Surface Area

The specific surface area of a medium, *S/V* is often calculated from the T_{2lm} value using Eq. (5). Note that Eq. (5) is exact for a single pore, not for a porous medium. This methodology, however, can be tested by simulation. Fig. 4 shows the comparison of the calculated *S/V* from NMR simulation with the actual *S/V* for the porous media generated in this study. The calculated *S/V* from NMR agrees approximately with the actual *S/V*. If the pore size distribution is bimodal or very different from log-normal, then the T_{2lm} may not be the best average to be used for specific area estimation.

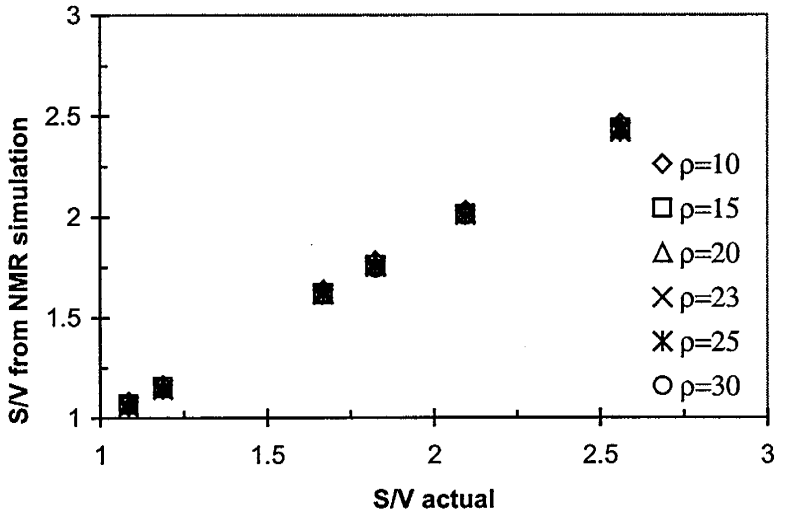

FIG. 4. Comparison of the *S/V* values calculated from NMR response simulation and the actual values of *S/V*.

4.5.3 Effect of Surface Relaxivity on T_2 Distribution and Its Log-mean

The effect of ρ on T_2 distribution is plotted in Fig. 5 for structure with λ equals to 0.1 and porosity equal to 0.3. As ρ decreases, the ability of the pore wall to relax the magnetization also decreases, hence the magnetization relaxes slowly and the T_2 distribution shifts to longer relaxation time. Fig. 6 shows the relationship between T_{2lm} and $1/\rho$ for each generated structure. The plot shows that T_{2lm} is inversely proportional to ρ, which implies $T_{2b} >> T_2$.

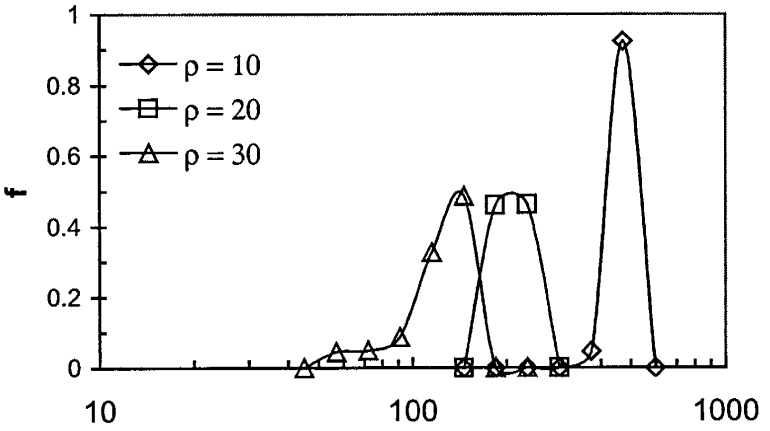

FIG. 5. Effect of ρ on the T_2 distribution for generated structure with λ = 0.1 and porosity = 0.3.

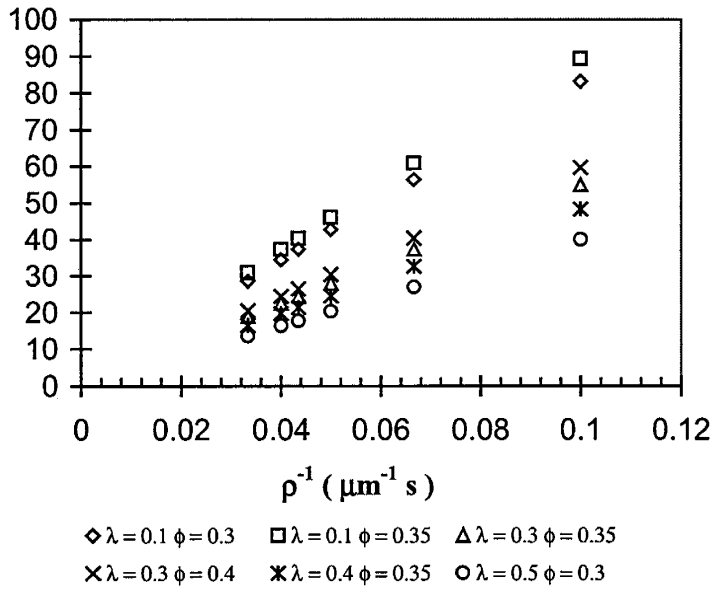

FIG. 6. The effect of ρ on $T_{2logmean}$ for various generated

Eq. (9) cannot be expected to be valid for porous media with a different surface relaxivity. Using the data in Fig. 6, however, we can include surface relaxivity ρ in the permeability model based on porosity and T_{2lm} and generalize Eq. (9) to be:

$$k = c_1 \rho^2 \phi^4 (T_{2\,lm})^2 \tag{39}$$

where c_1 is a new constant. To determine c_1, we plot k versus $[\rho^2 \phi^4 (T_{2\,lm})^2]$ for various values of ρ and calculate the slope from linear regression. The plot is given in Fig. 7. The unknown parameter c_1 is estimated to be 0.0139 with R^2 = 0.9562. For these exponentially correlated porous media, we obtained the following relationship:

$$k = 0.0139 \rho^2 \phi^4 (T_{2\,lm})^2 \tag{40}$$

where ρ is in μm s^{-1}, T_{2lm} is in ms and k is in mD.

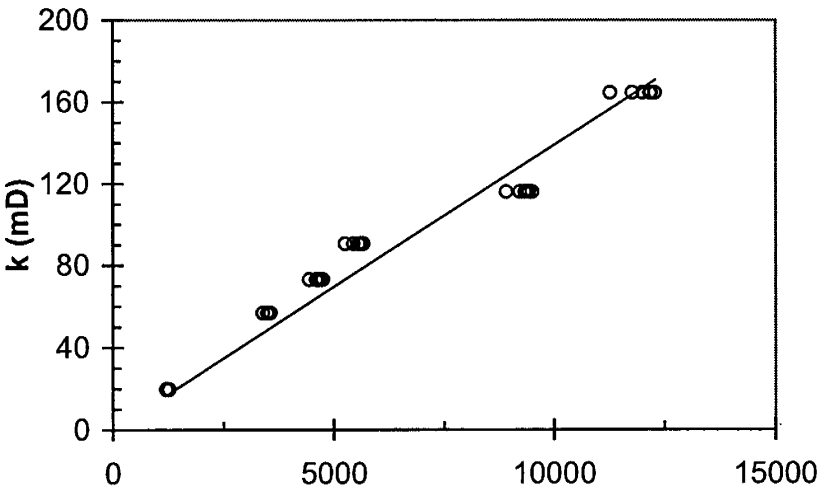

FIG. 7. Permeability computed from lattice Bolztmann algorithm vs ($\rho^2\ \phi^4\ (\ T_{2\ lm}\ )^2$). The calculated slope from straight line fitting is 0.0139 with $R^2 = 0.9562$.

4.5.4. Predictive Model with Formation Factor, Surface Relaxivity and T_{2lm}

Formation factor, F is calculated numerically as described in section 5. Fig. 8 shows that F is not a function of only porosity. If we replace the porosity term in Eq. (39) with the inverse of the formation factor, the permeability correlation becomes

$$k = c_2\, \rho^2\, (T_{2lm})^2 / F \tag{41}$$

where c_2 is the constant to be determined. Fig. 9 shows the plot of k versus $[\rho^2\ (T_{2lm})^2 / F]$ for all the simulated media in this study. c_2 is calculated from the slope of the best fit straight line. For the exponentially correlated 3D porous media, the c_2 is found to be 0.002 with $R^2 = 0.9107$ where the unit of ρ is in $\mu m\ s^{-1}$ and T_{2lm} is in ms. Intuitively, this is a better model than SDR model since tortuosity information is included as F in this model, which can be determined from electrical logs of the same formation.

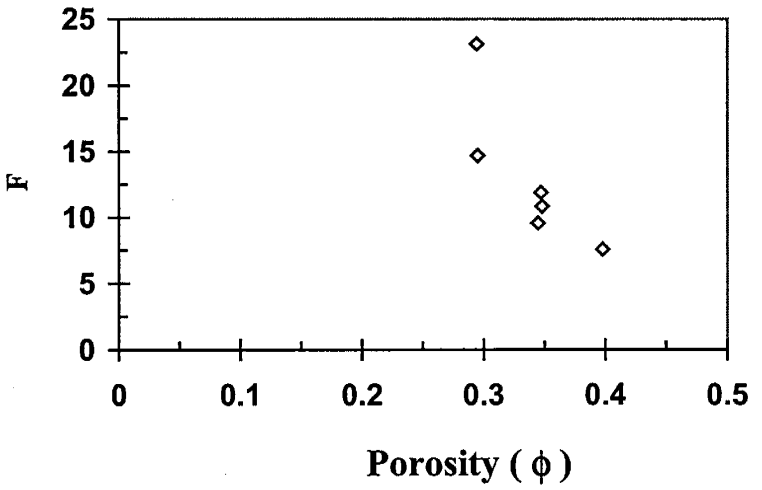

FIG. 8. Formation Factor (F) of the generated porous media.

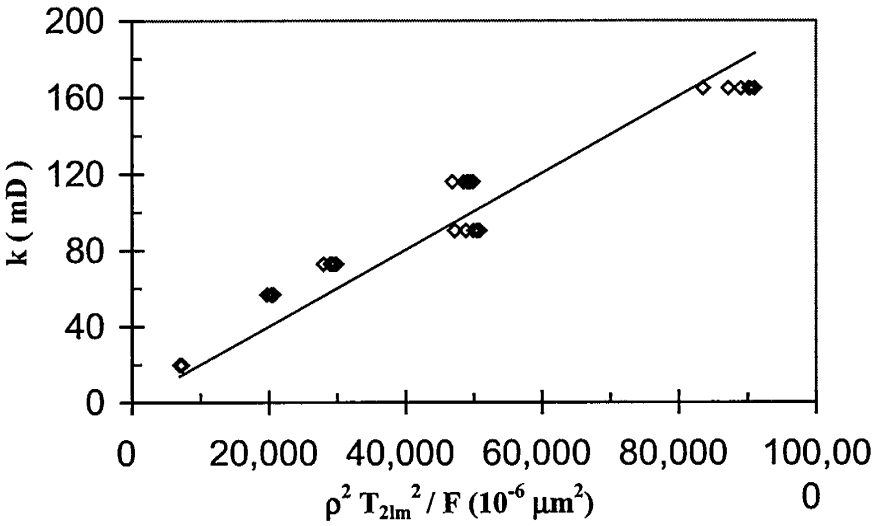

FIG. 9. Permeability computed from lattice Bolztmann algorithm vs $(\rho^2 (T_{2lm})^2 / F)$. The calculated slope from straight line fitting is 0.002 with $R^2 = 0.9107$.

4.5.5. Correlation between Pore Body and Throat Radii

The porous media generated in this study are exponentially correlated. Thus, characteristic pore body and throat radii are proportional to each other. The permeability correlations based on characteristic pore body radii, or equivalently *V/S* work even though pore throats control permeability. Such correlations should not work in porous media where pore throats and body radii are not correlated. This is demonstrated with the following example.

A periodic porous medium is constructed (conceptually) where all bodies are cubes of sides *a* attached to six throats in a simple cubic array (refer to Fig. 10). All the throats are of length *l* and of square cross-section of sides *b*. Parameters *a* and *l* are kept at constant values, 40 μm and 30 μm, respectively. The throat size *b* is varied from 4 to 10 μm. The porosity and T_{2lm} are plotted in Fig. 11, and the permeability calculated from lattice Boltzman and from Eq. (40) are plotted in Fig. 12. As the throat size increases, the permeability goes up, as it should, but the T_{2lm} actually decreases. T_{2lm} decreases because the surface area hardly changes, but the pore volume increases. Thus the permeability does not increase as T_{2lm}^2, as would be dictated in correlations like Eq. (9). The permeability increase (between pore throat of size 4 μm and 10 μm) estimated by this correlation is a factor of less than 2, whereas the actual permeability increases by a factor close to 10. A necessary condition for the NMR permeability correlations based on T2 is the correlation between pore body and throat radii.

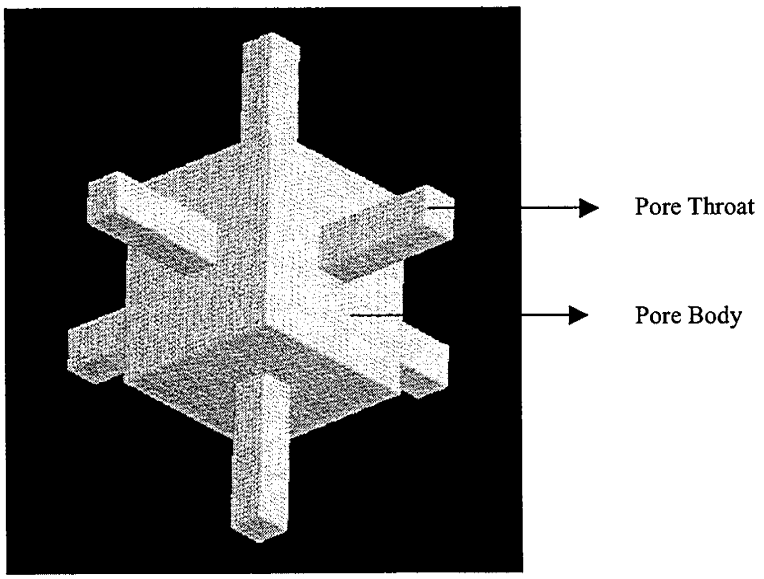

FIG. 10. Pore Throat – Pore Body Model.

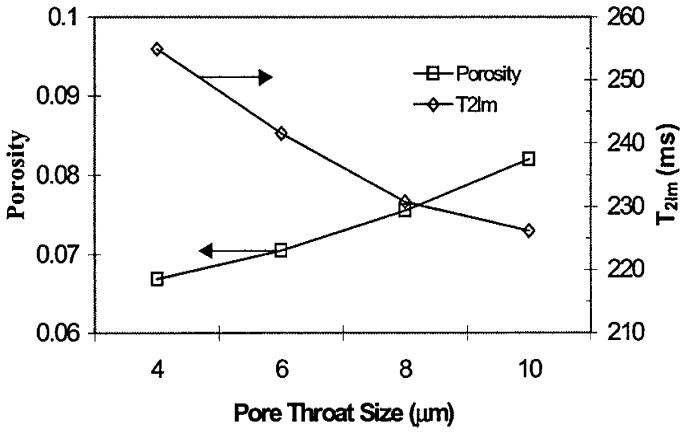

FIG. 11. Porosity and $T2_{lm}$ of periodic porous medium represented by one body six throat model.

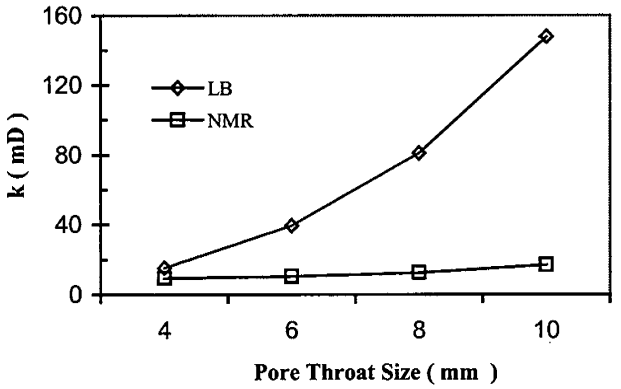

FIG. 12. Comparison of permeability calculated from lattice Boltzmann algorithm and from Eq. (42) for periodic medium represented by one body six throat model.

4.5.6. Effect of ρ on $T_{2cutoff}$ in Free Fluid Model

We use Coates' Free Fluid Model to calculate the $T_{2cutoff}$ value for the six generated porous media. Using the permeability calculated by the Lattice Boltzmann algorithm BVI is computed from Eq. (15). $T_{2cutoff}$ is calculated from the cumulative T_2 distribution given the BVI value. Fig. 13 shows the plot of $T_{2cutoff}$ versus $1/\rho$ for the six generated porous media. The plot shows that $T_{2cutoff}$ is also inversely proportional to ρ. This is expected since T_{2lm} is inversely proportional to ρ as has been discussed in section 6.3. It also shows that ($\rho\ T_{2cutoff}$) is not a constant. This indicates that this correlation would not work with a fixed $T_{2cutoff}$ even for constant surface relaxivity (e.g. 33 ms for sandstones and 92 ms for carbonates).

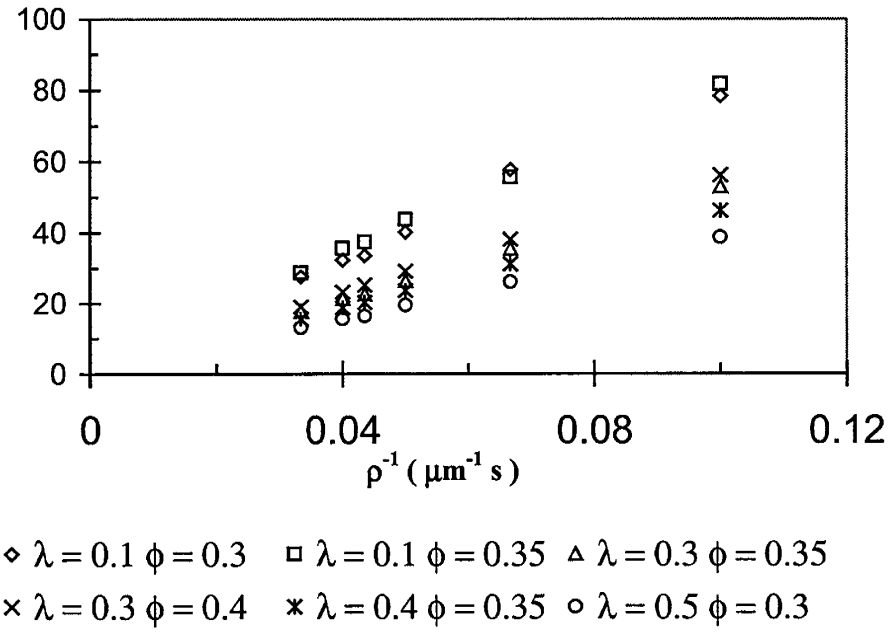

FIG. 13. Effect of ρ on $T_{2cutoff}$ for calculating BVI for various generated structures.

4.6 Conclusions

Under what conditions do NMR permeability correlations work for sandstones? Three conditions should be met. The surface relaxivity should not vary between the sandstones. The formation factor should depend only on porosity. The characteristic pore body radius should be proportional to the characteristic pore throat radius. In small sets of some sandstones, these conditions are often approximated. However, in diagenetically highly altered sandstones and carbonates, these conditions are not expected to be true. And the standard NMR correlations would not work in such media.

In this work, we have improved the correlations by including surface relaxivity and formation factor in these correlations explicitly. In porous media used in this study charateristic pore throat sizes and pore body sizes are correlated. The NMR correlations

for permeability work in these media because of throat-body correlation. The effect of throat-body correlation for more complex porous media and their effect of NMR permeability correlation will be explored in our future research.

5. Plans for Next Reporting Period

- Coreflood and CT imaging of Carbonate samples (Sub-Task 3.2)
- NMR response of carbonate samples (Sub-Task 3.3)
- Microscopic imaging of carbonate samples (Sub-Task 3.1)

References

Adler, P.M., (1990), "Flow in Simulated Porous Media", *Int. J. Multiphase Flow*, v. 16, no. 4, 691.

Adler, P.M., Jacquin, C.G., and Thovert, J.F., (1992), "The Formation Factor of a Reconstructed Porous Media", *Water Resources Research*, v. 28, no. 6, 1571-1576.

Adler, P.M., and Thovert, J-F (1998), "Real Porous Media; Local Geometry and Macroscopic Properties", *Appl. Mech. Rev.*, 51, 537-585.

Bergman, D.J., Dunn, K.J., Schwartz, L.M., Mitra, P.P., (1995), "Self-diffusion in a Periodic Porous Medium", *Physical Review E*, v. 51, no. 4, 3393-3400.

Bloch, F., (1946), "Nuclear Introduction", *Physical Review*, v. 70, no. 7-8, 460-474.

Coates, G.R., Peveraro, R.C.A., Hardwick, A., and Robert, D., (1991), "The Magnetic Resonance Imaging Log Characterized by Comparison with Petrophysical Properties and Laboratory Core Data", *SPE* 22723.

Coates, G.R., Xiao, L, and Prammer, M.G., "NMR Logging Principles and Applications", Halliburtion Energy Services, Houston.

Coker, D. A. and Torquato, S., (1995), "Extraction of Morphological Quantities from a Digitized Medium", *J. Appl. Phys*, 77, 12, 6087.

Dullien, F.A.L., (1979), "Porous Media Fluid Transport and Pore Structure", Academic Press, New York.

Fordham, E.J., Sezginer, A., and Hall, L.D., (1995), "Imaging Multiexponential Relaxation in the (y,$\log_e T_1$) Plane, with Application to Clay Filtration in Rock Cores", *J. Magn.. Reson. Series A*, 113, 139-150.

Hazzlet, R. D., 1997, "Statistical Characterization and Stochastic Modeling of Pore Networks in Relation to Fluid Flow", *Mathematical Geology*, 29, 6, 801.

Huang, C.C., (1997), "Estimation of Rock Properties by NMR Relaxation Methods", Master Thesis, Rice University.

Johnson, D.L., Koplik, J., and Schwartz, L.M., (1986), "New Pore-Size Parameter Characterizing Transport in Porous Media", *Physical Review Letters*, v. 57, no. 20, 2564-2567.

Katz, A.J., and Thompson, A.H., (1986), "Quantitative Prediction of Permeability in Porous Rock", *Physical Review B*, v. 34, no. 11, 8179-8181

Kenyon, W.E., Day, P.I., Straley C., and Willemsen, J.F., (1988), "A Three-Part Study of NMR Longitudinal Relaxation Properties of Water-Saturated Sandstones", *SPE Formation Evaluation*, 3, 622-636.

Kenyon, W.E., (1997), "Petrophysical Principles of Applications of NMR Logging", *The Log Analyst*, 38, 21-43.

Kubica, P., (1995), "Statistical Test of Permeability Estimates Based on NMR Measurements", *Annual Logging Symposium Transactions: SPWLA*, 36, paper VVV.

Latorraca, G.A., Dunn, K.J., and Brown, R.J.S., (1993), "Predicting Permeability from Nuclear Magnetic Resonance and Electrical Properties Measurement", *Society of Core Analysts, SCA-9312.*

Lee, S.B., Kim, I.C., Miller, C.A., and Torquato, S., (1989), "Random Walk Simulation of Diffusion Controlled Processes among Static Traps", *Physical Review B*, 39, 11833.

Ramakrishnan, T.S., Schwartz, L.M., Fordham, E.J., Kenyon, W.E., and Wilkinson, D.J. (1998), "Forward Models for Nuclear Magnetic Resonance in Carbonate Rocks", *Transactions of the SPWLA 39th Annual Logging Symposium*, paper SS.

Roberts, A. P., 1997, "Statistical reconstruction of three-dimensional porous media from two-dimensional images", *Physical Review E*, 56, 3203.

Sahimi, M.S. and Stauffer, D., (1991), "Efficient simulation of flow and transport in porous media", *Chemical Engineering Science*, v. 46, no. 9, 2225-2233.

Seevers, D.O. (1966), "A Nuclear Magnetic Method for Determining the Permeability of Sandstones", *Annual Logging Symposium Transactions: Society of Professional Well Log Analysts*, paper L.

Siegel, R.A. and Langer, R., (1986), "A New Monte Carlo Approach to Diffusion in Constricted Porous Geometries", *J. Coll. Interf. Sci.*, v. 109, no. 2, 426-440

Singh, M., and Mohanty, K.K., (2000), "Permeability of Spatially Correlated Porous Media", *Chemical Engineering Science*, v. 55, no. 22, 5393-5403.

Straley, C., Rossini, D., Vinegar, H., Tutunjian, P., Morriss, C.E., (1995), "Core Analysis by Low-Field NMR", *Society of Core Analysts, SCA-9494.*

Timur, A., (1969), "Producible Porosity and Permeability of Sandstones Investigated Through Nuclear Magnetic Resonance Principles", *The Log Analyst*, Jan.-Feb.,3-11.

Timur, A., (1969), "Pulsed Nuclear Magnetic Resonance Studies of Porosity, Movable Fluid, Permeability of Sandstones", *Journal of Petroleum Technology*, 21, 775-786.

Torquato, S., and Kim, I.C., (1989), "Efficient Simulation Technique to Compute Effective Properties of Heterogenous Media", *Appl. Phys. Lett*, v. 55, no.18, 1847- 1849.

Yeong, C. L. Y. and Torquato, S., 1998, "Reconstructing random media", *Physical Review E*, 57, 1, 495.

Yeong, C. L. Y. and Torquato, S., 1998, "Reconstructing Random Media II. Three-Dimensional Media from Two-Dimensional Cuts", *Physical Review E*, v. 58, no. 1, 224.

Zheng, L.H., and Chiew, Y.C., (1988), "Computer Simulation of Diffusion Controlled Reactions in Dispersions of Spherical Sinks", *J. Chem. Phys*. v. 90, no. 1, 322-327.